Supplementary Information for:

Size dependent optical properties and structure of ZnS nanocrystals prepared from a library of thioureas

Ellie Bennett,[†] Matthew W. Greenberg,[†] Abraham J. Jordan,[†] Leslie Hamachi, [§,†] Soham Banerjee,[‡] Simon J. L. Billinge[‡,ǁ] and Jonathan S. Owen*[,†]

[†]Department of Chemistry, Columbia University, New York, NY 10027, USA
[§]Department of Chemistry and Biochemistry, California Polytechnic State University, San Luis Obispo, CA 93407, USA
[‡]Department of Applied Physics and Applied Mathematics, Columbia University, New York, NY 10027, USA
[ǁ]Condensed Matter Physics and Materials Science Department, Brookhaven National Laboratory, Upton, NY 11973, USA

*Email: jso2115@columbia.edu

Supplementary Information Contents:

List of SI Figures

Section I

Section II

Section III

List of SI Tables

Section I

Section III

Section I – Synthesis of ZnS

Measuring UV Absorption Spectroscopy of Aliquots:

ZnS nanocrystals synthesized using these methods absorb UV-wavelengths beginning at λ = 260 – 320 nm depending on their size. Zinc oleate, zinc tetradecanoate, hexadecane, and *alkyl*-substituted thioureas do not absorb photons in this range, therefore their reaction aliquots can be measured without purification. However, *aryl*-substituted thioureas absorb photons strongly at λ > 230 nm. Aliquots from syntheses using *aryl*-substituted thioureas must be purified prior to measuring the ZnS absorption spectrum. Additional details are provided below. Additionally, a UV-transparent solvent such as hexanes or octane should be used instead of commonly used toluene.

(A) When zinc oleate is the zinc precursor:

(i) Measuring aliquots from alkyl only thiourea reactions.
A 50 uL aliquot of the reaction mixture is added to 3 mL of hexanes (or octane). The absorbance is measured between 200 – 400 nm against a hexanes or octane blank for all samples.

(ii) Measuring aliquots from aryl containing thiourea reactions. A 200 uL aliquot added to a 10 mL centrifuge tube containing hexanes (0.5 mL) and acetone (2.0 mL). *Note: precipitation is often not immediately observed.* After centrifugation (8500 rpm, 7 minutes) the supernatant is discarded and the precipitate dispersed in hexanes (0.5 mL), the solution is then transferred to 4 mL vial and dried under vacuum to remove any remaining acetone (absorbs strongly at λ < 350 nm). Hexanes (3 mL) are added to the dried product and absorption monitored against a hexanes blank. *Note: if absorbing too strongly, all aliquots can be diluted by a factor of 2.*

(B) When zinc tetradecanoate is the zinc precursor:

ZnS nanocrystals terminated by zinc tetradecanoate have a lower solubility. To maintain a clear colloidal dispersion for optical absorption spectroscopy, aliquots are added to a stock solution of oleic acid in octane.

(i) ZnS from alkyl only containing thioureas. Aliquots (50 uL) are added to 3 mL of a stock solution of oleic acid (3 mM) in octane and held at 50 ^{o}C for 2 minutes. Upon cooling to room temperature, the absorption spectrum is measured using the oleic acid stock solution as the reference spectrum.

(ii) ZnS from aryl containing thioureas. Aliquots (100 uL) are added to 0.5 mL of a stock solution of oleic acid (36 mM) in octane and held at 50 ^{o}C for 2 minutes, before cooling and transferring to centrifuge tube. The aliquot is then purified according to *A.ii above.*

Preparing aliquots for STEM analysis

The presence of organics on a TEM grid hinders the imaging, creating a blurry and low contrast micrograph. To prepare aliquots for STEM imaging, the above purification procedure (*A.ii* or *B.ii*) is performed twice.

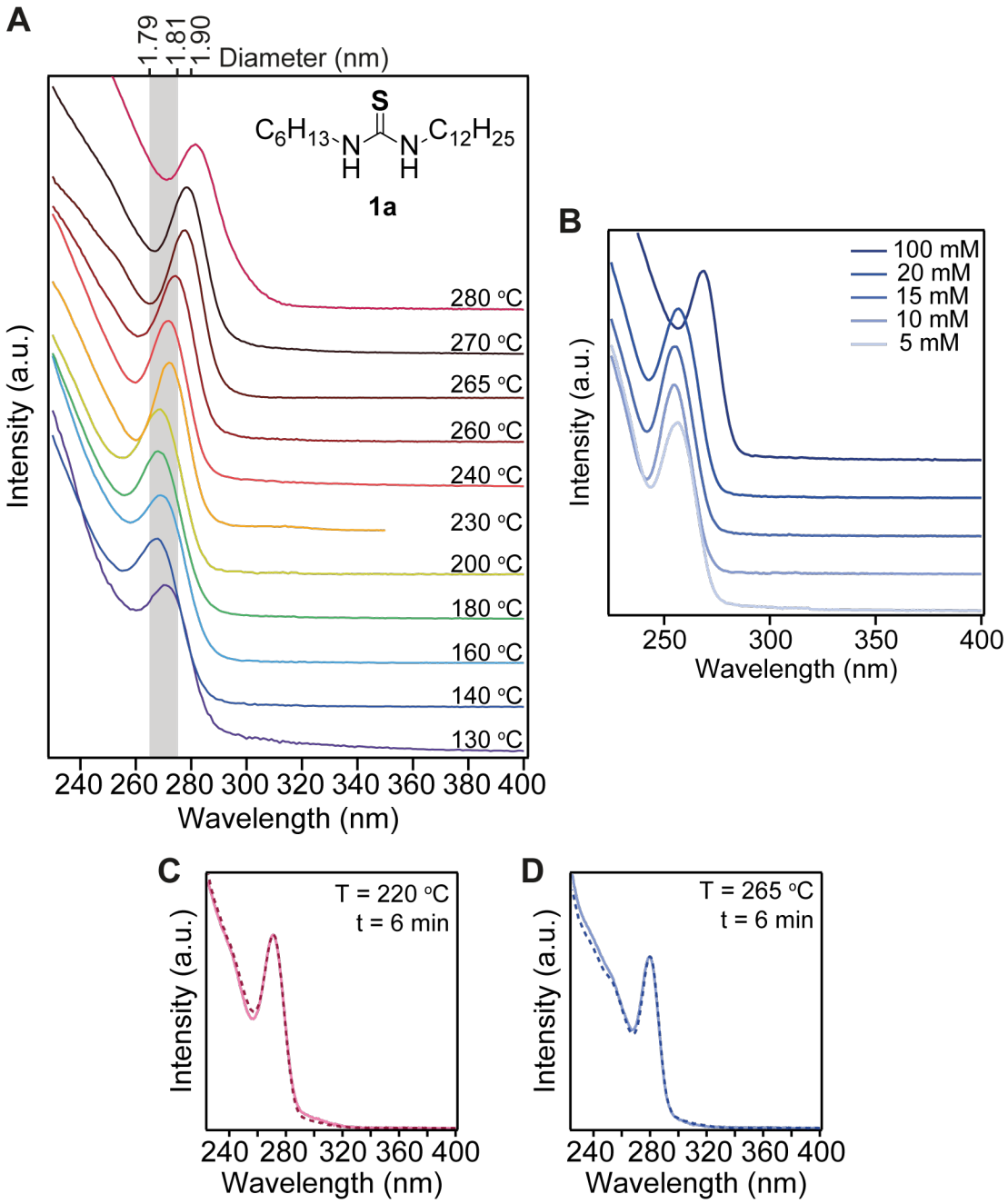

Figure S1. (A) UV absorption spectra of aliquots from ZnS reactions using zinc oleate and *N*-hexyl, *N'*-dodecyl thiourea (**1a**) across a range of temperatures (130 – 280 °C). (B) Final UV-vis trace for reaction between zinc oleate and **1a** (N-hexyl, N'-dodecyl thiourea) at 240 °C and the concentrations noted. In all cases the Zn:S precursor ratio is 1.5:1, with the concentration referring to [S]. This demonstrates the reaction can be scaled up by increasing the concentration, but this yields a larger size. (C,D) UV absorption spectra for two reactions run at T = 220 °C (C) and two run at T = 265 °C (D) (zinc oleate + **1a**). This demonstrates the reproducibility of the method described.

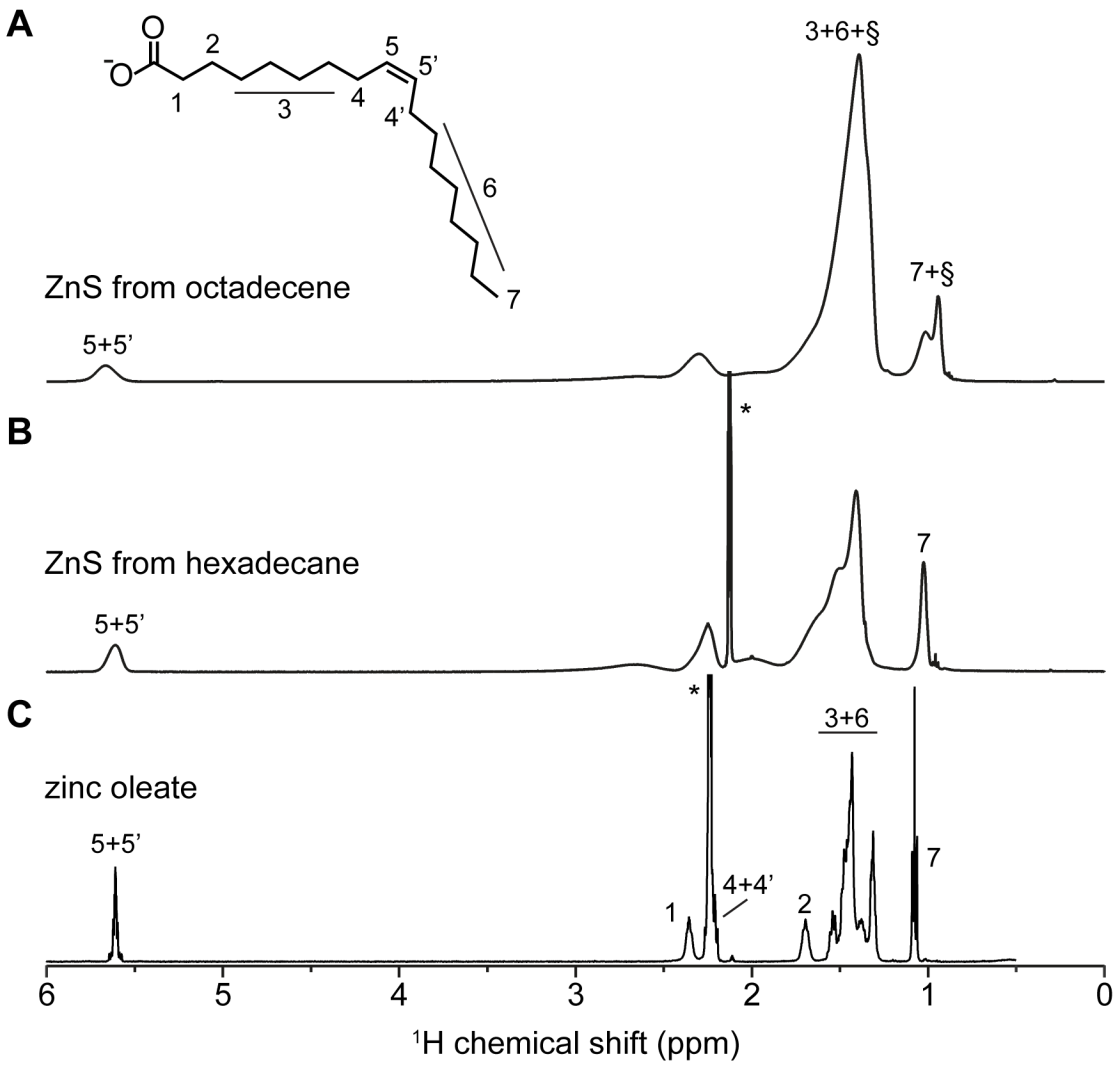

Figure S2. ^{1}H NMR was used to characterize the surface. When bound to a nanocrystal, the peaks become broadened (A-B), compared to free zinc oleate (C). When ZnS is synthesized in hexadecane, the purified nanocrystals possess the expected integration ratio (2:3) between the alkene (5+5') and methyl resonance (7) in the oleate chain (B). When synthesized in octadecene, the nanocrystal sample contains an alkane polymer impurity (§, A). This is assigned to polymerized octadecene as has been discussed previously.[1]

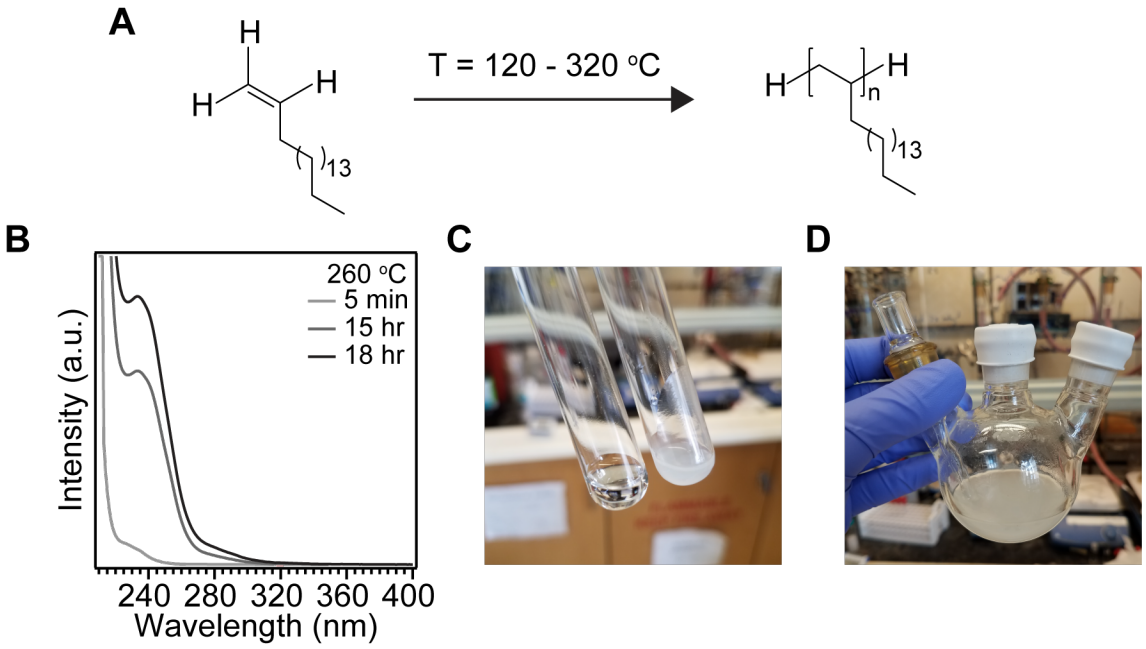

Figure S3. (A) Control reaction heating 1-octadecene under argon. (B) UV absorbance spectroscopy confirms that polymerized octadecene does not significantly impact the region where ZnS absorbs (λ = 265 – 320 nm). (C) Aliquot from octadecene reaction shows it is initially a clear, colorless liquid (left, 5 min) but turns cloudy and viscous (right, 18 hr). (D) After 18 hours, cooling to room temperature results in an opaque viscous product.

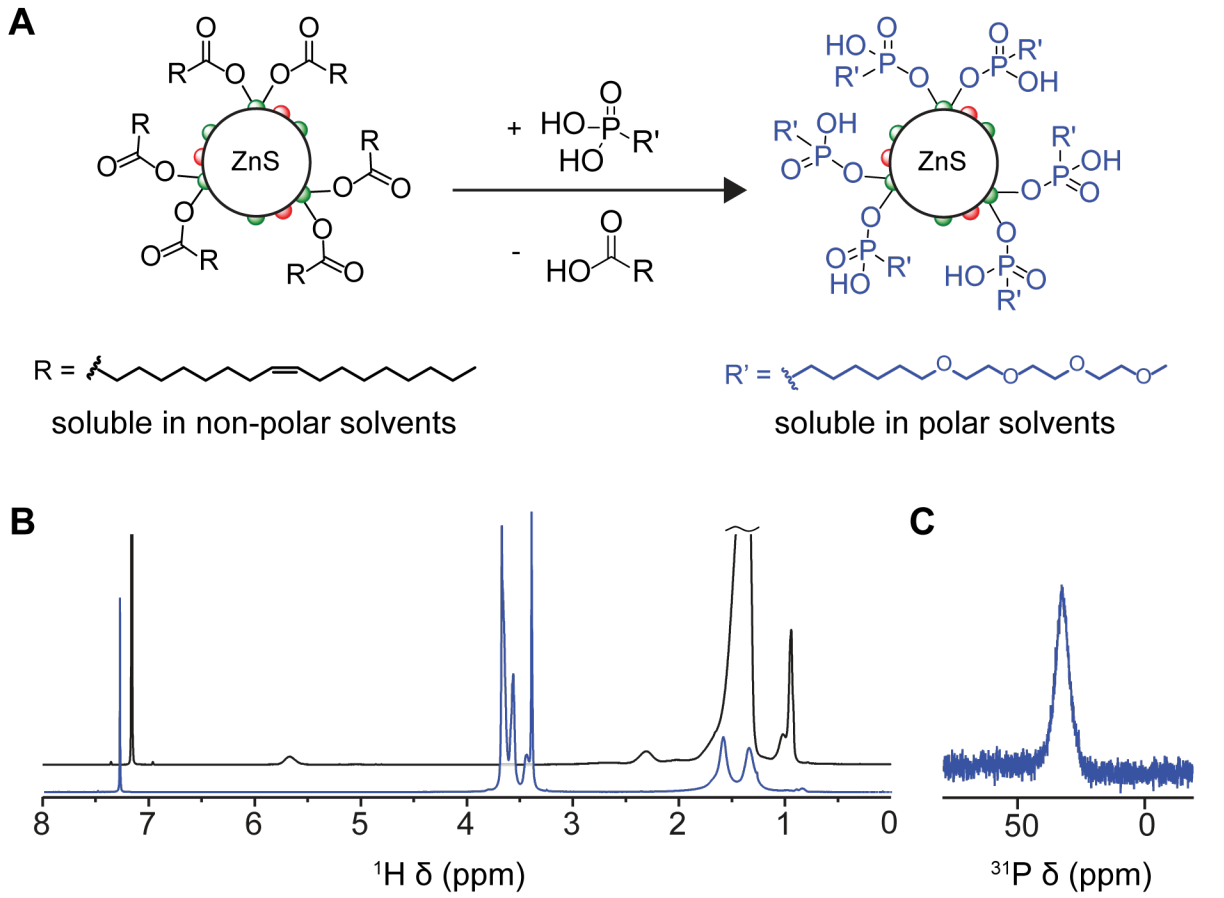

Figure S4. (A) Schematic ligand exchange from oleate to (6-[2-[2-(2-methoxyethoxy)-ethoxy]-ethoxy]hexyl) phosphonate on ZnS nanocrystals, following the procedure described by Dhaene *et al*[1]. (B) ^{1}H NMR confirms the polymer impurity initially present (black) is removed post ligand exchange and purification (blue). (C) The single broad resonance in ^{31}P spectrum confirms the binding of the phosphonate.

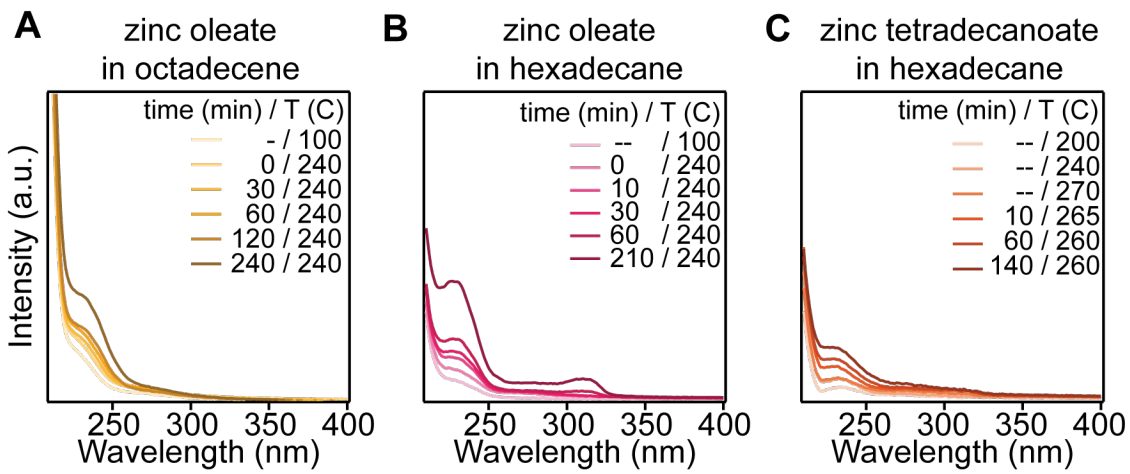

Figure S5. UV-visible absorption spectra monitoring stability of zinc carboxylates in reaction solvent. For each reaction, temperature is specified and [zinc carboxylate] = 30 mM. No significant changes in the absorption profile for zinc oleate in octadecene (A) and zinc tetradecanoate in hexadecane (C), indicating their stability. For zinc oleate in hexadecane (B), a feature between 300 – 320 nm grows in, and solution turns visibly yellow/grey. The absorbance intensity shown here is significantly less intense than from ZnS in aliquots.

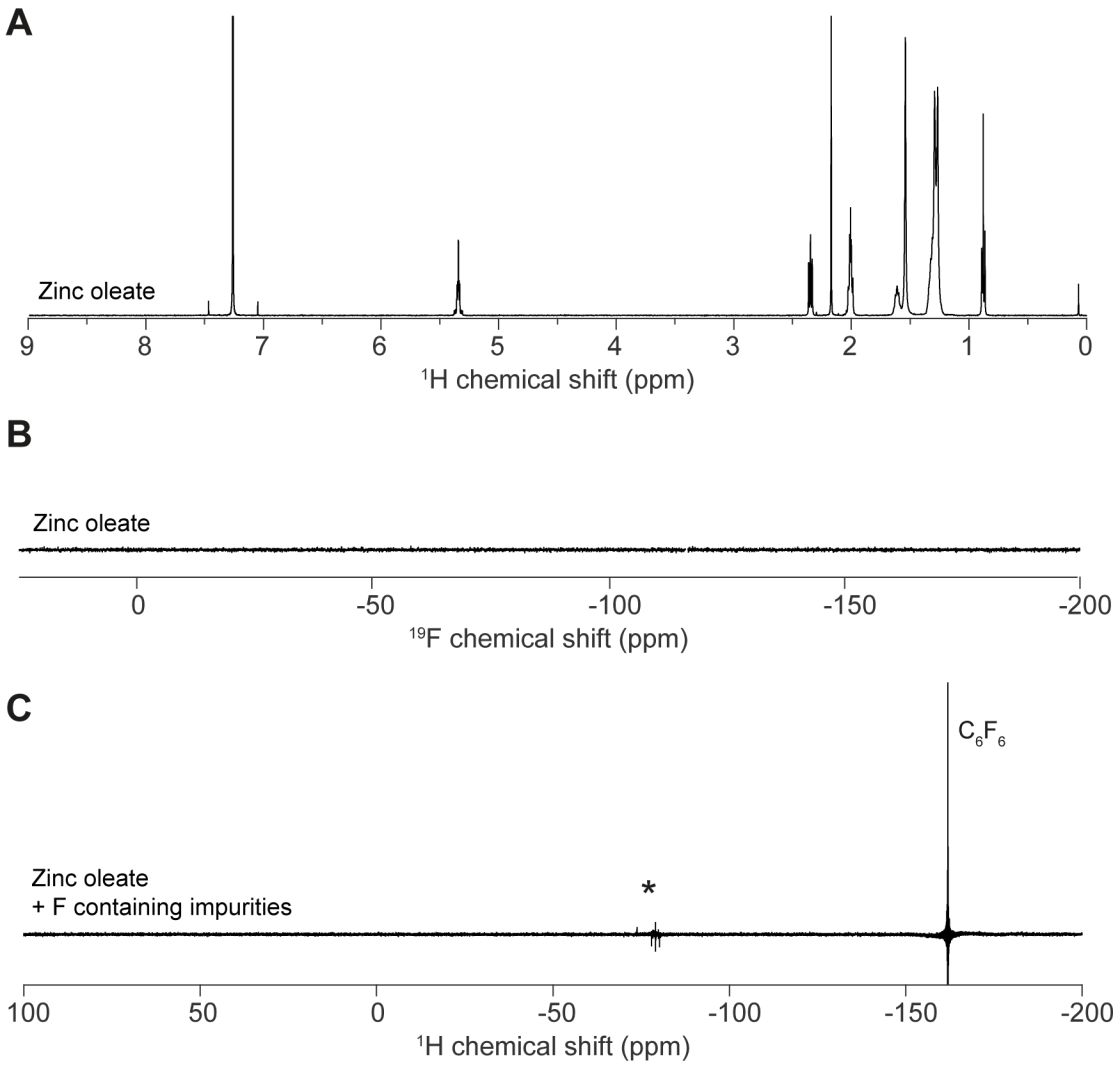

Figure S6. NMR characterization for zinc oleate. (A) ^{1}H NMR taken in $CDCl_3$ for purified zinc oleate (not recrystallized). (B) ^{19}F NMR used to confirm that no unreacted zinc trifluoroacetate or other F-containing species remain in the zinc oleate. (C) Representative ^{19}F NMR spectrum for a sample that has not been washed thoroughly and still contains byproducts (~ -75 ppm, denoted with *), the strong signal at -160 ppm is C_6F_6 used as an internal standard.

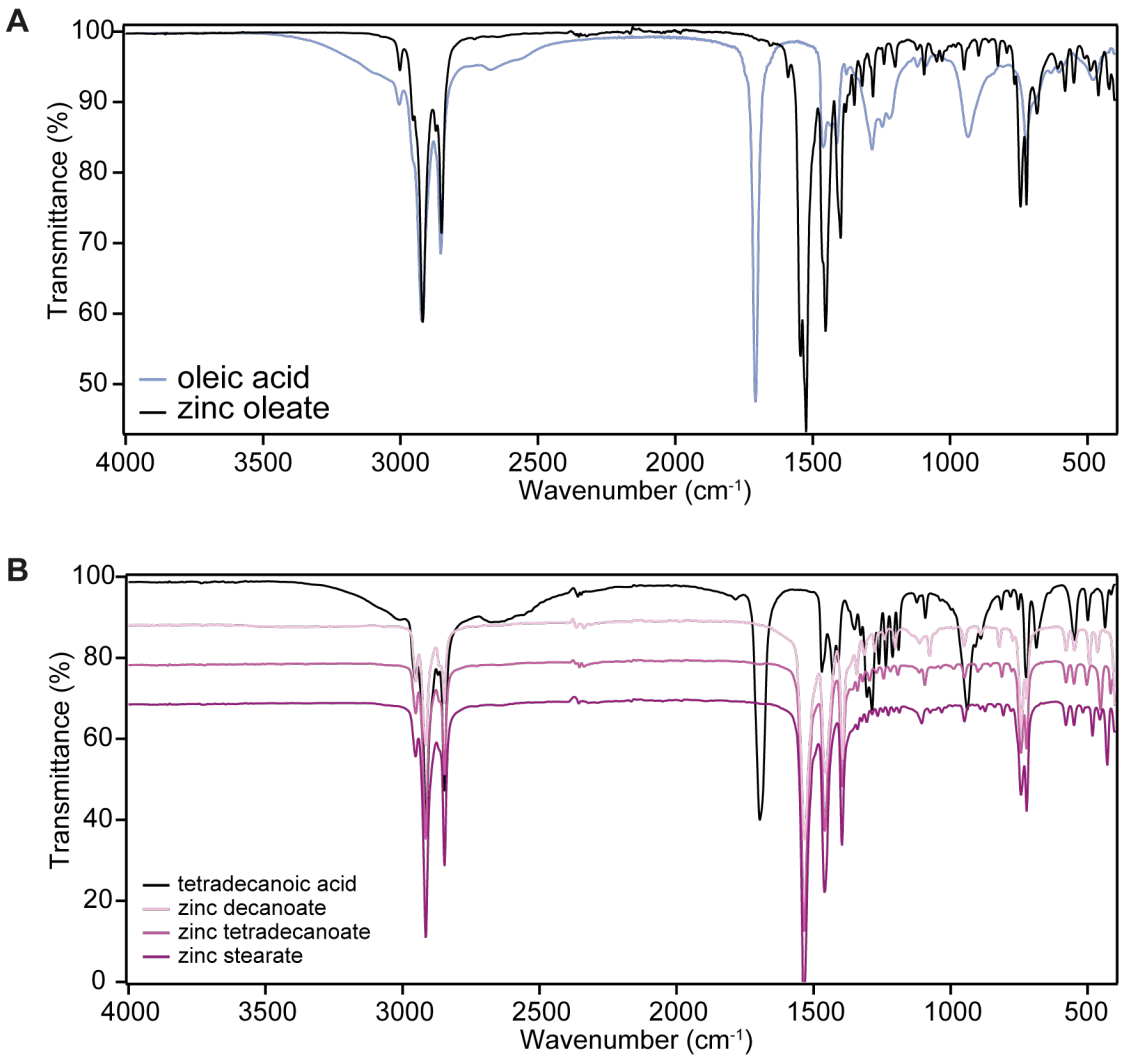

Figure S7. FT-IR characterization for the zinc carboxylates used in the study. (A) Comparison spectra for oleic acid (blue) and zinc oleate (black). The ν(O-H) region in oleic acid (2500 – 3500 cm^{-1}) is not present in the zinc oleate. Additionally, the carboxyl band ν(COOH ~1700 cm^{-1}) of oleic acid has been replaced by the symmetric (~1450 cm^{-1}) and antisymmetric (~1550 cm^{-1}) ν(COOZn) bands of zinc oleate. (B) Comparison of spectra for tetradecanoic acid (black trace) and synthesized saturated zinc carboxylates: zinc decanoate, zinc tetradecanoate and zinc stearate. As with (A), the zinc carboxylates do not contain the signature ν(O-H) or ν(COOH), but do contain the symmetric and antisymmetric ν(COOZn).

Determining the reaction endpoint:

As detailed in the main text, the progress of the reaction can be determined by monitoring the following with respect to reaction time:

1. Increase in absorbance intensity at peak and high energy wavelengths (< 240 nm)
2. Increase in average nanocrystal diameter (calculated from λ_{max})
3. Evolution of the low-energy hwhm of the absorbance feature

Analysis of ZnS reactions over a range of conditions reveals that a plateau in the growth (~ constant diameter with time) generally occurs at the same time as a plateau in the absorbance intensity at high energy wavelengths and at the excitonic feature. In addition, at this same time the *hwhm* is usually at its minimum value (Figure S8).

See Table S6 for methods to synthesize specific sizes of ZnS. Table S6 contains the synthetic parameters (precursors, solvent, reaction temperature and time) for each sizing sample included in this paper. In addition, it lists the optical properties ($E_{1s\text{-}1s}$, *hwhm*) and size (Tables S9 – S11, *d* and dispersity). The samples span the tunable range (λ = 260 – 320 nm, *d* = 1.7 – 4.5 nm and 10 nm).

In addition, we present the following synthesis guide in Tables S1 and S2. In addition, syntheses can be further tuned to increase size by increasing temperature and adding oleic acid, as discussed in the manuscript.

Table S1. Synthesis guide for *N,N'*-disubstituted precursors.

N,N'-disubstituted thiourea + unbranched zinc carboxylate				
Thiourea	T (°C)	t (min)	λ_{max} (nm)	*d* (nm)
1a-d	140	60	268 - 270	~1.79
1a-d	160	45	268 - 270	~1.79
1a-d	180	40	268 - 270	~1.79
1a-d	200	20 - 30	268 - 270	~1.79
1a-d	220	15	268 - 270	~1.79
1a-d	240	< 5	268 - 270	~1.79
1a-d*	240	10 - 30	274 - 277	1.80 - 1.85
1a-d*	260	10	~ 280	~1.9
1a-d*	280	5	~ 285	~2.1
N,N'-disubstituted thiourea + zinc 2-hexyldecanoate				
1a-d§	240	30	306 - 310	~3.8
1a-d§	265	30	312 - 316	~4.5
Precursor **1b** + unbranched zinc carboxylate (Zn:S = 3:1)				
1b	240	60 - 90	~ 295	~2.5
1b¶	240	20 - 30	~ 302	~3.0

* - Thought to follow a thermally activated ripening growth mechanism. Longer reaction times may yield larger ZnS.

§ - Aliquots monitoring these reactions showed a peak that didn't red-shift significantly throughout reaction. At these large sizes it's hard to elucidate changes in diameter from UV absorption

spectroscopy alone. Sizes represent diameters extracted from STEM analysis after running for 30 minutes.

¶ - This reaction is run with 1.5 equivalents of acid.

Table S2. Synthesis guide for *N,N',N'*- and *N,P,P*-trisubstituted precursors.

N,N',N'-alkyl trisubstituted thiourea + zinc oleate				
Thiourea	T (°C)	t (min)	λ_{max} (nm)	*d* (nm)
2a, d	180	60 - 90	~ 285	~ 2.1
2a, d	200	60 - 90	288 - 290	~ 2.2
2a, d	220	30 - 45	~ 293	~ 2.4
2a, d	240	15 - 25	298 - 300	~ 2.8
2a, d	265	~ 10	~ 305	~ 3.3
N-aryl, *N'N'*-dialkyl thiourea + zinc oleate				
2b, f-g	180	90 - 120	288 - 290	~2.2
2b, f-g	200	60 - 90	290 - 292	~2.3
2b, f-g	240	45 - 60	299 - 301	~2.9
2b, f-g	265	~30	~305	~3.3
N-aryl, *P,P*-trisubstituted + zinc oleate				
3a-b	200	90 - 120	~ 294	~ 2.5
3a-b	220	90 - 120	~ 300	~ 2.9
3a-b	240	60 - 90	~ 303	~ 3.1
N,N',N'-trisubstituted + zinc 2-hexyldecanoate				
2,3§	265	30	~315 – 317	~10

§ - Aliquots monitoring these reactions showed a peak that didn't red-shift significantly throughout reaction. At these large sizes it's hard to elucidate changes in diameter from UV absorption spectroscopy alone. Additionally, the *hwhm* analysis doesn't change. This reaction can be stopped sooner to yield *d* < 10 nm. Sizes represent diameters extracted from STEM analysis after running for 30 minutes.

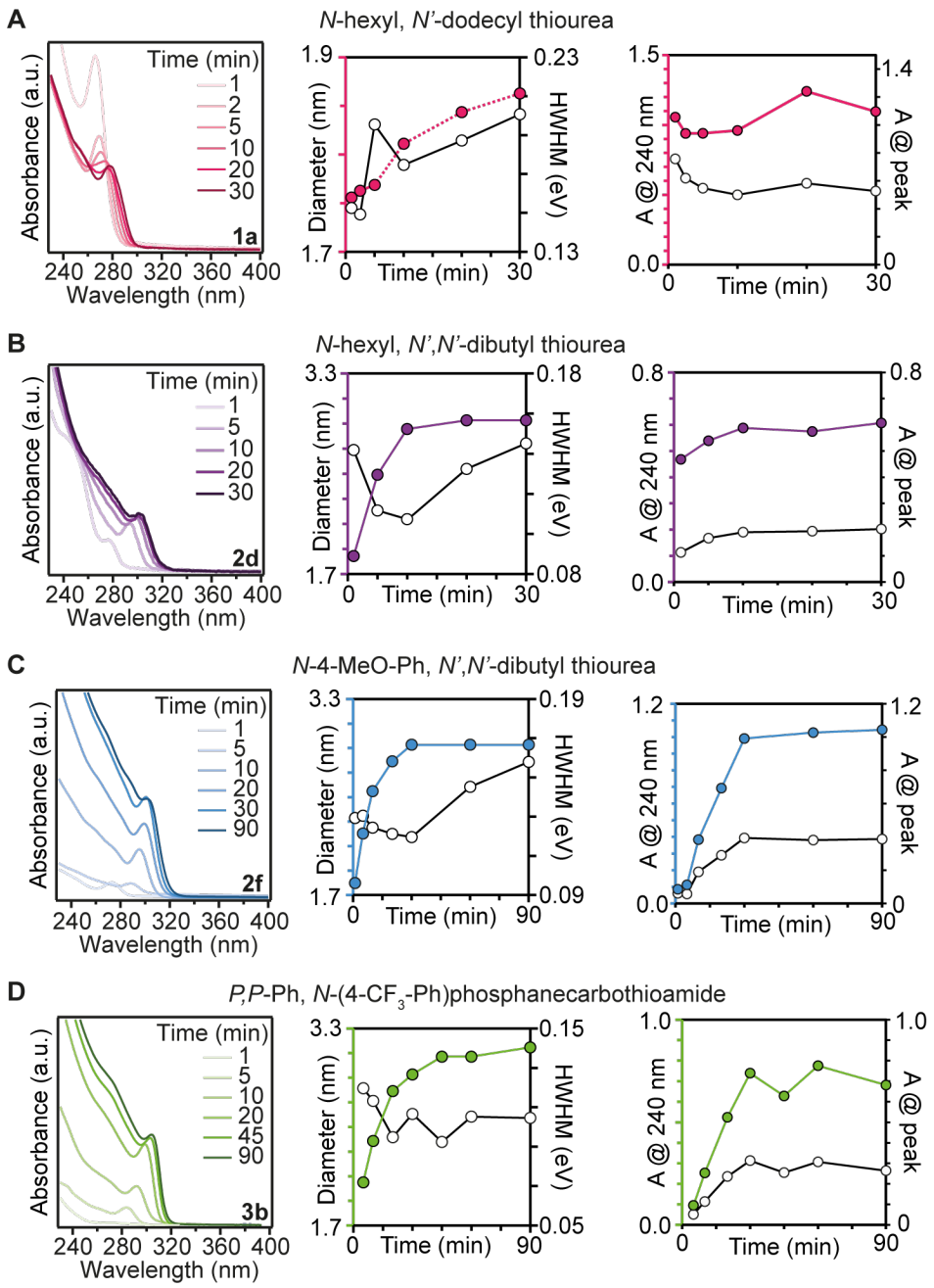

Figure S8. Monitoring ZnS reactions from *N,N'*-disubstituted (A), *N,N',N'*-trisubstituted (B,C), and *N,P,P*-trisubstituted (D) precursors. For the trisubstituted precursors, the time at which the size reaches a maximum and begins to plateau, the HWHM reaches a minimum and the absorbance intensity plateaus at both the peak, and at a higher wavelength (240 nm). This is indicative of the reaction reaching completion. For the disubstituted compounds, the conversion and precipitation reaction is immediate, although growth in the average size may continue *via* ripening when T > 240˚C.

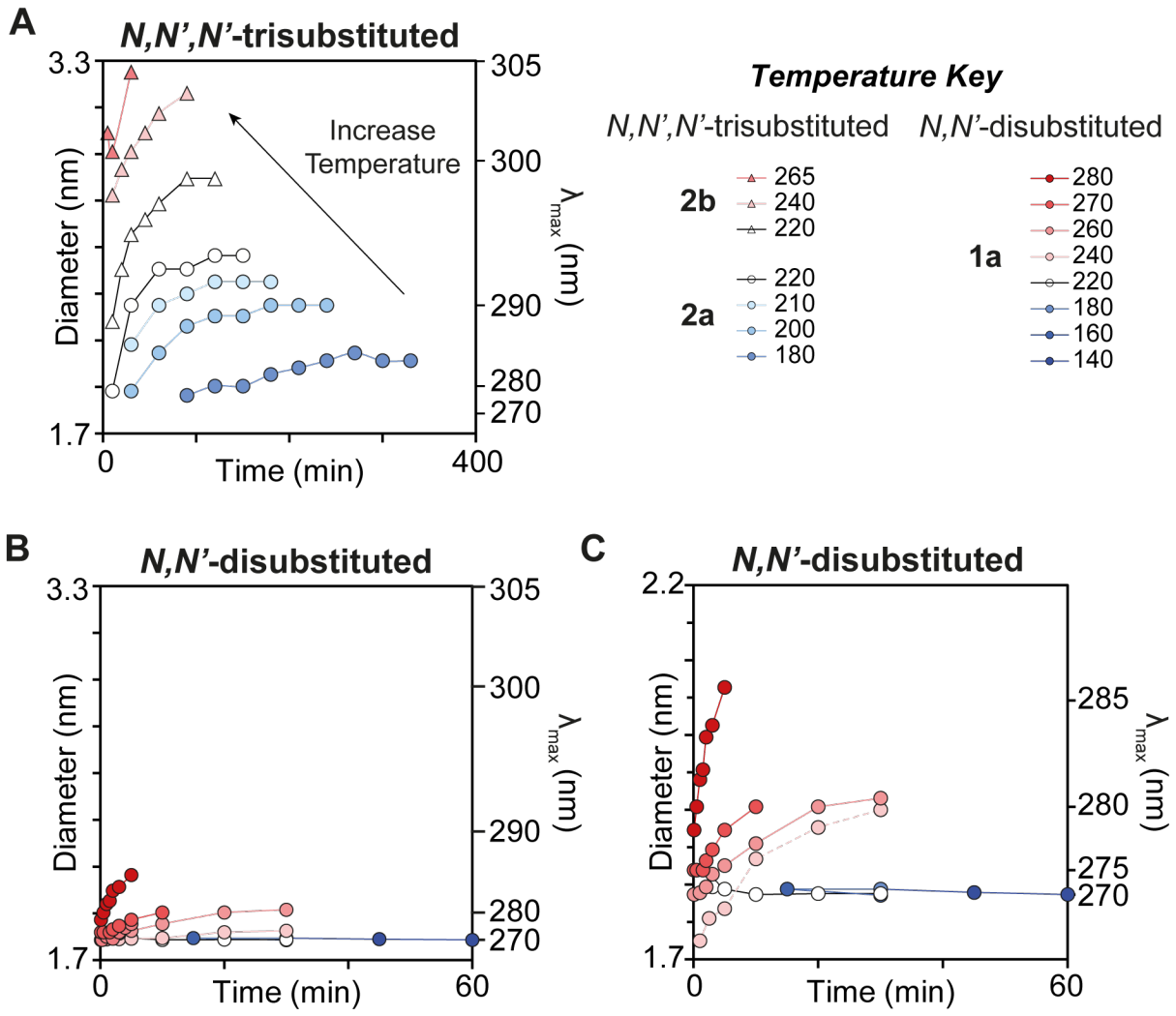

Figure S9. Evolution of ZnS diameter with reaction time as a function of reaction temperature for *N,N',N'*-trisubstituted thioureas **2a** and **2b** (A) and *N*-hexyl, *N'*-dodecyl thiourea **1a** (B, C). Increasing temperature speeds up the reaction and yields larger nanocrystals for *N,N',N'*-trisubstituted precursors (A). For *N,N'*-disubstituted compounds, a terminal size (d ~ 1.8 nm) is reached below T = 240 °C. At higher temperatures, larger sizes can be achieved likely via a ripening mechanism.

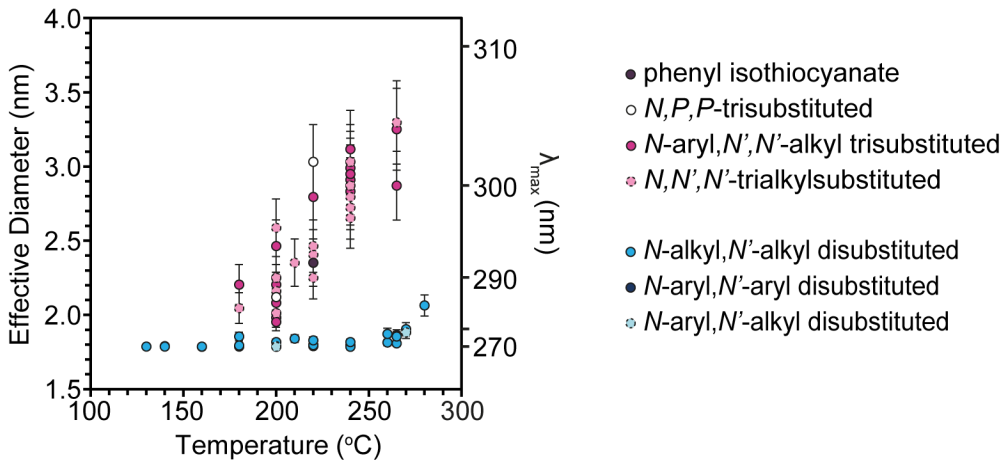

Figure S10. Figure 3 from manuscript, coded per class of precursor.

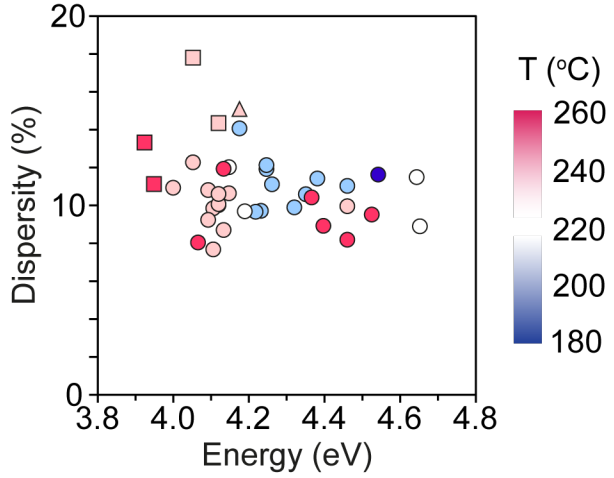

Figure S11. Size polydispersity (%) versus the band gap transition energy. The size polydispersity dispersity (σ/d) is obtained by analyzing STEM images (Appendix I). Synthesis conditions are as follows: standard conditions (circle), zinc 2-hexyldecanoate (square), and Zn/S = 3 (triangle). There is no trend between synthesis temperature and percent size polydispersity. However, the more disperse samples (> 13 %) are synthesized from zinc 2-hexyldecanoate or an initial 3:1 ratio.

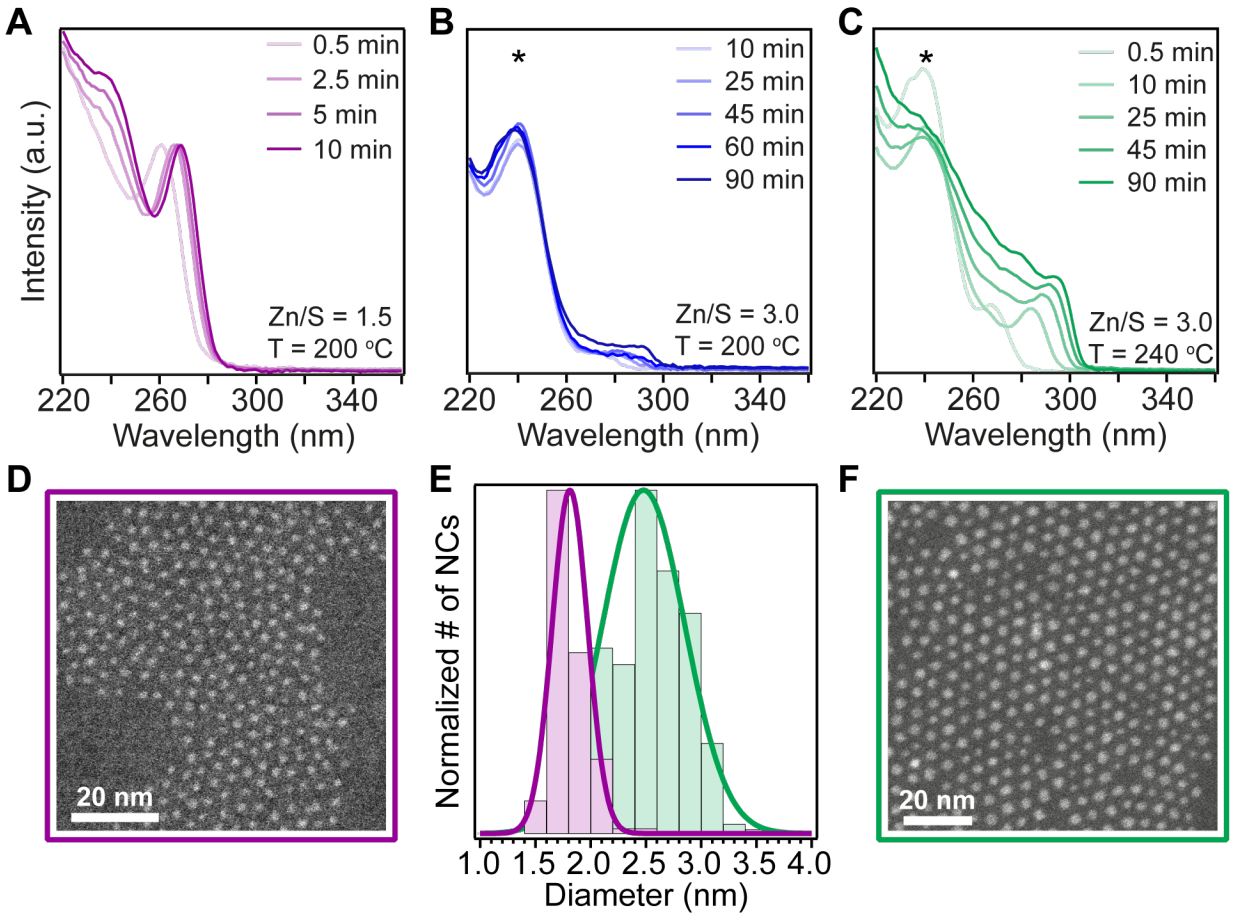

Figure S12. Comparison of initial zinc oleate:**1b** ratio 1.5 and 3, at two temperatures 200 ˚C and 240 ˚C. (A) Typical evolution of optical features with standard Zn:S ratio (1.5:1) at 200 ºC. (B) Maintaining the temperature but increasing the initial Zn:S ratio (3:1) results in the stabilization of an intermediate (*, λ ~ 240 nm), and no significant formation of ZnS. (C) The same high Zn:S ratio ran at higher temperature (240 ºC) sees the same initial spectral feature appear (*), which then converts slowly to ZnS nanocrystals. STEM images (D, F) and sizing analysis (E) confirms the differing sizes between 1.5:1 at 200 ºC (D, pink) and 3:1 at 240 ºC (F, green) (1.5:1 d = 1.78 nm, σ = 10%; 3.0:1 d = 2.5 nm, σ = 15%). Notably, the structure of **1b** appears to be promoting this reaction pathway; **1a** does not possess the λ = 240 nm absorption feature at a 3:1 ratio, or grow to the same larger sizes. In addition, higher Zn:S ratios with *N,N',N'*-trisubstituted compounds does not noticeably impact the spectral evolution.

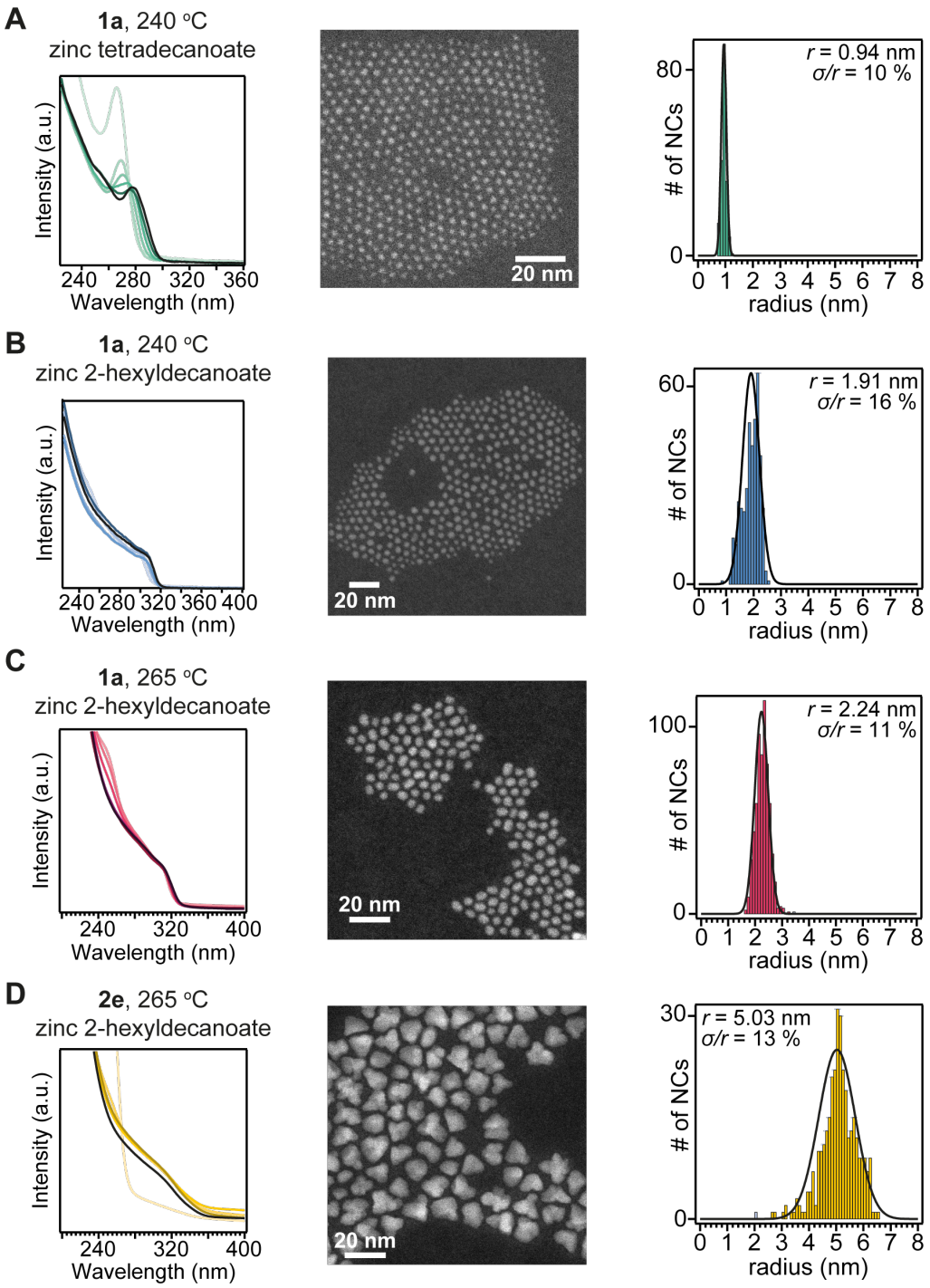

Figure S13. The impact of zinc carboxylate structure on ZnS nanocrystal size. Representative UV absorbance traces, STEM images, and sizing histograms from the following ZnS reactions: (A) **1a** + zinc oleate, 240 °C; (B) **1a** + zinc 2-hexyldecanoate, 240 °C; (C) **1a** + zinc 2-hexyldecanoate, 265 °C; (D) **2e** + zinc 2-hexyldecanoate, 265 °C. Morphology (shape) differences are discussed in Chapter 3. The radii of A–C are measured by analyzing STEM images, see Section III. For D, the total area of each nanocrystal was converted into an "effective radius" by calculating the radius of a circle required to achieve the same area.

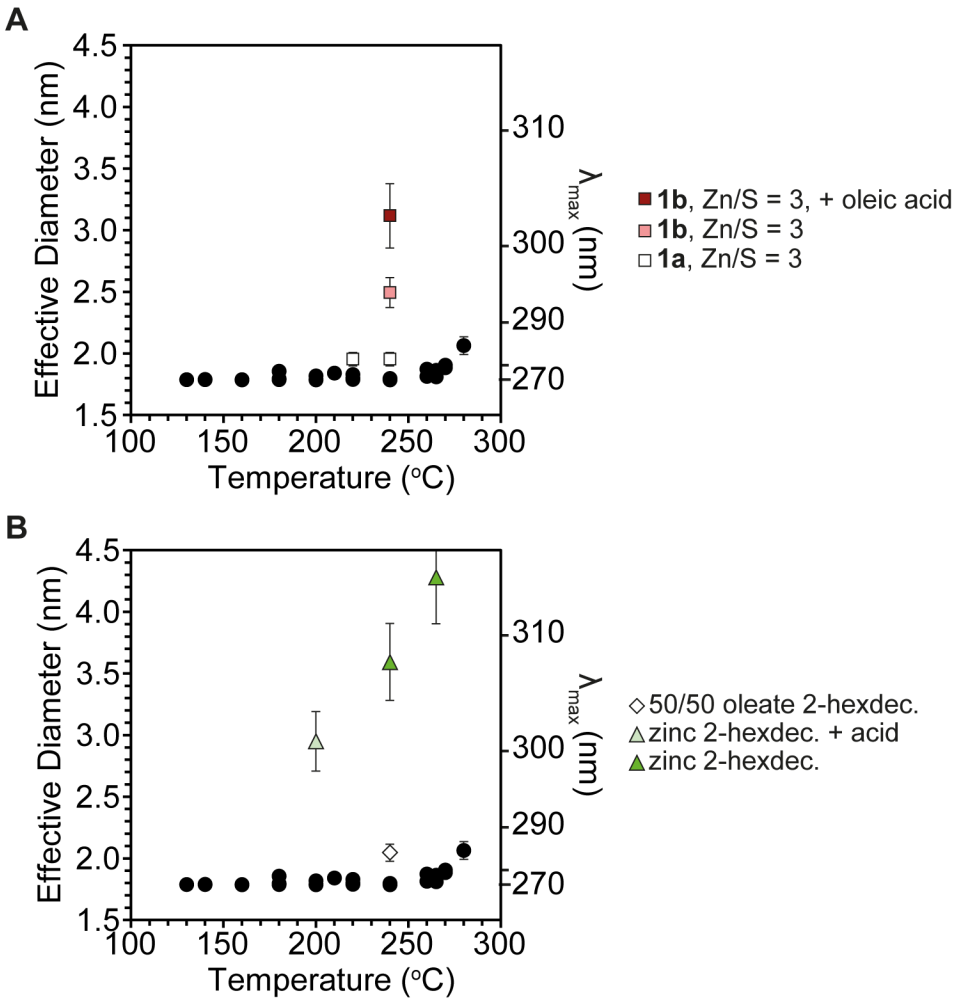

Figure S14. Impact of Zn:S ratio (A) and zinc carboxylate structure (B) on ZnS size synthesized from *N,N'*-disubstituted thioureas. Black circles represent standard conditions. Increasing the Zn/S precursor ratio to 3 (from 1.5) results in larger nanocrystals when synthesized from **1b**, and this size can further be increased with the addition of oleic acid (A). Under the same conditions, switching from an unbranched (black circles) to branched (triangles) zinc carboxylate, larger ZnS can be synthesized using **1a** (B).

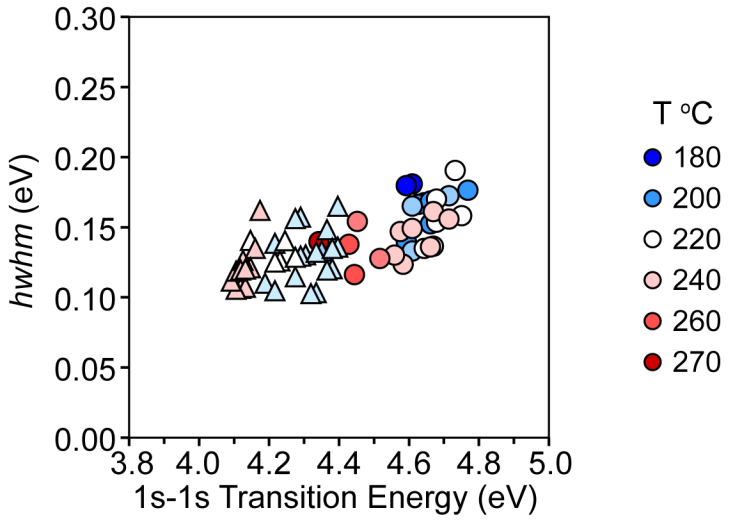

Figure S15. Half-width half maximum as a function of transition energy for isolated ZnS nanocrystals. All reactions are unbranched zinc carboxylates with *N,N'*-disubstituted thioureas (circles) or *N,N',N'* and *P,P,N*-trisubstituted precursors (triangles). Points are color-coded for temperature.

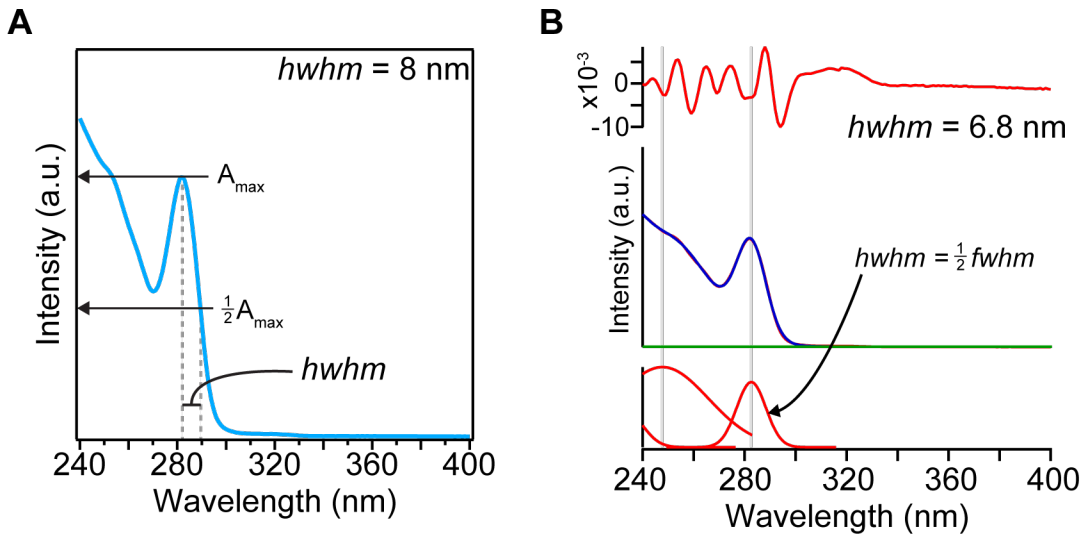

Figure S16. Calculating *hwhm*. The *hwhm* values reported are using method (A). Here, the *hwhm* of the red-tail of the excitonic feature is estimated by subtracting the $\lambda_{A,max}$ from $\lambda_{A,halfmax}$, here giving *hwhm* = 8 nm. This method is used as it is fast. The *hwhm* can be more carefully extracted by fitting the absorbance feature to a gaussian curve (B). Here, the *hwhm* is 6.8 nm. The gaussian fitting method is especially challenging for the weakly quantum confined ZnS (d > 3 nm). Hence method (A) is used, even though it systematically overestimates the width of the peaks. However, so long as the same method is used for all samples, comparisons can be drawn.

Section I - References

1. Dhaene, E.; Billet, J.; Bennett, E.; Van Driessche, I.; De Roo, J., The Trouble with ODE: Polymerization during Nanocrystal Synthesis. *Nano Letters* **2019,** *19*, 7411-7417.

Section II - Morphology Discussion

The shape dispersity in ZnS nanocrystals was analyzed using UV absorption spectroscopy and HAADF-STEM (referred to throughout this section as "STEM"). Purified zinc oleate, specific thiourea precursors, and using zinc oleate instead of zinc myristate, yields spherical nanocrystals with the narrowest shape dispersity. Here, we further detail the factors impacting shape dispersity.

General considerations

UV-vis absorbance and shape dispersity. Inspection of STEM images of the ZnS reveals most samples are spherical or quasi-spherical, but some samples possess more anisotropic shapes (Figure S17). Additionally, there is a link between the isotropy of the ZnS and the optical features, with quasi-spherical nanocrystals possessing a more well-defined absorption feature (Figures S17-S19). The broadening of the feature is not always captured by the *hwhm* analysis, as this analyzes on the red-tail of the absorption and relies heavily on the accurate determination of the peak position – something that is harder to do with broader peaks. Thus, the broadening of the optical spectra after growth can be attributed in part to an increasing shape dispersity.

TEM versus STEM. The shape dispersity is easier to assess using STEM compared to TEM. By TEM, the nanocrystal-background contrast is low and so the edges of the nanocrystals are not easily defined, and as such, all samples appeared roughly spherical. By instead using STEM, the contrast is increased, and the size and shape of the ZnS are more accurately assessed. Providing a sample is sufficiently stable under the electron beam, we suggest that STEM be used for all nanocrystal characterization, as TEM can often simplify the structure to a smooth sphere.

Effect of carboxylate structure and impurities on shape anisotropy:

1. *Addition of zinc acetate.* We added zinc acetate to a synthesis to study its effect on the evolving nanocrystal shape (Figure S19). Increasing from 0% zinc acetate, to 10, 25 and 50% saw the spectral feature broaden out, and the corresponding STEMs confirm anisotropic, tetrapod-like morphologies for the ZnS synthesized in the presence of zinc acetate. In addition, the anisotropic nanocrystals are more aggregated, consistent with a metal acetate coordinating to the surface and reducing the colloidal stability.
2. *Zinc carboxylate purity.* We examined the morphology of ZnS from zinc carboxylates synthesized from zinc trifluoroacetate and zinc nitrate (Figure S18). An advantage of the method utilizing zinc trifluoroacetate is that impurities can easily be detected by ^{19}F NMR. Comparing different syntheses of zinc tetradecanoate (which produces more anisotropic nanocrystals than zinc oleate) we found that pure zinc tetradecanoate made from zinc trifluoroacetate produced the least anisotropic ZnS. Zinc carboxylates made using the same route, but not washed thoroughly and still containing impurities detectable by ^{19}F NMR (likely zinc trifluoroacetate), produced highly anisotropic nanocrystals. Similarly anisotropic nanocrystals were produced from the zinc carboxylate synthesized from zinc nitrate, which we attribute to undetected nitrate impurities. Like for the case of the acetate, we suspect that the coordination of these small anions (e.g. nitrate, trifluoroacetate) to the surface of the growing ZnS can drive anisotropic growth. To achieve the most isotropic, spherical ZnS, care must be taken to ensure that the zinc carboxylate is pure. A second effect may be related to the presence of zinc hydroxide formed under the basic methanolic conditions used to make zinc tetradecanoate and zinc nitrate. This impurity is avoided in the trifluoroacetate route by using excess of trifluoroacetic acid. Additionally, the zinc oleate is washed multiple times, dried thoroughly *in vacuo*, and its purity checked by ^{1}H and ^{19}F NMR before use (Figure S6).
3. *Zinc oleate vs zinc tetradecanoate.* More isotropic ZnS is produced from zinc oleate compared to zinc tetradecanoate (Figures S26, S27). Similarly, increasing the zinc oleate

to thiourea ratio to 3:1 produces significantly less isotropic particles for precursors **2-3** (Figure S20). These effects may be explained by the influence of the chain structure on the surface ligand packing or differences the stability of the metal carboxylate complex toward decomposition.

Impact of zinc carboxylate structure on ZnS shell deposition:
Unbranched vs branched zinc carboxylates. Islands often form when depositing a ZnS shell onto a core nanocrystal. The island growth is commonly attributed to interfacial strain caused by the lattice mismatch. However, we find that isotropic shells can be grown on $Zn_xCd_{1-x}S_ySe_{1-y}$ nanocrystal cores from zinc 2-hexyldecanoate (Figure S21). If instead zinc oleate is used, highly anisotropic shells are grown. Interestingly, adding 2-hexyldecanoic acid to the zinc oleate shelling mixture resulted in slightly more isotropic shells being deposited. Further improvements to the homogeneity could be made by increasing the temperature. These results may be explained by a lower coverage of the bulkier ligands on the growing surface supporting more isotropic growth. In addition, use of zinc 2-hexyldecanoate results in faster deposition of ZnS (both when shelling and synthesizing nanocrystals), and this fast deposition could also favor unselective, isotropic growth.

Influence of thiourea precursor:
1. *Precursor substituents.* ZnS synthesized from *N,N'*-disubstituted thioureas are spherical, whereas *N,N',N'*-trisubstituted precursors yield a more irregular morphology. In particular, *N*-R, *N'*-pyrrolidine trisubstituted thioureas give more anisotropic ZnS than other *N,N',N'*-trisubstituted precursors examined in this study (Figure S24). This is in contrast to, for example, *N*-4-X-phenyl, *N',N'*-dibutyl thioureas (X = H, OMe, CF_3) which remain reasonably spherical throughout (Figure S22).
2. *Conversion by-products.* Given the sensitivity of anisotropicity to the thiourea, we explored the possibility that the conversion by products (oleic acid and oleic anhydride) influenced the polydispersity (Figure S29). As has been described previously, added oleic acid yields larger nanocrystals, with increased polydispersity, but no notable changes to the morphology. Stearic anhydride (to mimic the formation of oleic anhydride) also yielded no noticeable change in ZnS synthesized from **1a**.
3. *Impact of ZnS diameter.* Under the same synthetic conditions *N,N'*-disubstituted thioureas yield smaller ZnS nanocrystals than *N,N',N'*-trisubstituted precursors. To probe whether the observed morphology difference was purely a function of size, large ZnS (d ~ 4.5 nm) was synthesized from *N*-hexyl, *N'*-dodecyl thiourea (**1a**) and zinc 2-hexyldecanoate (T = 265 °C). STEM shows it still resulted in quasi-spherical nanocrystals (Figure S13 compared to S17).

Influence of solute supply kinetics and total reaction time:
Given the difference in reaction times and precursor conversion rate between the *N,N'*- and *N,N',N'*-substituted thioureas, we hypothesized that longer reaction times or slower solute supply kinetics could cause shape polydispersity.
1. We aimed to synthesized similar size ZnS from **1a** (λ_{max} = 282 nm, d ~ 2.0 nm from sizing curve) and **2b** (λ_{max} = 289 nm, d ~ 2.2 nm from sizing curve) by adjusting the temperature and reaction time and compare the resulting morphology (Figure S28). Again, the ZnS synthesized from **1a** results in the most isotropic shaped nanocrystals.
2. We manually slowed the solute supply by doing a slow continuous syringe-pump addition of *N*-hexyl, *N'*-dodecyl thiourea (**1a**) (Figure S30). As expected, large anisotropic ZnS is formed. This is the only case where a *N,N'*-disubstituted precursor yields anisotropic ZnS.

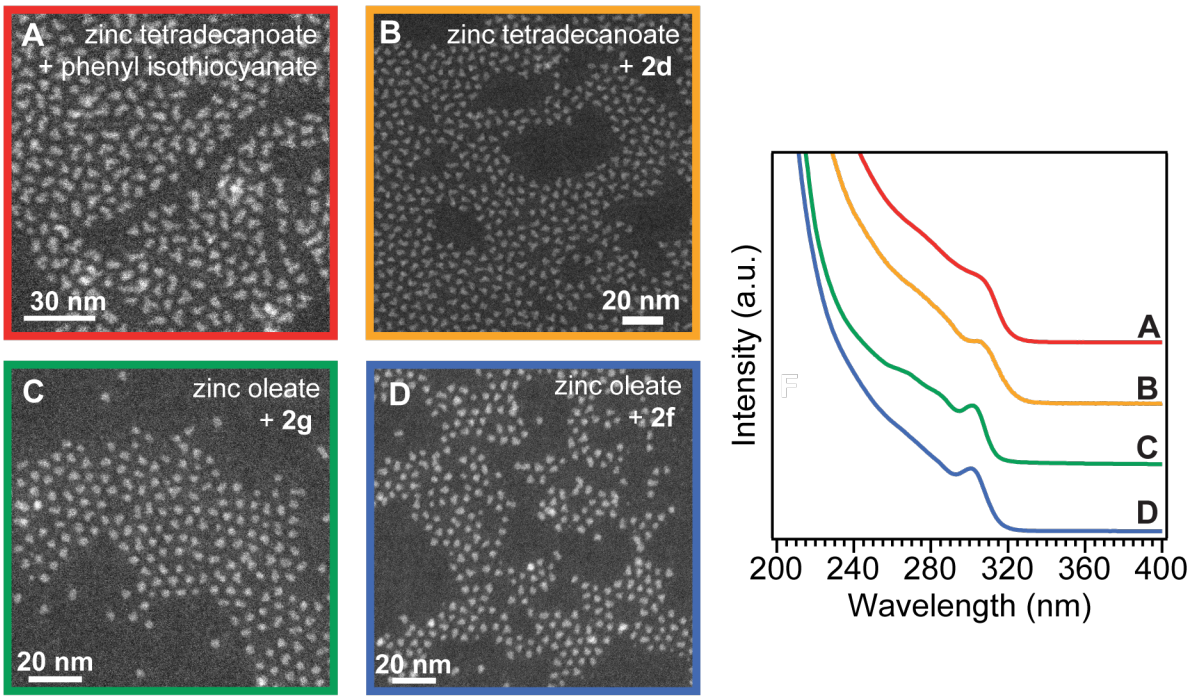

Figure S17. Link between ZnS isotropy and optical absorbance feature. The more spherical ZnS nanocrystals (C, D) result in more well-defined UV absorbance spectra. As the nanocrystals become increasingly anisotropic (A, B) the excitonic feature broadens and the peak is ill-defined.

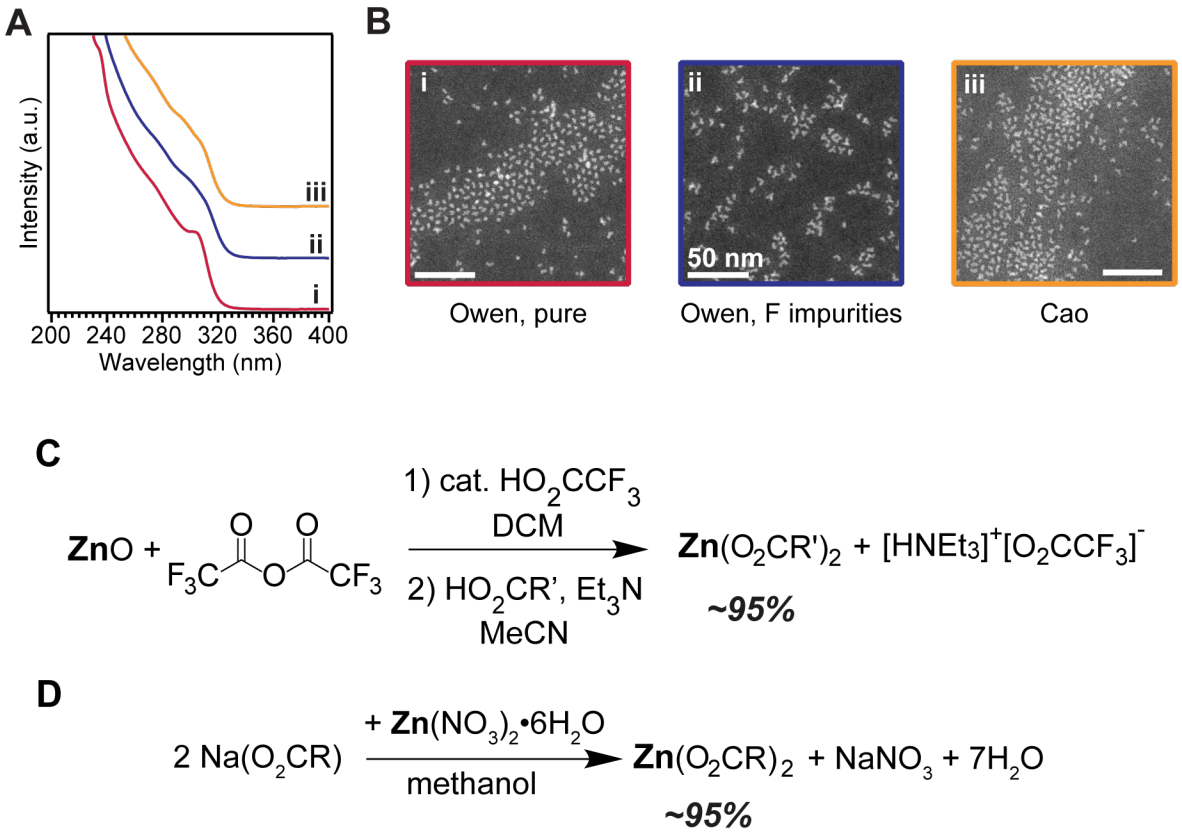

Figure S18. UV absorbance spectra for ZnS synthesized from zinc tetradecanoate. Pure zinc tetradecanoate yields irregular ZnS (B). However, known inclusion of trifluoroacetate impurities, or suspected inclusion of nitrate impurities drives anisotropic, tetrapod-like growth. Eliminating small anionic ligands is necessary to achieve isotropic growth. Zinc tetradecanoate was synthesized from zinc oxide (Owen[1], C) and zinc nitrate (Cao[2], D).

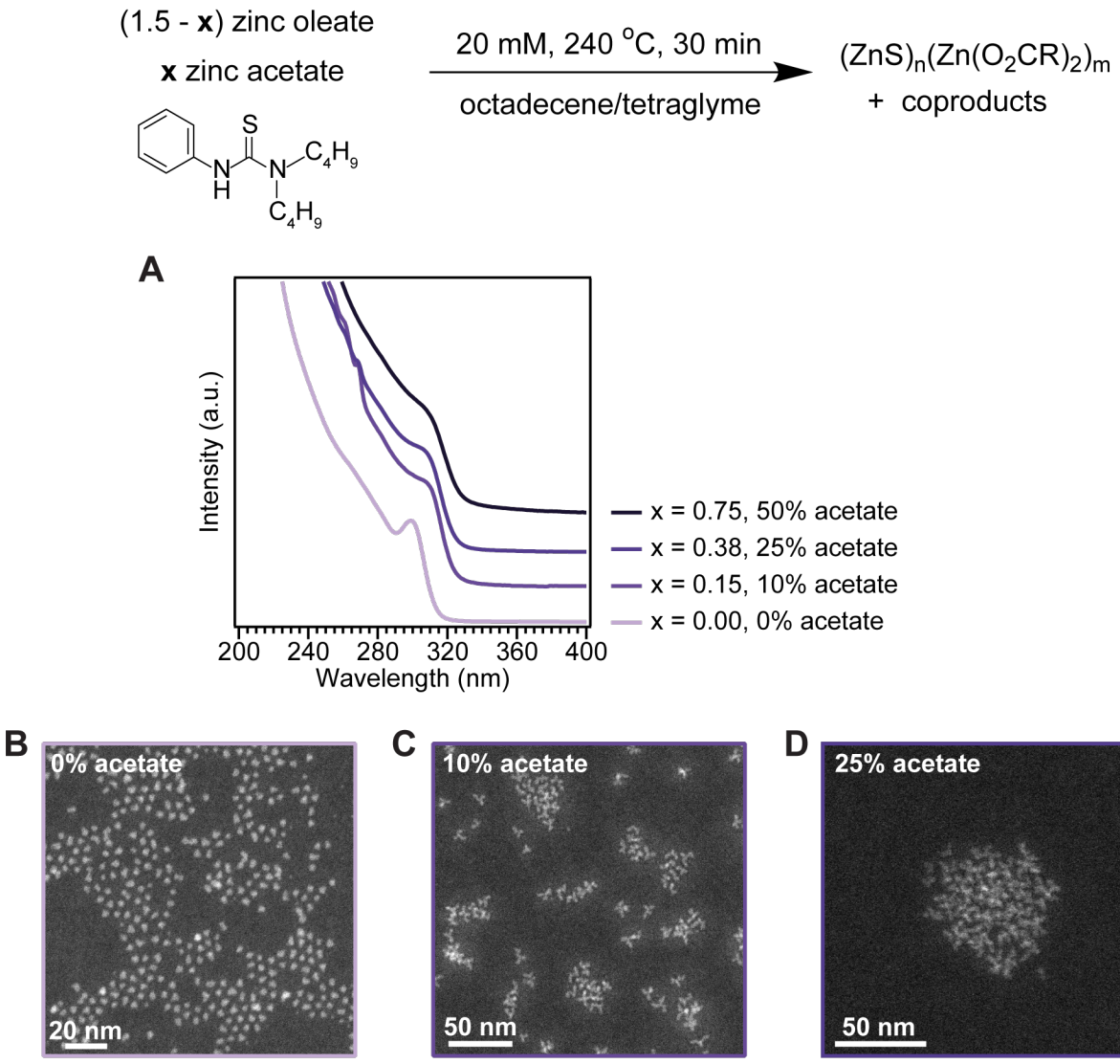

Figure S19. Introduction of acetate into a ZnS synthesis drive anisotropic growth. The UV absorbance spectra show a broadened feature when synthesized in the presence of acetate (10, 25, and 50 mol.%) compared to only zinc oleate (A). STEM confirms the formation of highly anisotropic ZnS with 10 and 25 mol.% acetate (C, D), compared to the quasi-spherical nanocrystals formed from zinc oleate (B). The 50 mol.% sample precipitated during washing, indicative of the lower colloidal stability afforded by zinc acetate.

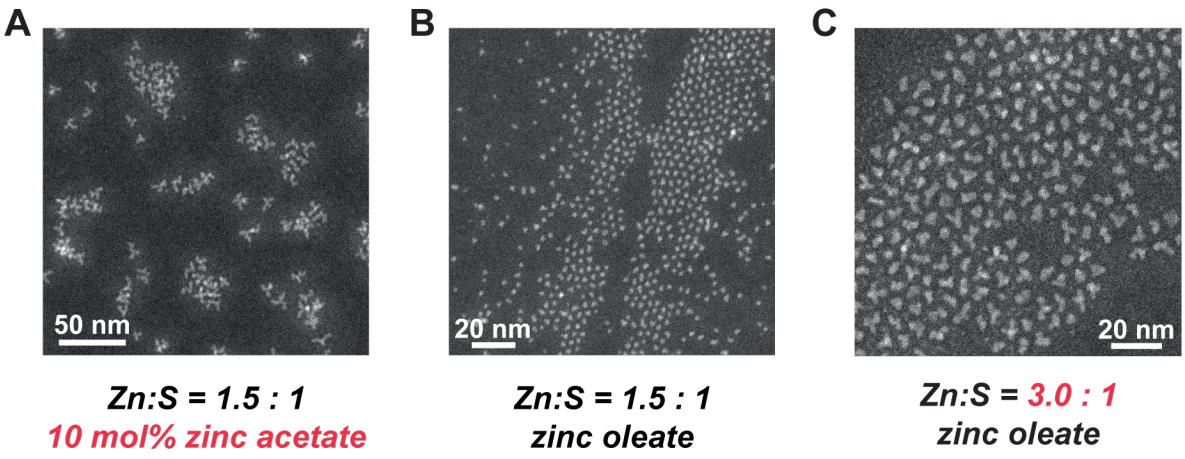

Figure S20. Reactions run in the presence of zinc acetate (A), or with higher zinc oleate ratios (Zn:S = 3:1) (C) yield anisotropic structures. Conversely, eliminating the presence of small anions and running with a lower zinc oleate excess (Zn:S = 1.5:1) yields quasi spherical nanocrystals.

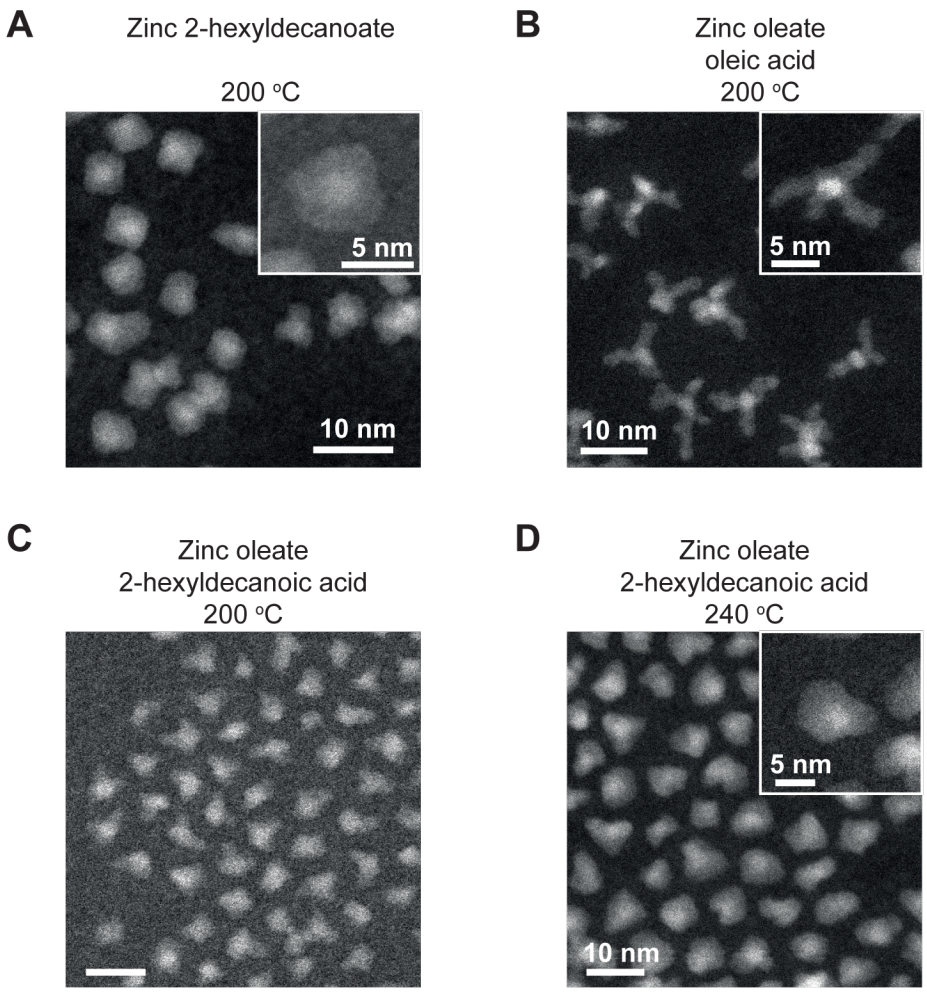

Figure S21. At 200 °C, the use zinc 2-hexyldecanoate results in isotropic shell growth (A), whereas zinc oleate grows anisotropic "arms" (B). The faster ZnS deposition and lower surface coordination afforded by zinc 2-hexyldecanoate causes these morphology differences. When using zinc oleate, the homogeneity of deposition can be increased by adding 2-hexyldecanoic acid (C) and growing at a higher temperature (D). The core nanocrystals are $Zn_xCd_{1-x}S_ySe_{1-y}$ and their synthesis will be reported in an upcoming publication.

Deposition of ZnS shell onto nanocrystal cores. The manuscript describing the preparation of the $Zn_xCd_{1-x}S_ySe_{1-y}$ core nanocrystals is under preparation. The shelling method will be described here. For example, the shelling corresponding to Figure S21B. In air zinc oleate (0.653 g, 1.04 mmol, 1.04 equiv.), oleic acid (0.294 g, 1.04 mmol, 1.04 equiv.) and 1-octadecene (9 mL) are loaded into a 25 mL Schlenk flask. This is attached to the vacuum line and sealed with a septum. The Schlenk is heated to 100 °C and degassed for 2 hours. Under inert atmosphere *N*-butyl, *N',N'*-dibutyl thiourea (2a) (0.272 g, 1 mmol, 1 equiv.) and 1-octadecene (1 mL) are loaded into a 4 mL vial which is sealed with a septum. The 4 mL vial is attached to argon supply. After degassing the zinc oleate solution, the flask is filled with argon and left stirring at 60 °C. The core nanocrystals in octadecene are heated to the shelling temperature. When shelling is ready to commence, the solution of 2a in octadecene is injected into the zinc oleate Schlenk, forming the shelling solution. The shelling solution is taken up in a syringe and injected slowly *via* syringe pump over the course of an hour (~ 1 mmol S/hr). After the injection has completed the reaction is left to stir at the synthesis temperature for a further 15 minutes, before removing from the heat and allowing to cool to room temperature. The product is isolated following the procedure outlined for pure ZnS nanocrystals.

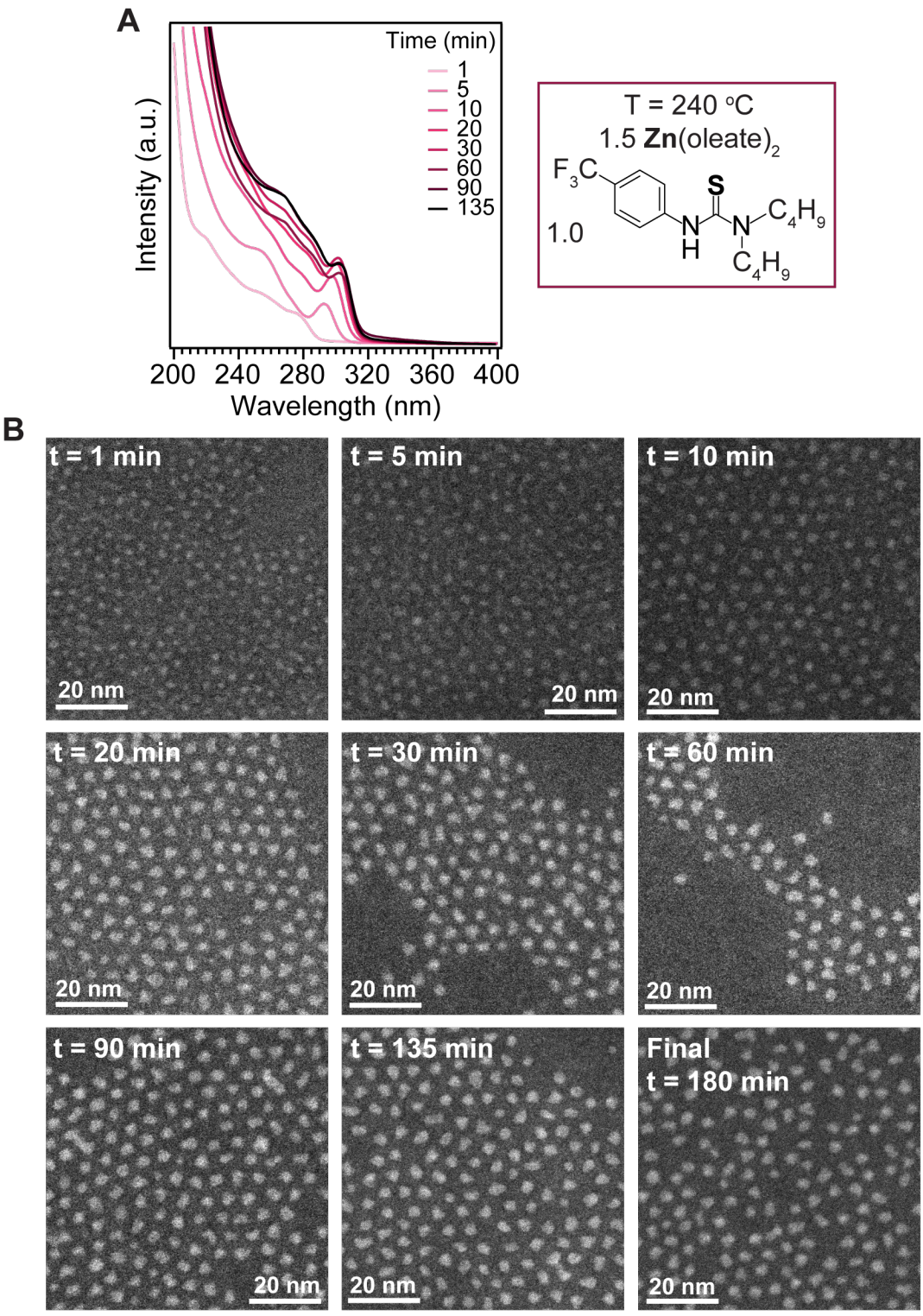

Figure S22. UV absorption spectra and STEM images of aliquots from the reaction between zinc oleate and **2g**. Reaction is completed after approximately 45 minutes. Size dispersities for these samples are shown in Figure S23.

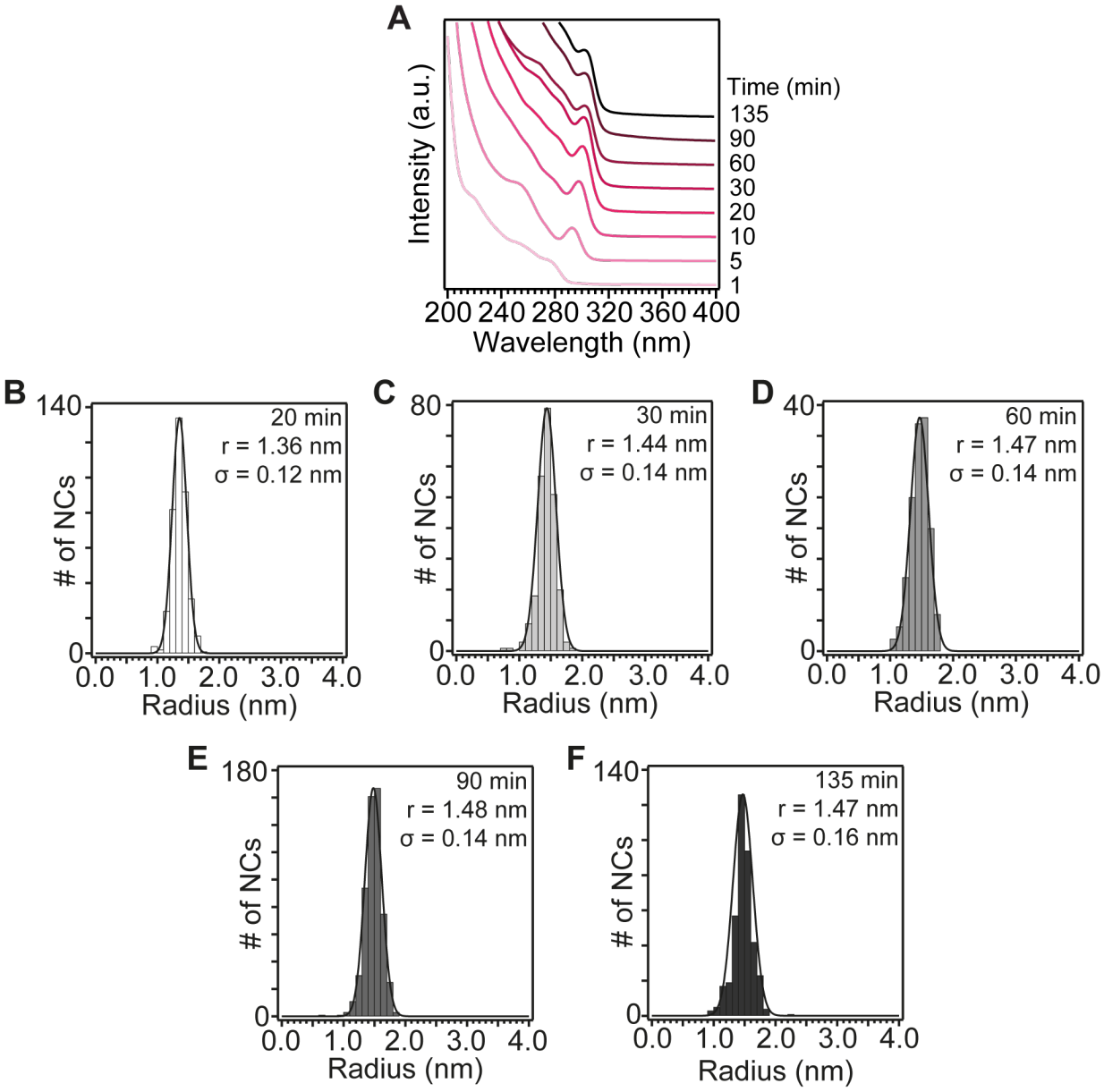

Figure S23. (A) UV absorbance spectra from a ZnS reaction and (B-F) size histograms from STEM analysis for the corresponding time points (STEM micrographs are shown in Figure S22). After 30 minutes, there is no red-shift in the UV absorbance, and STEM confirms a steady average diameter of ~ 1.47 nm. There is only a slight increase in radius standard deviation in this time ($\Delta\sigma$ = + 0.02 nm). A more detailed description of the sizing method is included in Section III.

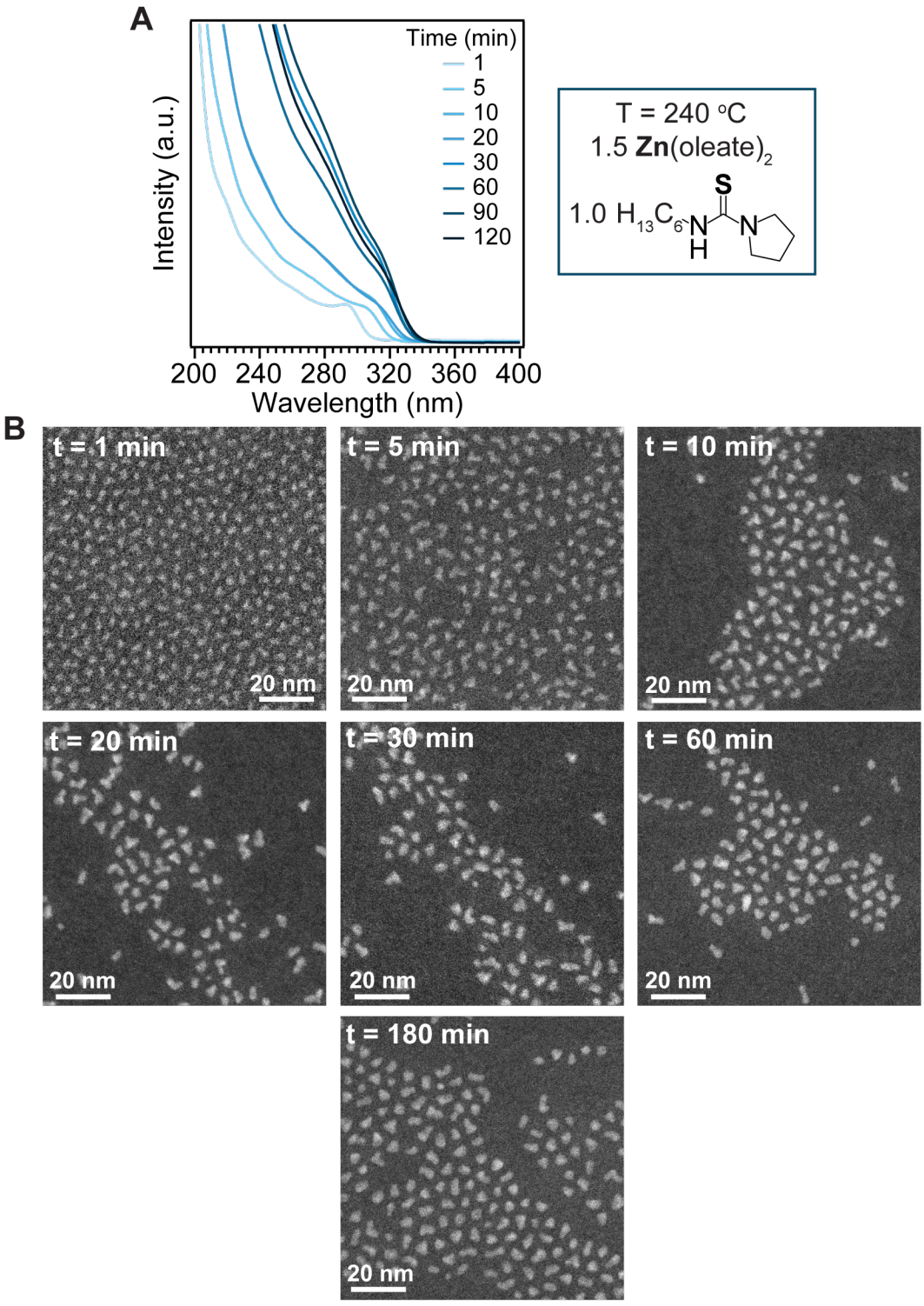

Figure S24. UV absorption spectra and STEM images of aliquots from the reaction between zinc oleate and **2e**. Reaction is completed after approximately 45 minutes.

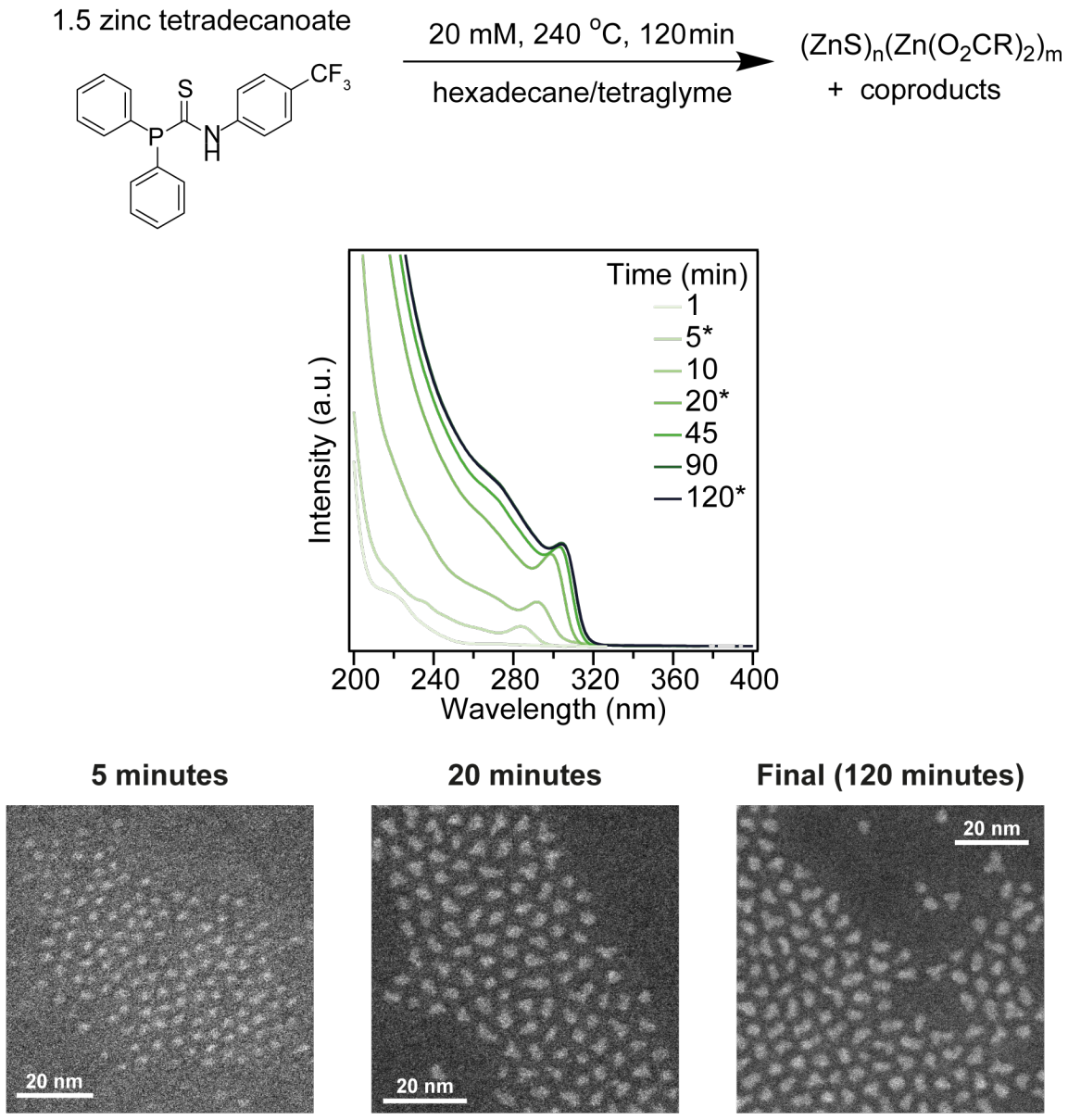

Figure S25. UV absorption spectra and STEM images of aliquots from the reaction between zinc tetradecanoate and **3b**. Interestingly, the absorption features are still fairly sharp eventhough zinc tetradecanoate was used in the synthesis and STEM shows the nanocrystals are not especially spherical. Reaction is completed after approximately 90 minutes. Use of zinc oleate instead sharpens the optical feature and leads to spherical nanocrystals (see Sizing sample 3).

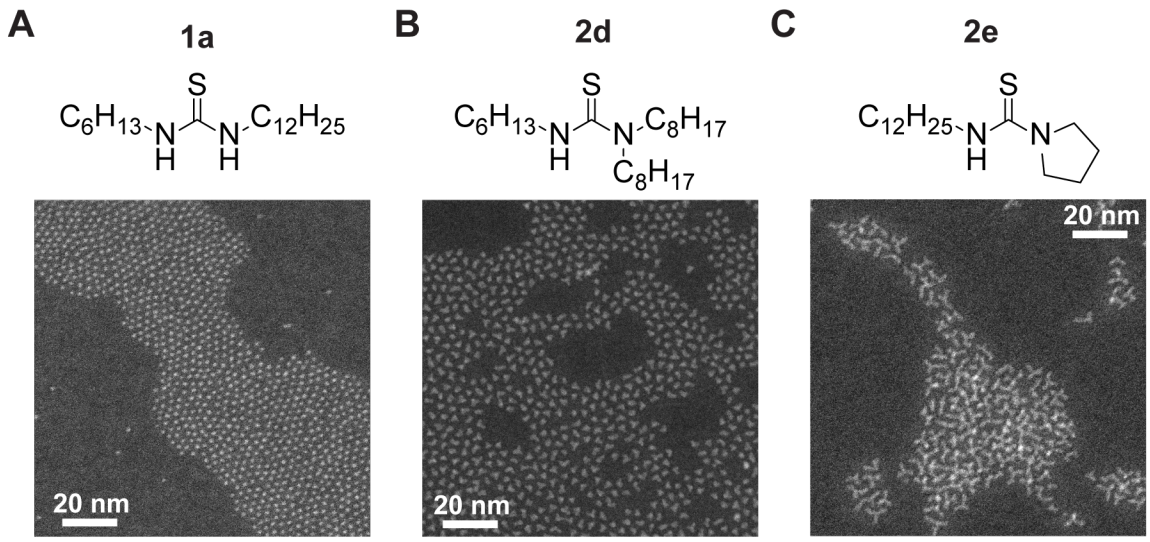

All: zinc tetradecanoate, T = 265 °C, t = 5 minutes

Figure S26. Thiourea precursor influence on ZnS shape when synthesized from zinc tetradecanoate. Shape differences are less pronounced when using zinc oleate (Figure S27).

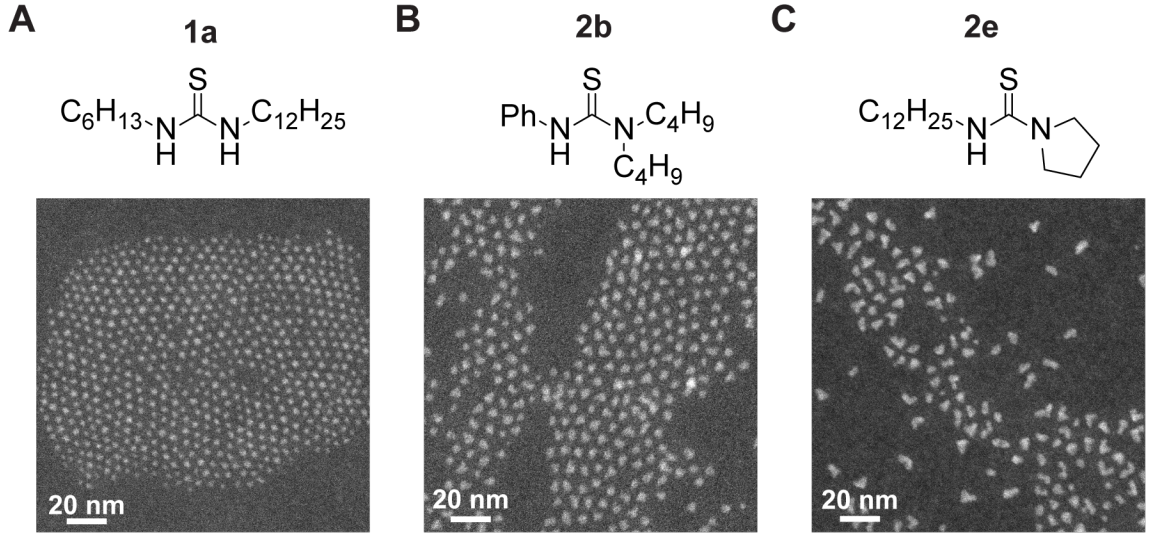

All: zinc oleate, T = 240 °C, t = 20 minutes

Figure S27. Thiourea precursor influence on ZnS shape when synthesized from zinc oleate.

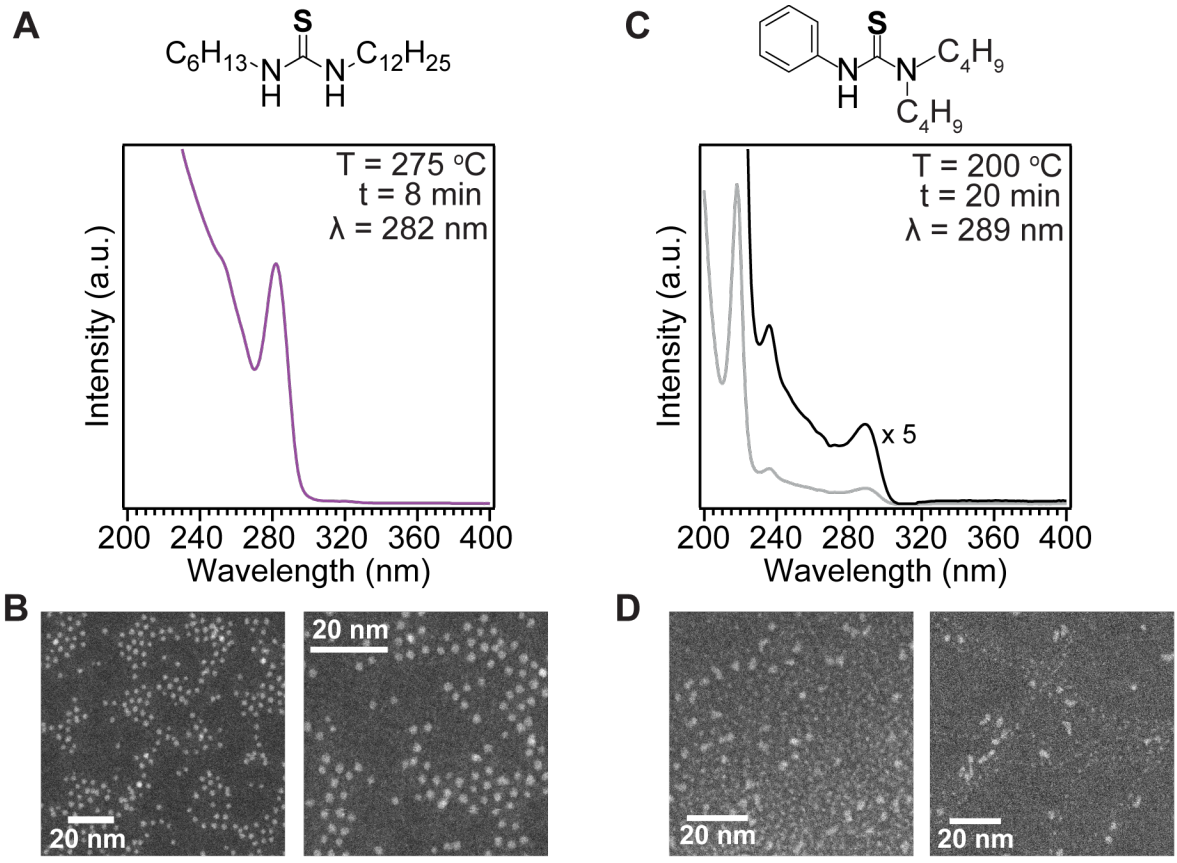

Figure S28. Comparison of similarly sized ZnS synthesized from different thiourea precursors. ZnS synthesized from the fast converting disubstituted **1a** resulted in a sharp optical feature (A) and spherical nanocrystals (B). Utilizing the slower **2b**, a reasonably well-defined excitonic feature was achieved (C), but STEM confirms the irregular growth of ZnS (D).

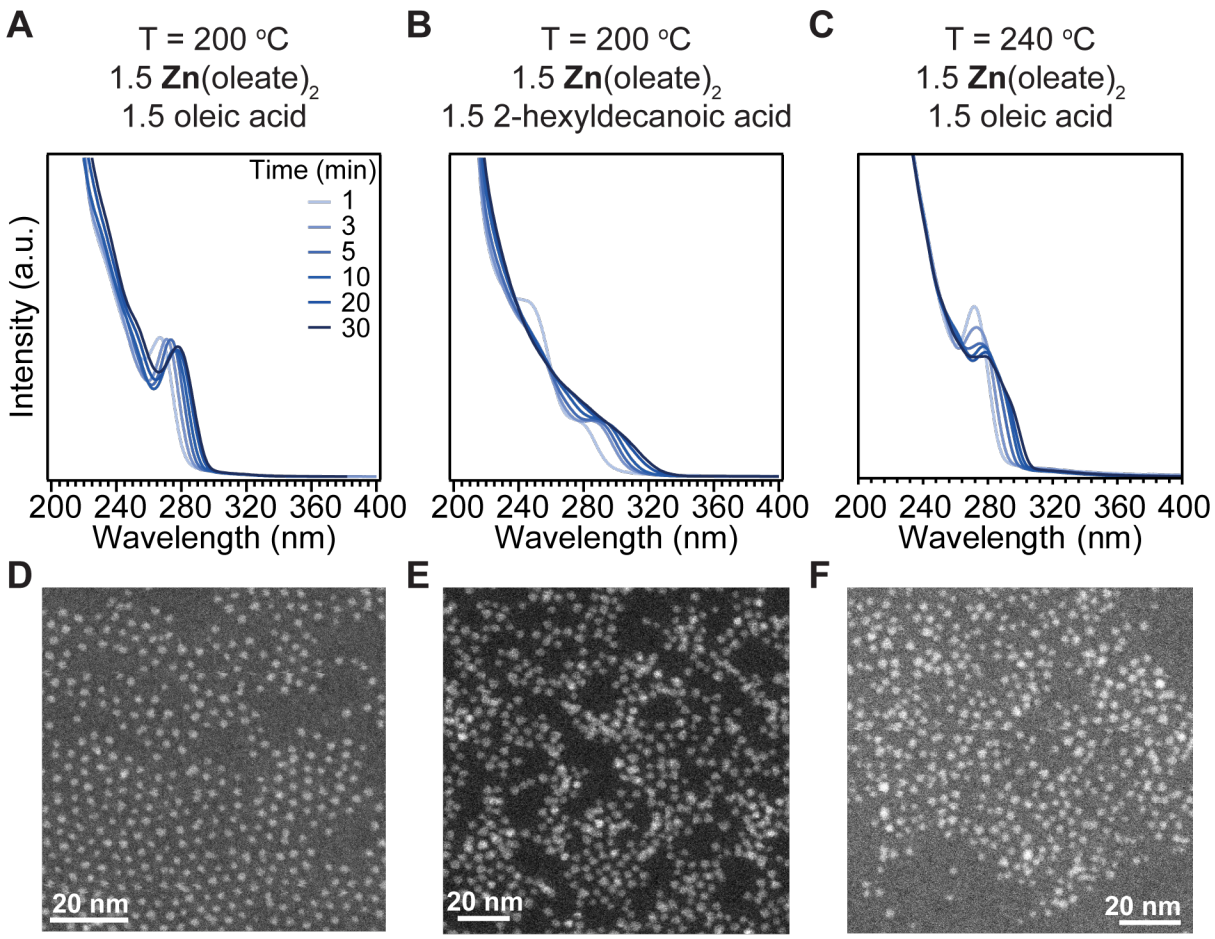

Figure S29. Impact of exogenous carboxylic acid on the shape of ZnS. Addition of oleic acid (A) and 2-hexyldecanoic acid (B) to reactions between zinc oleate and **1a** at 200 °C led to larger, but still spherical, nanocrystals. Increasing the temperature saw ripening occur to a greater extent and the polydispersity increase (C). However, the shape remained spherical.

Synthesis of ZnS with added acid. ZnS was synthesized using the method outlined for synthesis from zinc oleate in the main text, with the following modification: zinc oleate (0.226 g, 0.36 mmol, 1.5 equiv.), oleic acid (0.102 g, 0.36 mmol, 1.5 equiv.) and 1-octadecene (8.99 g, 11.4 mL) are loaded in a 50 mL 3-neck round bottom flask in an inert atmosphere

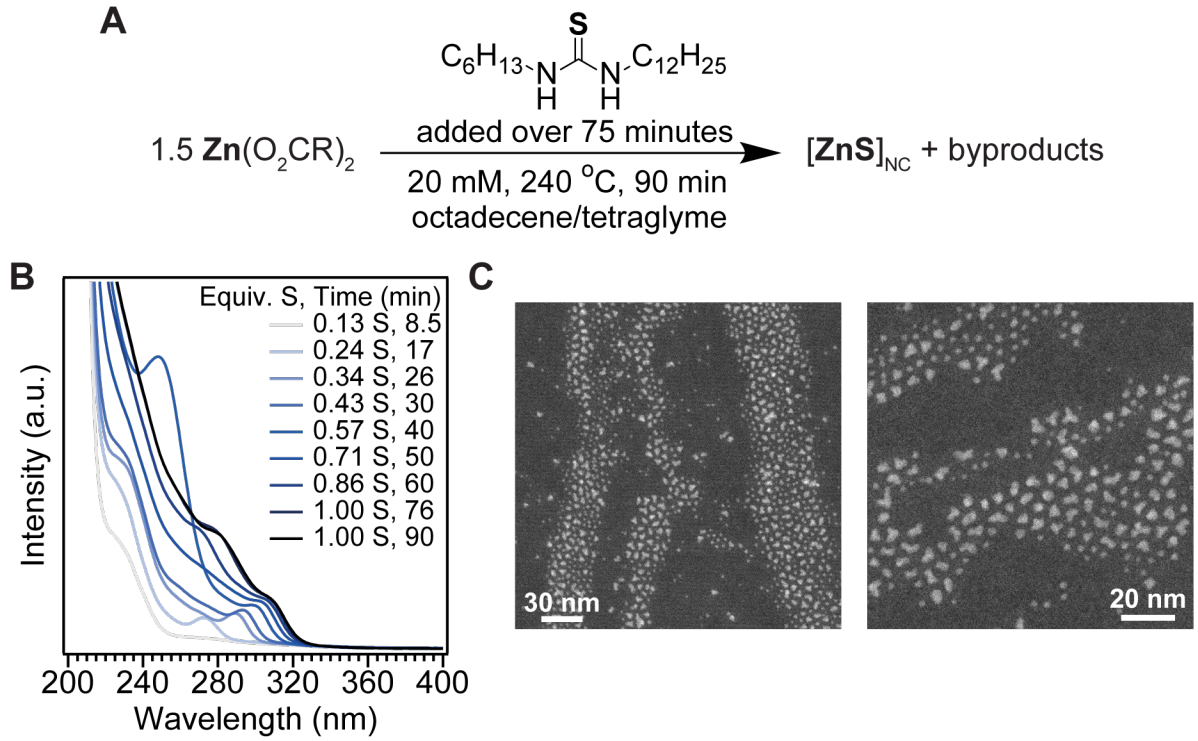

Figure S30. Synthesis of ZnS nanocrystals *via* slow injection of an *N,N'*-disubstituted thiourea. The solute supply from precursor **1a** was manually slowed down by slowly injecting the thiourea over the course of 75 minutes, instead of the usual single, fast injection which is complete in ~ 3 minutes. The evolution of the optical spectra are distinct from the fast-injection synthesis, with the peak significantly red-shifted indicating much larger ZnS are growing using this method (B). The addition rate was not optimized, and a clear second population appears after 30 minutes. STEM confirms the polydisperse sizes (C). Significantly, the large ZnS nanocrystals display anisotropy.

Synthesis of ZnS with slow addition of thiourea. In an inert atmosphere glovebox, zinc oleate (0.226 g, 0.36 mmol, 1.5 equiv.) and 1-octadecene (8.995 g, 11.4 mL) are added to a 50 mL 3-neck round bottom flask equipped with a stir bar and sealed with an air free vacuum adapter and two rubber septa. *N*-hexyl, *N*-dodecyl thiourea (0.079 mg, 0.24 mmol, 1 equiv.) and tetraglyme (0.6 mL) are added to a 4 mL vial and sealed with a rubber septum. The vessels are attached to an Argon inlet on a Schlenk line. The 3-neck flask is heated to 240 ˚C. Upon reaching temperature, the thiourea solution is slowly injected *via* syringe pump (~0.19 mmol/hr). The reaction is run for a total of 90 minutes before cooling to room temperature.

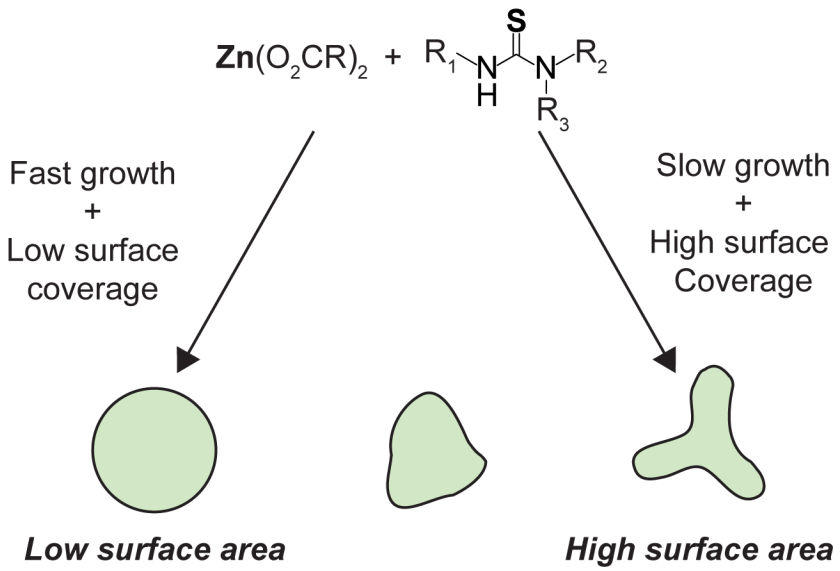

Figure S31. Factors impacting the shape of ZnS nanocrystals.

Section II - References

1. Hendricks, M. P.; Campos, M. P.; Cleveland, G. T.; Jen-La Plante, I.; Owen, J. S., A tunable library of substituted thiourea precursors to metal sulfide nanocrystals. *Science* **2015,** *348*, 1226-1230.
2. Yang, Y. A.; Wu, H.; Williams, K. R.; Cao, Y. C., Synthesis of CdSe and CdTe nanocrystals without precursor injection. *Angew Chem Int Ed Engl* **2005,** *44*, 6712-5.

Section III – Sizing Curve for ZnS

1. Literature survey of ZnS sizes

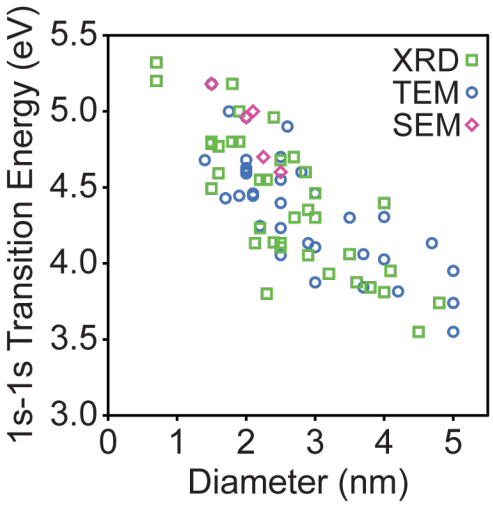

Figure S32. Survey of ZnS nanocrystal sizes and energies reported in the literature. Data used to generate this figure are included in Tables S3 – S5.

Table S3. Sizes from Literature Survey – TEM.

Reference	Bandgap from UV-vis		d (nm)	Method
	nm	eV		
Baruah *et al.*[1]	314	3.95	5	TEM
Shahid *et al.*[2]	253		2.6	TEM
Barman *et al.*[3]	309	3.74	5	TEM
Bochev *et al.*[4]	292		2.2	TEM
He *et al.*[5]	293		2.5	TEM
Vogel *et al.*[6]	265		1.4	TEM
Dumbrava *et al.*[7]	300		2.9	TEM
“	300		4.69	TEM
Wang *et al.*[8]	320		3	TEM
Chandrakar *et al.*[9]	269	4.60	2.8	TEM
“	260	4.70	2.5	TEM
“	250	4.96	2	TEM
“	248	5.00	1.75	TEM
“	239	5.18	1.5	TEM
Lu *et al.*[10]		4.05	2.5	TEM
“		3.84	3.7	TEM
Kho *et al.*[11]	274	4.53	6.08	TEM
Juine *et al.*[12]		4.46	3	TEM
“		4.06	3.7	TEM
“		3.55	5	TEM
Joo *et al.*[13]	310		11	TEM
Rossetti *et al.*[14]	269		2	TEM
Nanda *et al.*[15]	272	4.55	2.5	TEM
“	288	4.30	3.5	TEM
Nakaoka *et al.*[16]	293		2.5	TEM
“	280		1.7	TEM
“	302		3	TEM
“	282		4	TEM
“	308		4	TEM
“	288		4	TEM
“	270		2	TEM
“	268		2	TEM
“	279		2.1	TEM
“	279		1.9	TEM
“	282		2.5	TEM
“	278		2.1	TEM
Xia *et al.*[17]	265	4.68	2	TEM
Zhang *et al.*[18]	318		9.5	TEM
Zhao *et al.*[19]	325		4.2	TEM

Table S4. Sizes from Literature Survey – X-ray Techniques.

Reference	Bandgap from UV-vis		d (nm)	Method
	nm	eV		
Baruah *et al.*[1]	314	3.95	4.09	XRD
Barman *et al.*[3]	309	3.74	4.8	XRD
He *et al.*[5]	293		2.2	XRD
Dumbrava *et al.*[7]	300		2.5	XRD
“	300		2.13	XRD
Chandrakar *et al.*[9]	269	4.60	2.86	XRD
“	260	4.70	2.69	XRD
“	250	4.96	2.4	XRD
“	248	5.00	1.9	XRD
“	239	5.18	1.8	XRD
Lu *et al.*[10]		4.59	1.6	XRD
“		4.14	2.4	XRD
“		4.05	2.9	XRD
“		3.93	3.2	XRD
“		3.87	3.6	XRD
“		3.84	3.8	XRD
“		3.81	4	XRD
Kan *et al.*[20]	265		2.5	XRD
Juine *et al.*[12]		4.46	3	XRD
“		4.06	3.5	XRD
“		3.55	4.5	XRD
Mahamuni *et al.*[21]		5.20	0.7	XRD
“		4.80	1.5	XRD
“		3.80	2.3	XRD
Nakaoka *et al.*[16]	259		1.5	XRD
“	260		1.6	XRD
“	302		2.5	XRD
“	233		0.7	XRD
“	276		1.5	XRD
Nanda *et al.*[15]	260	4.80	1.8	XRD - small angle
“	272	4.55	2.2	XRD - small angle
“	288	4.30	3	XRD - small angle
Zhao *et al.*[19]	285		2.9	XRD - small angle
Nanda *et al.*[15]	260	4.80	1.9	XRD - wide angle
“	272	4.55	2.3	XRD - wide angle
“	288	4.30	2.7	XRD - wide angle

Table S5. Sizes from Literature Survey – SEM.

Reference	Bandgap from UV-vis		d (nm)	Method
	nm	eV		
Chandrakar *et al.*[9]	269	4.60	2.5	SEM
"	260	4.70	2.25	SEM
"	250	4.96	2	SEM
"	248	5.00	2.1	SEM
"	239	5.18	1.5	SEM

Note: this is a compilation for ZnS nanocrystals with d < 10 nm.

2. Synthetic Parameters for ZnS sizing samples

Table S6. Samples synthesized for sizing analysis (on following page).

* = included in sizing curve fit (samples 1 – 10, 12 – 17, 19 – 28)

[a] = Zn:S = 3:1

[b] = with 0.5 equivalents of oleic acid

$Zn(O_2CR)_2$ abbreviations: oleate = zinc oleate, tetradec. = zinc tetradecanoate, 2-HD = zinc 2-hexyldecanoate.

Solvent abbreviations: ODE = 1-octadecene, HEX = hexadecane.

The following table includes all samples considered for the sizing curve. It lists the energy, error and *hwhm* of the 1s-1s transition energy (in nm and eV). Also included are the synthetic parameters used to synthesize the samples: precursors, solvent, reaction time and temperature. The samples marked with an * represent those used in the sizing curve fit. See discussion later on how samples were selected.

Sample ID	nm			eV			Synthesis				
	Peak	± error	HWHM	Peak	± error	HWHM	TU	$Zn(O_2CR)_2$	solvent	T (°C)	t (min)
1*	267	1	10	4.64	0.017	0.17	1a	oleate	ODE	220	1
2*	291	1	9	4.26	0.015	0.13	2b	oleate	ODE	200	60
3*	287	1	8	4.32	0.015	0.12	3a	oleate	ODE	200	45
4*	285	1	10	4.35	0.015	0.15	2a	oleate	ODE	200	10
5*	292	1	9	4.25	0.015	0.13	2c	oleate	ODE	200	120
6*	300	2	13	4.13	0.069	0.11	2b	tetradec.	HEX	265	30
7*	305	2	10	4.07	0.027	0.13	2d	tetradec.	HEX	265	5
8*	274	1	9	4.52	0.017	0.14	1a	tetradec.	HEX	265	1.5
9*	284	1	8	4.37	0.015	0.12	1a	tetradec.	HEX	260	10
10*	273	1	9	4.54	0.017	0.15	1a	tetradec.	HEX	180	10
11	297	2	9	4.17	0.028	0.12	2b	tetradec.	HEX	200	60
12*	306	2	9	4.05	0.026	0.12	2b	tetradec.	HEX	240	60
13*	306	3	8	4.05	0.040	0.10	1a	2-HD	ODE	240	30
14*,[a]	297	2	7	4.17	0.028	0.10	1b	tetradec.	HEX	240	90
15*	266.5	1	10	4.65	0.017	0.17	1a	tetradec.	HEX	220	5
16*	281	1	11	4.41	0.016	0.17	1a	oleate	ODE	240	30
17*	314	2	9	3.95	0.025	0.11	1a	2-HD	HEX	265	30
18	316	3	14	3.92	0.037	0.17	2e	2-HD	HEX	265	30
19*,[b]	278	1	11	4.46	0.016	0.17	1a	oleate	ODE	200	30
20*	282	1	8	4.40	0.016	0.12	1a	tetradec.	HEX	275	8
21*	300	2	8	4.13	0.028	0.11	2g	oleate	ODE	240	20
22*	301	2	8	4.12	0.027	0.11	2g	oleate	ODE	240	30
23*	302	2	8	4.11	0.027	0.11	2g	oleate	ODE	240	60
24*	303	2	8	4.09	0.027	0.11	2g	oleate	ODE	240	90
25*	303	2	8	4.09	0.027	0.11	2g	oleate	ODE	240	135
26*	299	2	9	4.15	0.028	0.12	2f	oleate	ODE	240	20
27*	301	2	9	4.12	0.027	0.12	2f	oleate	ODE	240	30
28*	301	2.5	7	4.12	0.034	0.28	1a	2-HD	HEX	240	20
29	301	2	9	4.12	0.027	0.12	2b	tetradec.	HEX	240	25
30	302	2	9	4.11	0.027	0.12	2b	tetradec.	HEX	240	60
31	299	2	9	4.15	0.028	0.12	2b	tetradec.	HEX	220	90
32	277.5	1	8	4.46	0.016	0.12	1a	tetradec.	HEX	265	3
33	269	1	10	4.61	0.017	0.17	1d	oleate	ODE	200	30
34	283	1	9	4.38	0.015	0.14	3a	oleate	ODE	200	45
35	292	2	10	4.25	0.029	0.14	2a	oleate	ODE	200	90
36	293	2	8	4.23	0.029	0.11	2b	oleate	ODE	200	75
37	294	2	10	4.22	0.029	0.14	2b	oleate	ODE	200	60
38	296	2	11	4.19	0.028	0.15	2a	oleate	ODE	220	60
39	310	5	10	4.00	0.039	0.12	2d	oleate	ODE	240	30

Table S7. Sizing methods for each sample.

Sample ID	Sizing Techniques	
	PDF	(S)TEM
1*	✓	✓
2*	✓	✓
3*	✓	✓
4*	✓	✓
5*	✓	✓
6*		✓
7*	✓	✓
8*	✓	✓
9*	✓	✓
10*	✓	✓
11	✓	✓
12*	✓	✓
13*		✓
14*,[a]	✓	✓
15*		✓
16*		✓
17*		✓
18		✓
19*,[b]		✓
20*		✓
21*		✓
22*		✓
23*		✓
24*		✓
25*		✓
26*		✓
27*		✓
28*		✓
29		✓
30	✓	✓
31		✓
32	✓	✓
33	✓	
34		✓
35		✓
36		✓
37		✓
38		✓
39		✓

3. X-ray Total Scattering experiments

The experimental geometry, 2θ range, and detector misorientations were calibrated by measuring a crystalline nickel powder directly prior to the ZnS nanocrystals, with the experimental geometry parameters refined using the Fit2D program[22]. Standardized corrections are then made to the data to obtain the total scattering structure functions:

$$\mathrm{S(Q)} = \frac{\mathrm{I(Q)} + \langle f(Q)\rangle^2 - \langle f^2(Q)\rangle}{\langle f(Q)\rangle^2} \text{ and } F(Q) = Q(S(Q) - 1),$$

which is then directly Fourier transformed to obtain the reduced PDF G(r) as:

$$G(r) = \frac{2}{\pi}\int_{Qmin}^{Qmax} F(Q)Sin(Qr)\, dQ$$

using PDFgetX3[23] within xPDFsuite[24]. The maximum and minimum range of data used in the Fourier transform (Q_{max}/Q_{min}), where:

$$\frac{Q \;=\; 4\pi \sin\theta}{\lambda}$$

is the magnitude of the momentum transfer on scattering, was chosen to give the best trade-off between statistical noise and real-space resolution.

Pair Distribution Function Analysis Modelling

For single phase fits, one independent lattice parameter is refined for the zincblende phase and two independent lattice parameters are refined for the wurtzite phase in order to preserve space group symmetry for each phase. Isotropic thermal displacement parameters are refined for Zn and S atoms in the unit cell of each phase. To account for nanoscale finite size effects on the PDF we refine a diameter of a spherical envelope function.[25] Correlated atomic motion was treated by optimizing an empirical quadratic correlated atomic motion correction factor.[26] An overall scale factor for the data is also optimized for the fit. The wurtzite and zincblende phase fractions were calculated refining independently a scale factor X which was fit for the zincblende phase which constrained the value of the wurtzite scale factor which was defined as $(1 - X)$ and a shared spherical envelope function diameter for both phases.[27] An overall scale factor for the data is also optimized for the fit. Other parameters were taken from the single-phase fits to avoid overparameterization of the two-phase model.

Table S8. PDF Analysis Results.

Sample ID	Peak Energy		2-phase model			Pure ZB model		
	(nm)	(eV)	*r* (nm)	*d* (nm)	R_w	*r* (nm)	*d* (nm)	R_w
1#	267	4.64	0.84	1.68	0.30	0.70	1.40	0.36
2#	291	4.26	1.10	2.20	0.23	0.89	1.78	0.32
3#	287	4.32	1.05	2.09	0.22	0.85	1.70	0.31
4#	285	4.35	0.97	1.95	0.38	0.84	1.68	0.42
5#	292	4.25	1.09	2.17	0.30	0.89	1.77	0.35
7	305	4.07	1.17	2.34	0.19	1.02	2.05	0.24
8	274	4.52	0.94	1.89	0.21	0.80	1.59	0.25
9	284	4.37	1.08	2.16	0.19	1.00	2.00	0.21
10	273	4.54	0.95	1.90	0.20	0.81	1.63	0.24
11	297	4.17	1.15	2.30	0.20	1.00	1.99	0.24
12	306	4.05	1.25	2.49	0.20	1.13	2.26	0.24
14	297	4.17	1.25	2.51	0.19	1.03	2.05	0.25
30	302	4.11	1.26	2.53	0.19	1.04	2.07	0.25
32	277.5	4.46	0.98	1.96	0.19	0.82	1.64	0.25
33#	269	4.61	0.90	1.79	0.27	0.74	1.47	0.34

PDF samples 1-5 and 33 – denoted with # – were collected at a separate beam time to the others.

d = crystallite size extracted from PDF. Here, we use this as an estimate for the nanocrystal diameter.

r = radius (diameter/2).

R_w = goodness-of-fit measurement for the PDF model.

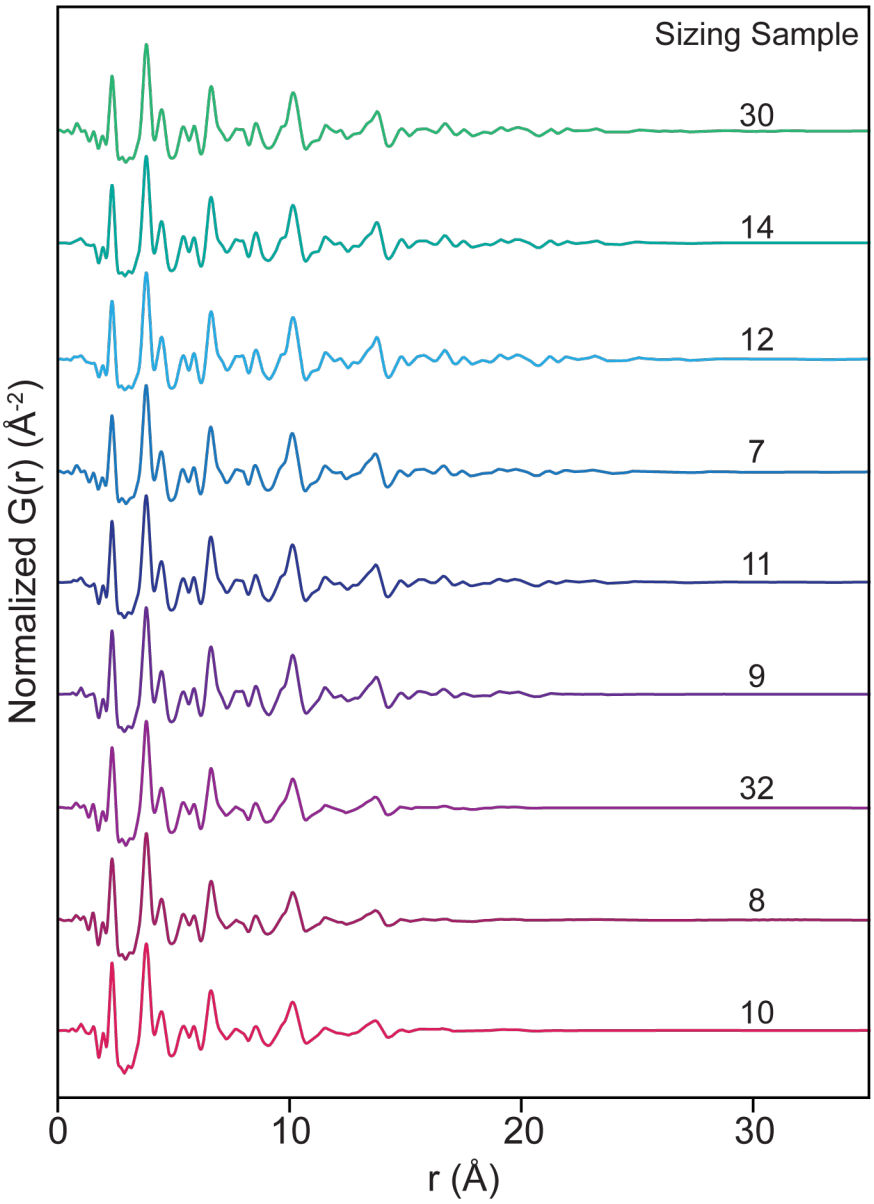

Figure S33. Representative normalized PDF data.

Sample 10

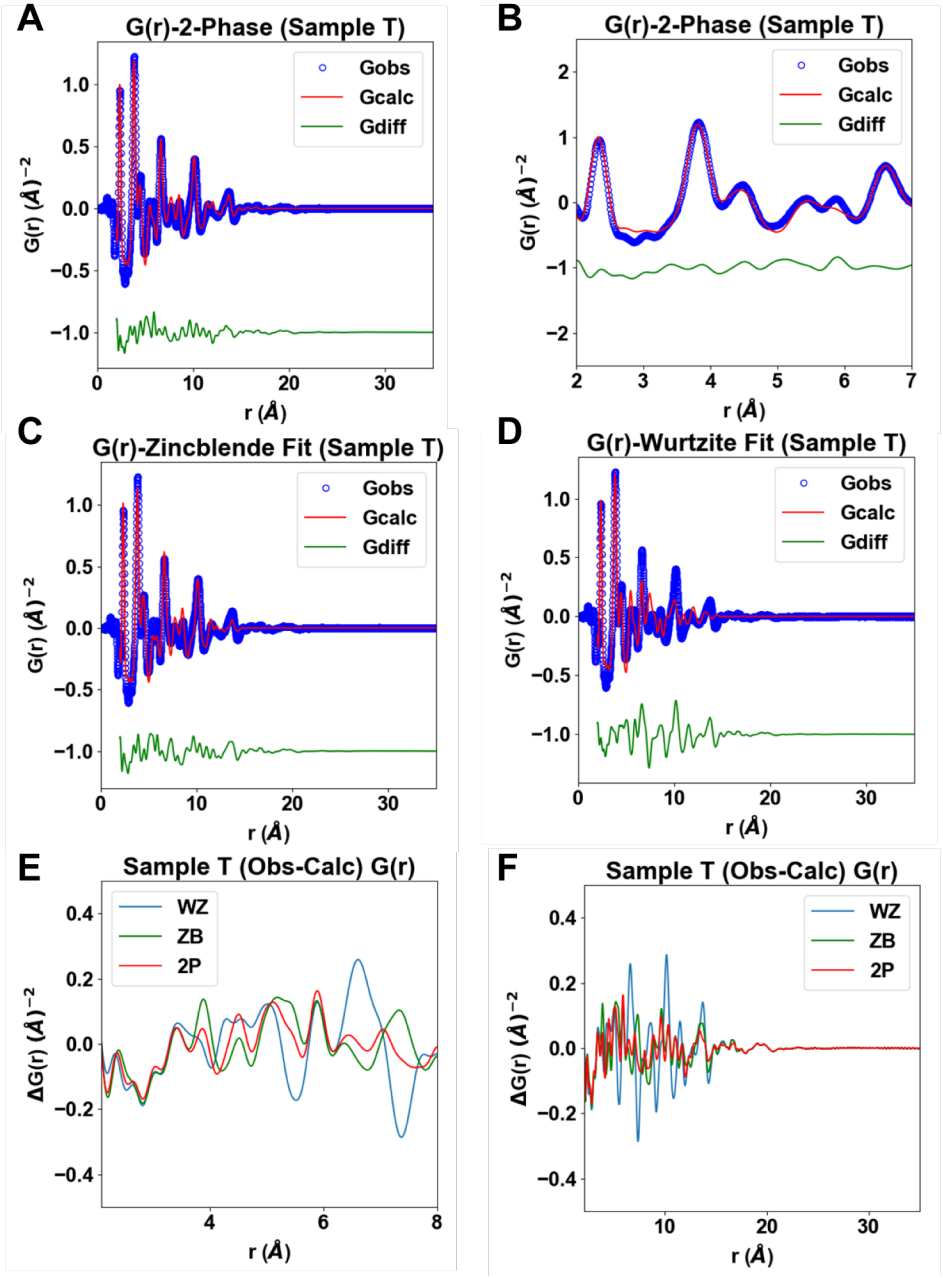

Figure S34. PDF fits for sample 10. The data is fit using a 2-phase (A-B), pure zinc blende (C), and pure wurtzite (D) models. The crystallite size obtained from the 2-phase fit gives d = 1.9 nm. The fit residuals are shown in E-F.

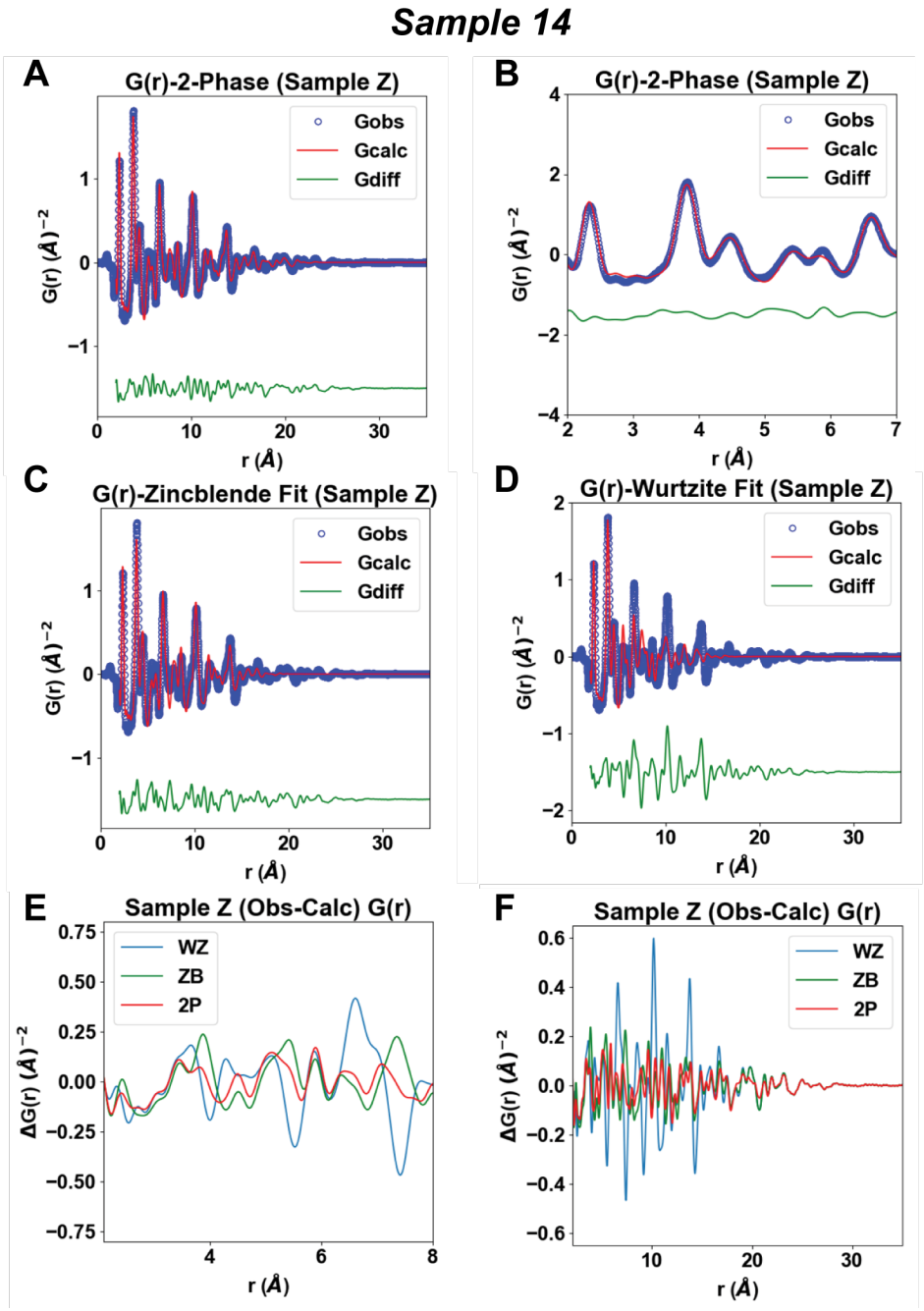

Figure S35. PDF fits for sample 14. The data is fit using a 2-phase (A-B), pure zinc blende (C), and pure wurtzite (D) models. The crystallite size obtained from the 2-phase fit gives d = 2.5 nm. The fit residuals are shown in E-F.

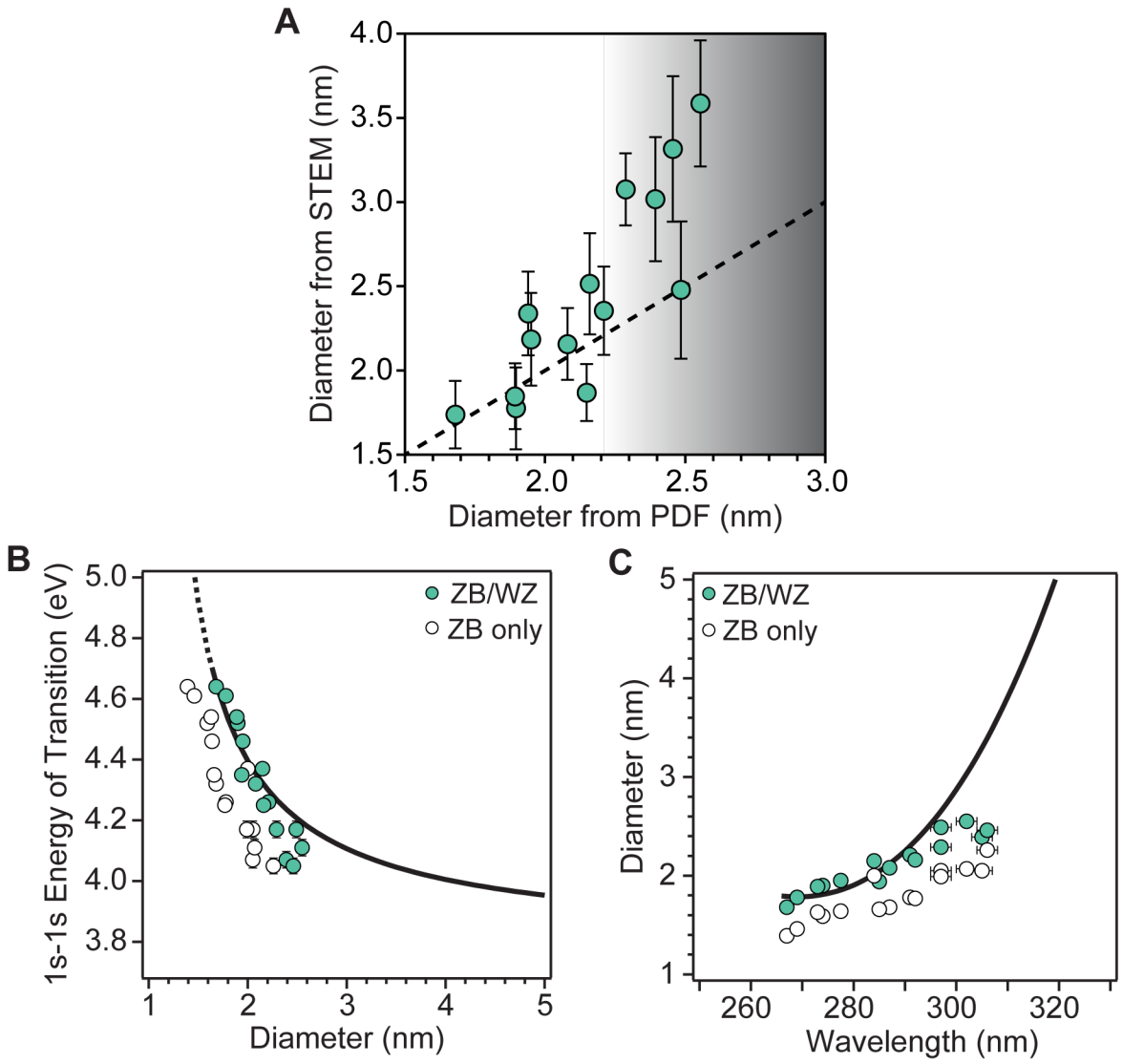

Figure S36. At small nanocrystal sizes (d < 2.3 nm), the diameter estimated by STEM and PDF are in agreement, but at larger sizes PDF underestimates the ZnS size (A). Diameters extracted using the 2-phase model (green) and pure zinc blende model (white) from PDF analysis plotted against the 1s – 1s transition energy (B) and wavelength (C). The sizing curve is shown in black. At sizes > ~ 2.2 nm, the PDF sizes diverge from the sizing curve.

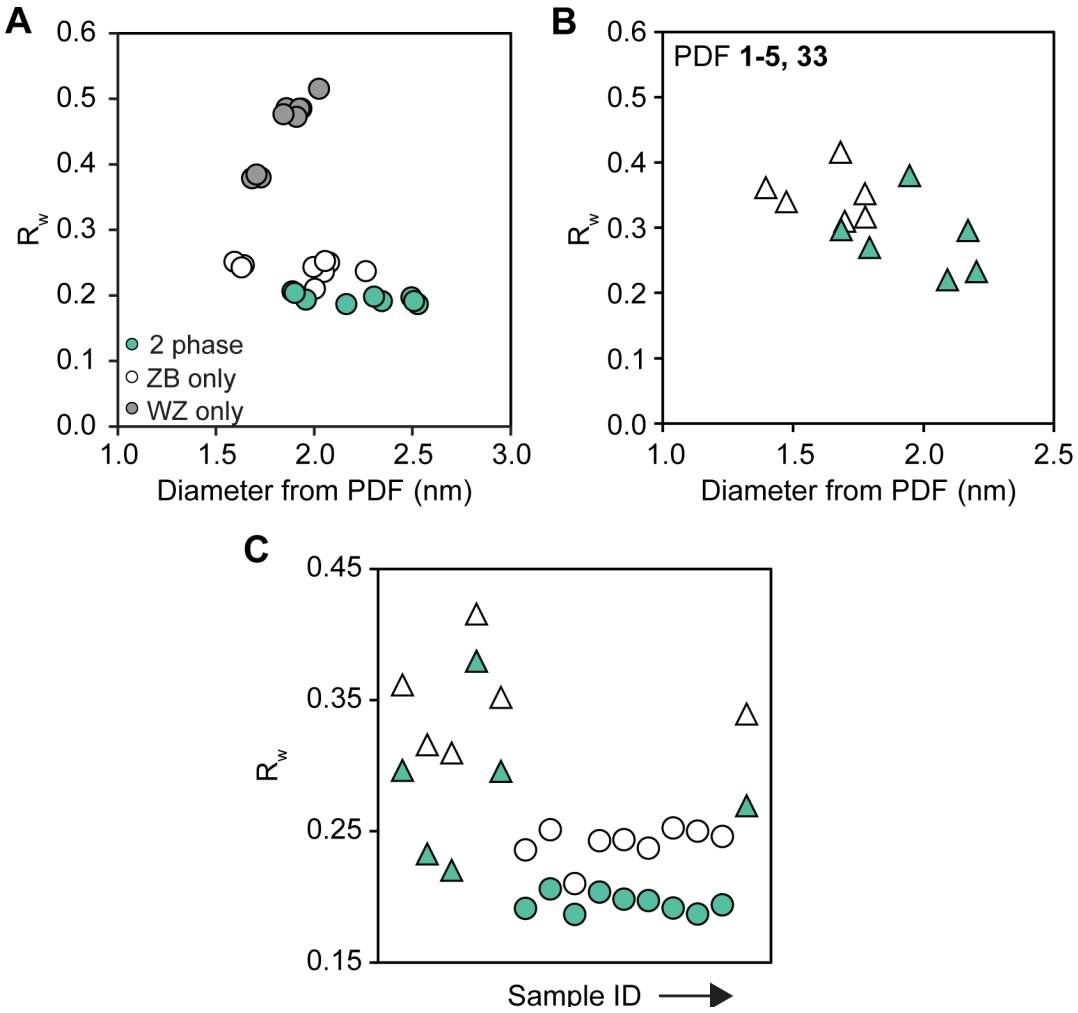

Figure S37. R_w (goodness of fit) values for the 2-phase model (green), pure zinc blende (white), and pure wurtzite (grey) models. Samples 1-5 and 33 are plotted separately in (B) as they were acquired at a separate beam time to the other samples (A). For each ZnS sample, the 2-phase model results in a larger extracted crystallite size and a lower R_W value than either of the single phase models. This is best demonstrated in (C) where the R_W values are plotted against Sample ID, where the ID number is increasing left to right (samples 1-5, 7-12, 14, 30, 32-33 in Table S8).

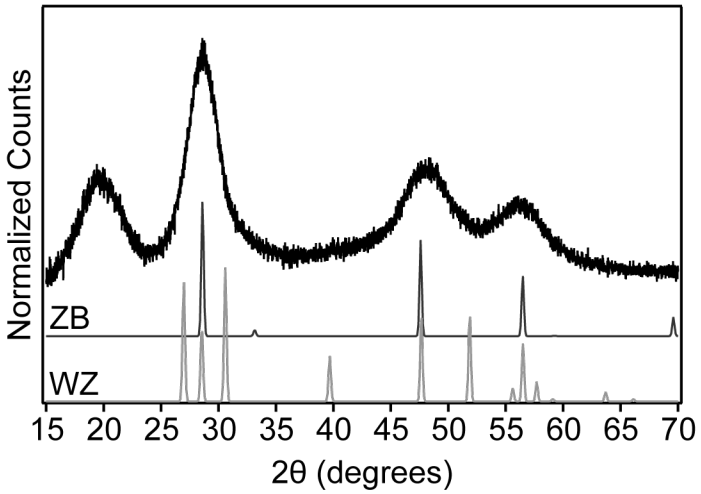

Figure S38. Powder X-ray diffraction (pXRD) appears zinc blende however the significant peak broadening means the detection of wurtzite is challenging. The feature at 2θ ~ 20° is assigned to polymer impurities and metal carboxylates.

4. Determination of ZnS size using HAADF-STEM and TEM

Imaging ZnS with electron microscopy techniques is challenging due to poor contrast between nanocrystal and background, particularly compared to other semiconductor nanocrystals such as CdS and PbS. This lack of contrast is due to the weaker interaction between the electron beam and the ZnS lattice. As such, traditionally used transmission electron microscopy (TEM) is not adequate for accurately determining ZnS shapes or sizes. Therefore, we predominantly use high-angle annular dark-field scanning transmission electron microscopy (HAADF-STEM), which achieves greater contrast between the nanocrystal and image background, for determining the size and size distributions in our samples. For ease, we refer to this simply as STEM throughout.

Sizing analysis was done using ImageJ. The image was imported as a .tif file, and the scale was set using the scale bar from the micrograph. For most samples, the contrast was too low to reliably apply a threshold to (i.e. transform image to black and white, with nanocrystals in black and background in white). Nanocrystals were not successfully separated from the background with this technique, meaning the particle sizes could not be extracted in this way. Hence, the particle selection was undertaken manually.

Nanocrystal Size Determination

For the samples containing nanocrystals appearing uniform and spherical, nanocrystals were selected individually using the circle tool. They were drawn such that the edges of the circle reached what was judged as the edge of the particle. Occasionally, an oval or polygon was used if it were deemed more appropriate. The area of each particle was measured, and from this a radius calculated from a circle with the same area:

$$r = \sqrt{\frac{Area}{\pi}}$$

Highly anisotropic nanocrystals were not analyzed in this manner, and are not included in the sizing curve fit.

Assessment of potential sources of error

All sizing was done by the same individual and carried out as systematically as possible. With the nanocrystals being selected manually, there is likely to be error introduced. To help counter this, as many nanocrystals as possible (given the acquied images) were analyzed and, for the smallest nanocrystals where we would expect the error to have the biggest impact on extracted size, PDF analysis was used to confirm the STEM results.

In addition to counting many nanocrystals per sample, only the highest magnification STEM images for each sample were used. We found that, for the same ZnS sample, analysis completed on micrographs acquired at a higher magnificiation (630 kx) consistently yielded average radius measurements of approximately 0.1 - 0.2 nm smaller than analysis completed on micrographs acquired at lower magnifications (320 or 450 kx) (Figure S39), consistent with a report from Pyrz and Buttrey.[28] We attribute this to the combination of it being harder to get the exact perimeter of the nanocrystal at lower magnifications, and each pixel representing a larger area (than at higher magnification), leading to a larger diameter being calculated. Together, these factors likely explain the systematic differences we see. We find that these sizes acquired from the higher magnification

are in closer agreement to the sizes obtained from PDF analysis, and therefore all sizing was completed on micrographs with the highest magnification form each sample.

Assessing the percent size dispersity

Many of the smaller samples analyzed in this way had distributions with the standard deviation in the diameter similar to the length of a Zn-S bond ($\sigma \sim 0.2 – 0.3$ nm, $r_{Zn\text{-}S} \sim 0.2$ nm). In addition, for the 630 kx samples, the dispersity (σ/d, as a percentage) mostly lay between 8.1 – 12.3 %, indicating good monodispersity in the sample (Figure S11). Interestingly, samples with higher dispersity values were synthesized from zinc 2-hexyldecanoate (Table S9: **13** 17.8 %, **18** 13.3 %, **28** 14.4 %) or from an initial Zn:S ratio of 3:1 (**14** 15.1 %). The results with zinc 2-hexyldecanoate point to ligand binding ability being a tool to control monodispersity.

Sizing Curve

ZnS samples used to create the sizing curve fulfilled the following criteria:

(1) Obtained using STEM mode.
(2) Obtained using 630 kx magnification (highest possible while still able to achieve good contrast).
(3) Quasi-spherical nanocrystals (approximated by circle or oval).

Any samples with signifcant shape anisotropy were not included.

In total, 26 samples were used to create the sizing curve, denoted by * in Table S9. During STEM analysis, efforts were made to count as many nanocrystals as possible, given the above criteria. For 21 samples, > 300 NCs were sampled (range: 314 – 1102 NCs/sample). For 5 samples, there were not enough micrographs to reach the suggested 300 NC threshold, instead analysis contained between 138 – 199 NCs/sample. Exclusion of these 5 samples from the sizing curve fit (described below) does not signifcantly alter the sizing curve coefficients. Compared to the sizing curve presented in the manuscript using all 26 samples, the sizing curve with the 5 excluded data points yields a maximum deviation in calculated bandgap energy of -0.1% from the original fit. As such, we included all 26 points in our sizing curve analysis.

For completeness, below we also include the data obtained from lower magnification (360 – 450 kx) STEM (Table S10) and TEM (Table S11) analysis. The poorer contrast afforded from TEM meant that there were fewer nanocrystals per micrograph where the particle edge (and therefore size) could be confidently determined. As such, fewer nanocrystals were counted for the TEM sizing histograms compared to the STEM, and there is likely a larger error associated with the sizes. As expected given the magnification discussion above, the samples analyzed using 360 – 450 kx STEM magnification, for a given peak energy, the average diameter turned out *slightly larger* than the sizing curve obtained from the fits to the 630 kx data points.

Figures S41 and S42 show a comparison between the different electron microscopy techniques and the determined sizing curves (eV vs d and d vs λ).

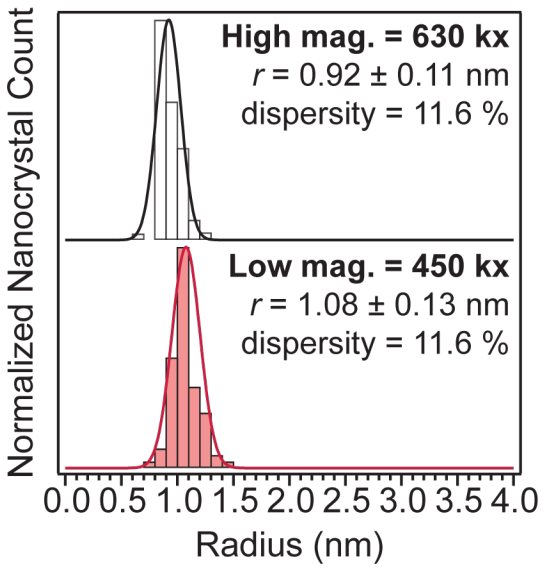

Figure S39. Comparison of nanocrystal sizing using 630 kx and 450 kx magnification.

Table S9. STEM high magnification (630 kx) sizing data.

	nm			eV			EM imaging			
New ID	Peak	± error	HWHM	Peak	± error	HWHM	d	d(σ)[a]	%[b]	# NCs
1*	267	1	10	4.64	0.017	0.17	1.74	0.20	11.5	573
2*	291	1	9	4.26	0.015	0.13	2.36	0.26	11.1	317
3*	287	1	8	4.32	0.015	0.12	2.16	0.21	9.9	1000
4*	285	1	10	4.35	0.015	0.15	2.34	0.25	10.6	356
5*	292	1	9	4.25	0.015	0.13	2.52	0.30	11.9	334
6*	300	2	13	4.13	0.069	0.11	3.09	0.37	11.9	406
7*	305	2	10	4.07	0.027	0.13	3.02	0.24	8.1	391
8*	274	1	9	4.52	0.017	0.14	1.78	0.17	9.5	1102
9*	284	1	8	4.37	0.015	0.12	1.87	0.19	10.4	736
10*	273	1	9	4.54	0.017	0.15	1.85	0.21	11.6	423
11	297	2	9	4.17	0.028	0.12	3.08	0.43	14.1	90
12*	306	2	9	4.05	0.026	0.12	3.31	0.41	12.3	199
13*	306	3	8	4.05	0.040	0.10	3.81	0.62	16.3	401
14*	297	2	7	4.17	0.028	0.10	2.48	0.37	15.1	813
15*	266.5	1	10	4.65	0.017	0.17	1.81	0.16	8.9	138
16*	278	1	11	4.46	0.016	0.17	1.89	0.19	10.0	187
17*	314	3	9	3.95	0.038	0.11	4.47	0.50	11.1	638
18	316	5	14	3.92	0.050	0.17	10.06	1.34	13.3	332
19*	278	1	11	4.46	0.016	0.17	1.83	0.20	11.0	844
20*	282	1	8	4.40	0.016	0.12	1.91	0.17	8.9	167
21*	300	2	8	4.13	0.028	0.11	2.71	0.24	8.7	380
22*	301	2	8	4.12	0.027	0.11	2.88	0.29	10.0	243
23*	302	2	8	4.11	0.027	0.11	2.94	0.29	9.9	144
24*	303	2	8	4.09	0.027	0.11	2.96	0.27	9.3	492
25*	303	2	8	4.09	0.027	0.11	2.94	0.32	10.8	391
26*	299	2	9	4.15	0.028	0.12	3.01	0.32	10.7	399
27*	301	2	9	4.12	0.027	0.12	3.03	0.30	10.1	314
28*	301	2.5	7	4.12	0.034	0.28	2.92	0.42	14.4	404

*denotes sample is used for sizing curve fit.

[a]d(σ) is the standard deviation in the nanocrystal diameter.

[b]% is the percent size dispersity measured (σ/d, %).

Table S10. STEM low magnification (450 kx) sizing data.

	nm			eV			EM imaging			
New ID	Peak	± error	HWHM	Peak	± error	HWHM	d	d(σ)[a]	%[b]	# NCs
29	301	2	9	4.12	0.027	0.12	3.27	0.35	10.6	222
30	302	2	9	4.11	0.027	0.12	3.58	0.28	7.7	250
31	299	2	9	4.15	0.028	0.12	3.39	0.41	12.0	206
32	277.5	1	8	4.46	0.016	0.12	2.19	0.18	8.2	274

[a]d(σ) is the standard deviation in the nanocrystal diameter.

[b]% is the percent size dispersity measured (σ/d, %).

Table S11. TEM sizing data.

	nm			eV			EM imaging			
New ID	Peak	± error	HWHM	Peak	± error	HWHM	d	d(σ)[a]	%[b]	# NCs
34	283	1	9	4.38	0.015	0.14	2.19	0.25	11.4	76
35	292	2	10	4.25	0.029	0.14	2.84	0.34	12.1	50
36	293	2	8	4.23	0.029	0.11	2.51	0.24	9.7	105
37	294	2	10	4.22	0.029	0.14	2.98	0.29	9.7	50
38	296	2	11	4.19	0.028	0.15	3.06	0.30	9.7	95
39	310	5	10	4.00	0.065	0.12	3.33	0.36	10.9	212

[a]d(σ) is the standard deviation in the nanocrystal diameter.

[b]% is the percent size dispersity measured (σ/d, %).

5. ZnS sizing curves and discussion

Sizing Curve: *λ vs d*

Additionally, we fit the relationship between λ and *d*, described well by:

$$d = \alpha + \beta\lambda + \gamma\lambda^2 + \delta\lambda^3$$

where *α, β, γ* and *δ* are fitting parameters summarized in Table S12:

Table S12. Fitting parameters for sizing curve relating ZnS diameter (*d*) to peak wavelength (*λ*).

α (nm)	7.288×10^{-6}
β	-4.9749×10^{-3}
γ (nm^{-1})	1.0943
δ (nm^{-2})	-7.4454×10^{1}

Again, the line is fit only to the high magnification STEM data.

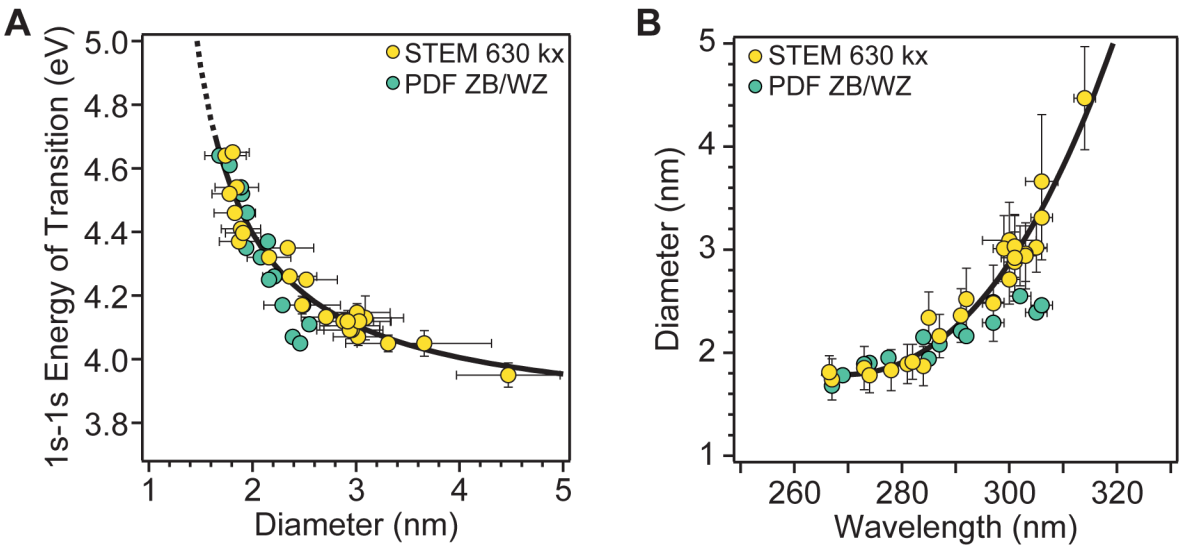

Figure S40. Sizing curves for ZnS. Sizing curve relating $E_{1s\text{-}1s}$ to diameter (A) and diameter to peak wavelength (B). Lines are fitted to STEM data (yellow), with PDF (green) plotted to show the agreement at low sizes.

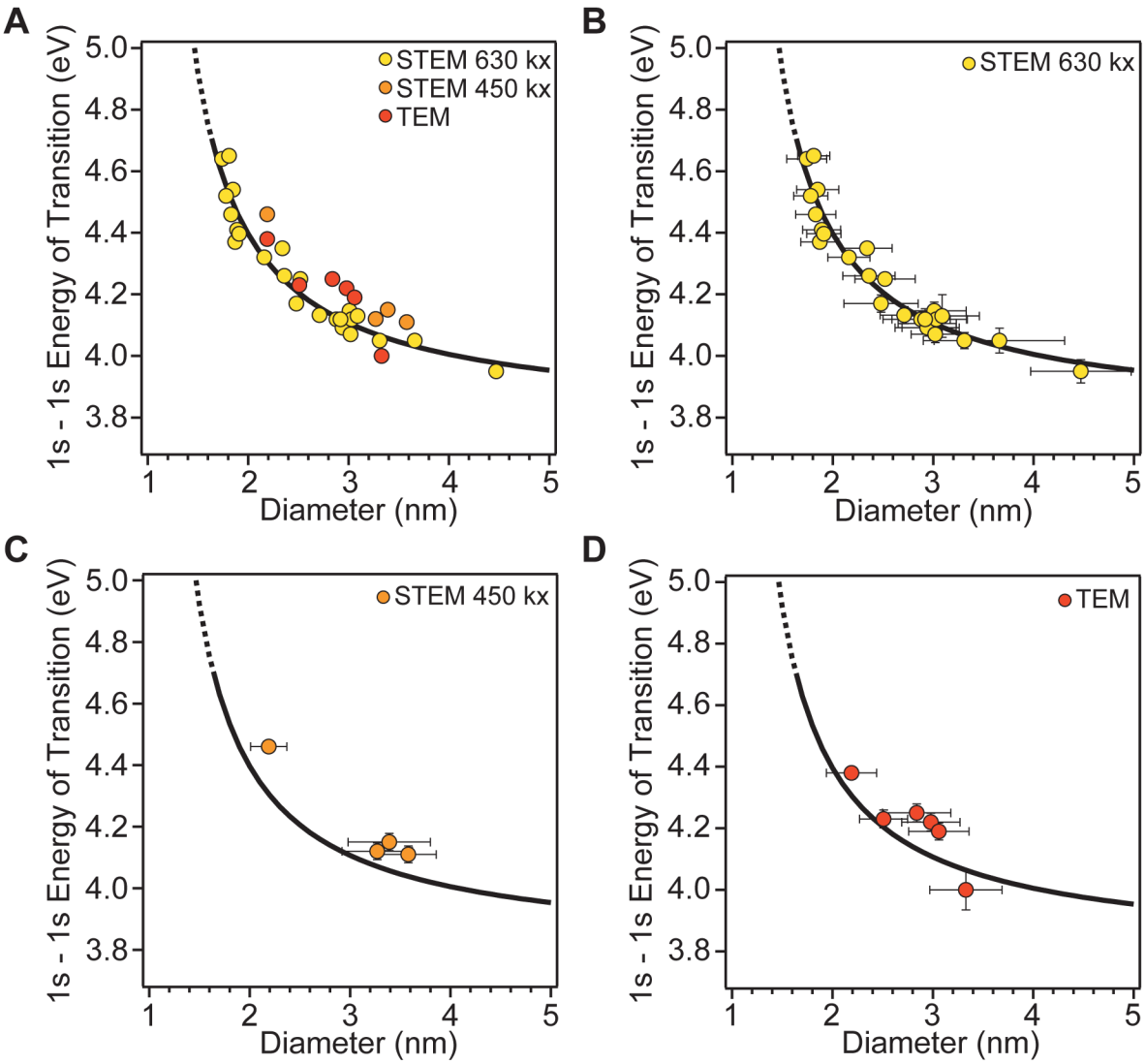

Figure S41. $E_{1s\text{-}1s}$ plotted as a function of measured nanocrystal size for all electron microscopy results (A), highest magnification STEM (630 kx, B), lower magnification STEM (450 kx, C), and TEM (D).

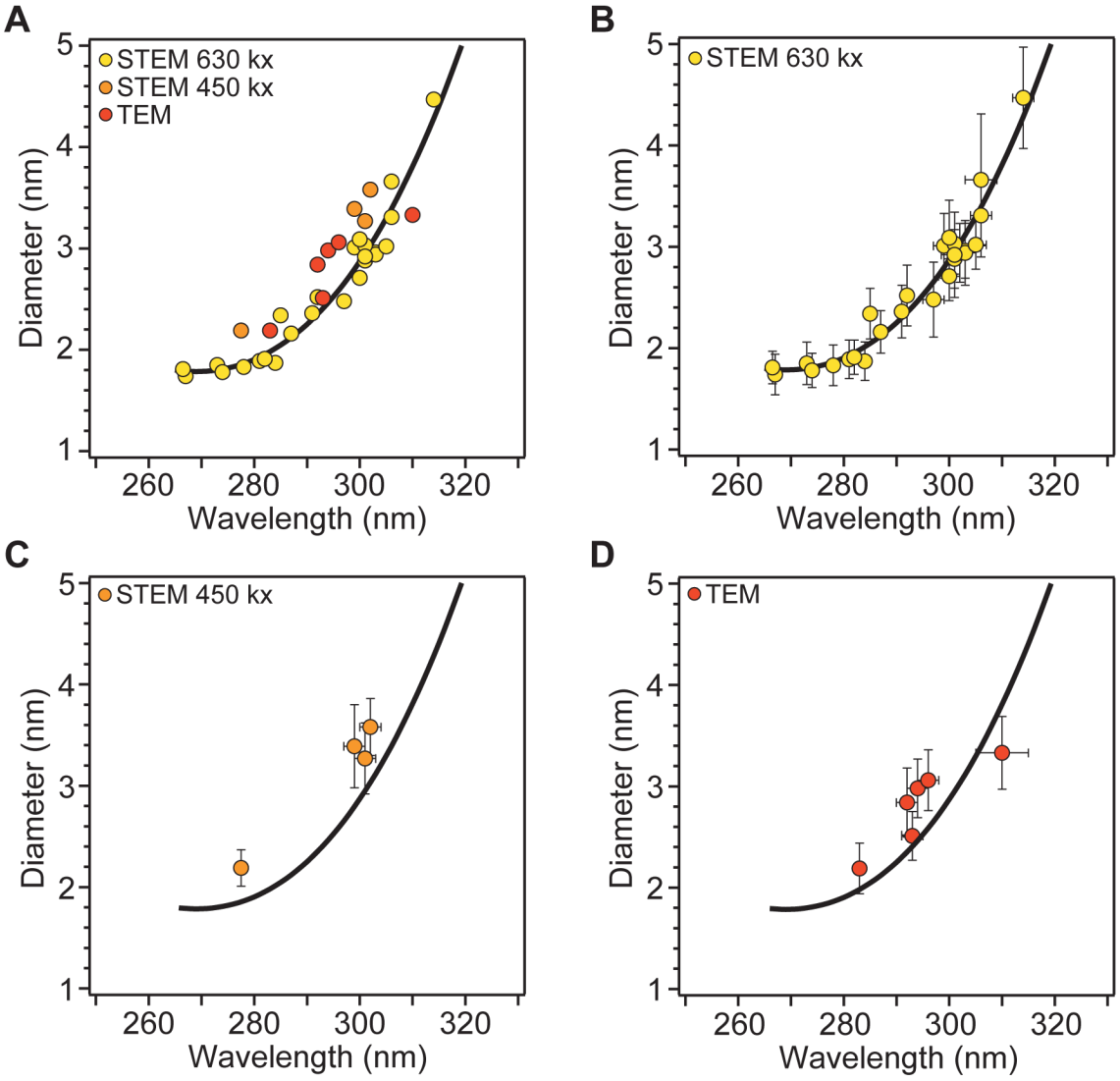

Figure S42. Measured nanocrystal diameter plotted as a function of peak wavelength for all electron microscopy results (A), highest magnification STEM (620 kx, B), lower magnification STEM (450 kx, C), and TEM (D).

Sizing curve discussion

Bohr radius and quantum confinement. ZnS has a small Bohr radius (r_B = 2.5 nm). In the strong quantum confinement regime ($r_{NC} < r_B$), a clear relationship between the energy of transition and the nanocrystal diameter can be extracted. At radii close to the Bohr radius, and therefore transition energies close to the bulk bandgap, the relationship between nanocrystal size and transition energy becomes harder to define. At these larger sizes, the peak energy becomes more challenging to determine. Additionally, a small change in transition energy corresponds to a large change in nanocrystal size.

Given the complications involved in determining sizes from optical spectra for weakly quantum confined nanocrystals, energy-size relationships reported for other metal sulfide nanocrystals are often reported for sizes much smaller than that of the Bohr radius (Figure S43, PbS: d ~ 2.8 – 10 nm).[29] With such a small Bohr radius, although the experimental diameter range used to generate the ZnS sizing curve is 1.7 – 4.5 nm, we suggest that this sizing curve is most reliable for d = 1.7 – 4.0 nm ($E_{1s\text{-}1s}$ = 3.97 – 4.64 eV, λ_{max} = 266 – 312 nm). Indeed, we find that at λ_{max} > ~ 313 nm ($E_{1s\text{-}1s}$ < ~ 3.95 eV), increasing nanocrystal size does not also significantly impact the optical spectrum. This is most apparent for aliquots during synthesis of large nanocrystals – the optical feature does not noticeably red-shift but the nanocrystals are growing.

So, if samples require sizing that are large (E_g < 3.97, λ_{max} > 312, r_{NC} > ~ 2 nm), we suggest the most accurate way to determine the nanocrystal size is to use electron microscopy techniques. Providing the sample is prepared carefully – free of contaminating organics, not too concentrated, and well dispersed on the TEM grid – the nanocrystals are large enough to be straightforward to get good data for. For such large ZnS, to get an approximate size, the equation describing the relationship between $E_{1s\text{-}1s}$ (eV) and diameter (nm) can be used, and will give a better estimation than the diameter (nm) versus wavelength (nm) fit.

Ligand and solvent choice. ZnS nanocrystals synthesized using these methods absorb UV-wavelengths beginning at λ = 260 – 320 nm, depending on their size. As discussed in the main text, many other molecules also absorb in this UV window. If such species are present, they can either completely obscure the optical feature or can slightly shift the observed energy of the ZnS optical feature. As such, the following conditions were used to take all optical spectra:

(1) Hexanes was used as solvent for UV absorption measurements. Hexanes was chosen because of its UV transparency and the ZnS nanocrystals are colloidally stable in it. Selection of a different solvent, for example chloroform, lead to a slight change in the energy at the peak maximum – likely due to the different UV cut-offs of the two solvents.

(2) ZnS should be thoroughly cleaned. Aryl containing precursors will absorb in same wavelength range and obscure/shift the optical feature.

(3) ZnS nanocrystals are bound purely by zinc carboxylates. We find that addition of octylamine to a sample can cause a slight red-shift (Figure S44). Under the assumption that the addition of octylamine did not significantly impact the average ZnS diameter, the red-shift caused by the addition results in the nanocrystal size being overestimated (when using the sizing curve).

With these conditions in mind, to obtain the most accurate results from these sizing curves, hexanes should be used as the UV absorption solvent, and the nanocrystals should be cleaned and bound only by zinc carboxylates/carboxylic acid.

Final considerations. Given the challenges in sizing small ZnS nanocrystals, and the discussion above regarding how solvent and ligand choice can alter the apparent $E_{1s\text{-}1s}$ it is unsurprising that reported sizes (Tables S3 – 5) and sizing curves (Figure S45) do not all agree well with each other. Additionally, we've shown that the ZnS nanocrystal shape is sensitive to many factors, and anisotropic nanocrystals further complicate the energy-size relationship.

The method outlined in this manuscript affords the synthesis of quasi-spherical nanocrystals. The sizing curves presented herein can then be applied to accurately extract diameters, using hexanes as the solvent for UV absorption spectroscopy. Care should be taken when applying these sizing curves to nanocrystals bound by ligands other than zinc carboxylate but should give a reasonable estimate of the size.

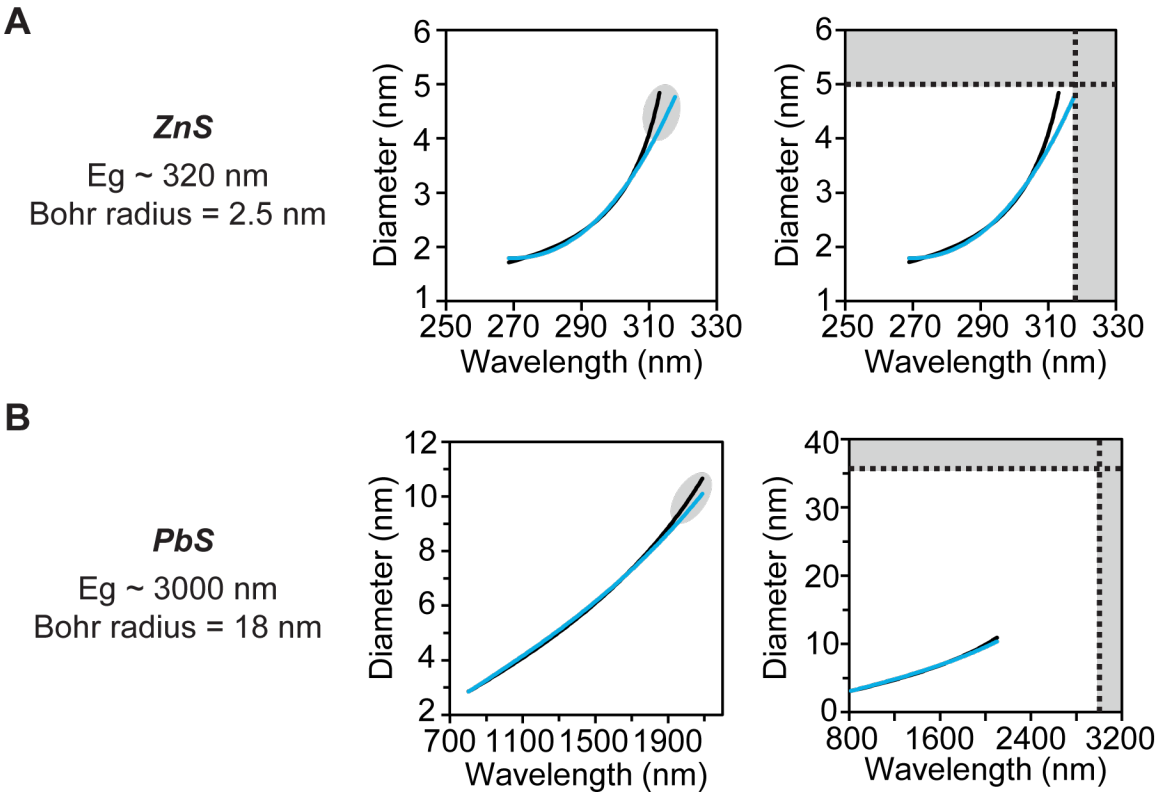

Figure S43. Comparison of ZnS sizing curve to a PbS sizing curve. PbS data is replotted using equations from Maes *et al.*[29] Comparison of the size-energy relationship extracted from (1) the eV *vs* diameter fit and (2) the diameter *vs* wavelength fit. For a given diameter, the energy of transition was calculated using (1), then converted to units of wavelength (plotted in black). This wavelength was then converted back to a diameter using (2) (plotted in blue). As expected, the two relationships give agreeing nanocrystal sizes for a given energy for ZnS and PbS. In all cases, at larger sizes the lines begin to deviate from each other, this is due to the difference in the shape of function between (1) and (2) the data has been fit to. For ZnS, comparison of the experimental data points to sizing curves (1) and (2), suggests that the eV *vs* diameter relationship better describes the nanocrystal size when approaching the Bohr radius.

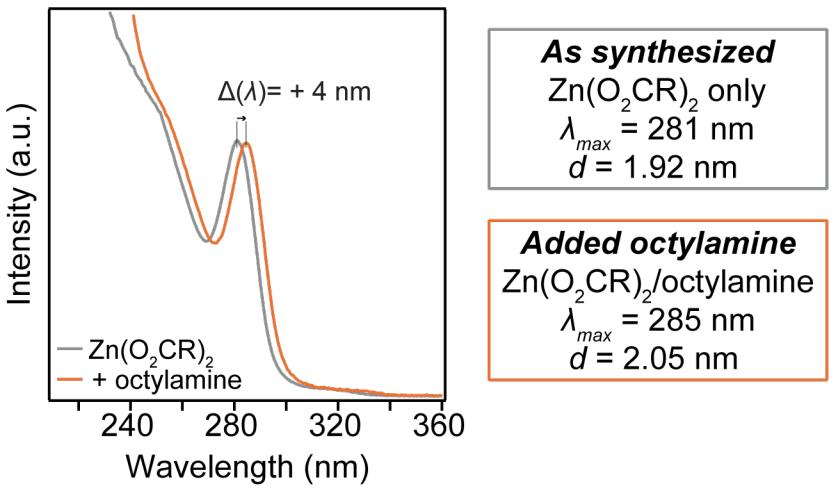

Figure S44. UV absorbance spectra of ZnS ligated by zinc oleate (grey), and zinc oleate + octylamine (orange). Diameters are calculated using the sizing curve.

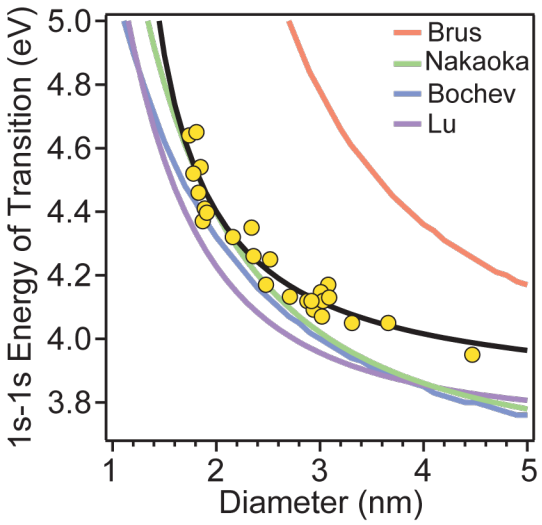

Figure S45. Comparison to experimental (green, blue, purple) and theoretical (orange) published ZnS sizing curves. The sizing relationship established here (black) shows comparable behaviour to published sizing curves at small sizes but deviates at larger diameters. The STEM data collected in this study is shown in yellow. Sizing curves are reproduced from work by Brus[30] (orange), Nakaoka and Nosaka[16] (green), Bochev and Yordanov[4] (blue), and Lu *et al.*[10] (purple).

Section III - References

1. Baruah, J. M.; Kalita, S.; Narayan, J., Green chemistry synthesis of biocompatible ZnS quantum dots (QDs): their application as potential thin films and antibacterial agent. *International Nano Letters* **2019,** *9*, 149-159.
2. Shahid, R.; Toprak, M. S.; Soliman, H. M. A.; Muhammed, M., Low temperature synthesis of cubic phase zinc sulfide quantum dots. *Central European Journal of Chemistry* **2012,** *10*, 54-58.
3. Barman, B.; Chandra Sarma, K., Low temperature chemical synthesis of ZnS, Mn doped ZnS nanosized particles: Their structural, morphological and photophysical properties. *Solid State Sciences* **2020,** *109*, 106404.
4. Bochev, B.; Yordanov, G., Room temperature synthesis of thioglycolate-coated zinc sulfide (ZnS) nanoparticles in aqueous medium and their physicochemical characterization. *Colloids and Surfaces A: Physicochemical and Engineering Aspects* **2014,** *441*, 84-90.
5. He, J.; Ji, W.; Mi, J.; Zheng, Y.; Ying, J. Y., Three-photon absorption in water-soluble ZnS nanocrystals. *Applied Physics Letters* **2006,** *88*, 181114.
6. Vogel, W.; Borse, P. H.; Deshmukh, N.; Kulkarni, S. K., Structure and Stability of Monodisperse 1.4-nm ZnS Particles Stabilized by Mercaptoethanol. *Langmuir* **2000,** *16*, 2032-2037.
7. Dumbrava, A.; Badea, C.; Prodan, G.; Popovici, I.; Ciupina, V., Zinc sulfide fine particles obtained at low temperature. *Chalcogenide Letters* **2009,** *6*, 437-443.
8. Wang, Y. H.; Chen, Z.; Zhou, X. Q., Synthesis and Photoluminescence of ZnS Quantum Dots. *Journal of Nanoscience and Nanotechnology* **2008,** *8*, 1312-1315.
9. Chandrakar, R. K.; Baghel, R. N.; Chandra, V. K.; Chandra, B. P., Synthesis, characterization and photoluminescence studies of undoped ZnS nanoparticles. *Superlattices and Microstructures* **2015,** *84*, 132-143.
10. Lu, S. H.; Chen, T. F.; Wang, A. J.; Wu, Z. L.; Wang, Y. S., Lattice and optical property evolution of ultra-small ZnS quantum dots grown from a single-source precursor. *Applied Surface Science* **2014,** *299*, 116-122.
11. Kho, R.; Torres-Martínez, C. L.; Mehra, R. K., A Simple Colloidal Synthesis for Gram-Quantity Production of Water-Soluble ZnS Nanocrystal Powders. *Journal of Colloid and Interface Science* **2000,** *227*, 561-566.
12. Juine, R. N.; Das, A.; Amirthapandian, S., Concentration controlled QDs ZnS synthesis without capping agent and its optical properties. *Materials Letters* **2014,** *128*, 160-162.
13. Joo, J.; Na, H. B.; Yu, T.; Yu, J. H.; Kim, Y. W.; Wu, F.; Zhang, J. Z.; Hyeon, T., Generalized and Facile Synthesis of Semiconducting Metal Sulfide Nanocrystals. *Journal of the American Chemical Society* **2003,** *125*, 11100-11105.
14. Rossetti, R.; Hull, R.; Gibson, J. M.; Brus, L. E., Excited electronic states and optical spectra of ZnS and CdS crystallites in the ≅15 to 50 Å size range: Evolution from molecular to bulk semiconducting properties. *The Journal of Chemical Physics* **1985,** *82*, 552-559.
15. Nanda, J.; Sapra, S.; Sarma, D. D.; Chandrasekharan, N.; Hodes, G., Size-Selected Zinc Sulfide Nanocrystallites: Synthesis, Structure, and Optical Studies. *Chemistry of Materials* **2000,** *12*, 1018-1024.
16. Nakaoka, Y.; Nosaka, Y., Electron Spin Resonance Study of Radicals Produced by Photoirradiation on Quantized and Bulk ZnS Particles. *Langmuir* **1997,** *13*, 708-713.
17. Xia, Y.; Zhai, G.; Zheng, Z.; Lian, L.; Liu, H.; Zhang, D.; Gao, J.; Zhai, T.; Zhang, J., Solution-processed solar-blind deep ultraviolet photodetectors based on strongly quantum confined ZnS quantum dots. *Journal of Materials Chemistry C* **2018,** *6*, 11266-11271.
18. Zhang, Y.; Xu, H.; Wang, Q., Ultrathin single crystal ZnS nanowires. *Chemical Communications* **2010,** *46*, 8941-8943.
19. Zhao, Y.; Zhang, Y.; Zhu, H.; Hadjipanayis, G. C.; Xiao, J. Q., Low-temperature synthesis of hexagonal (wurtzite) ZnS nanocrystals. *Journal of the American Chemical Society* **2004,** *126*, 6874-6875.

20. Kan, H.; Zheng, W.; Lin, R.; Li, M.; Fu, C.; Sun, H.; Dong, M.; Xu, C.; Luo, J.; Fu, Y.; Huang, F., Ultrafast Photovoltaic-Type Deep Ultraviolet Photodetectors Using Hybrid Zero-/Two-Dimensional Heterojunctions. *ACS Applied Materials & Interfaces* **2019,** *11*, 8412-8418.
21. Mahamuni, S.; Khosravi, A. A.; Kundu, M.; Kshirsagar, A.; Bedekar, A.; Avasare, D. B.; Singh, P.; Kulkarni, S. K., Thiophenol-capped ZnS quantum dots. *Journal of Applied Physics* **1993,** *73*, 5237-5240.
22. Hammersley, A. P., Fit2d v12. 012 reference manual v6.0. *ESRF Internal Report* **2004**, ESRF98HA01T.
23. Juhas, P.; Davis, T.; Farrow, C. L.; Billinge, S. J. L., PDFgetX3: a rapid and highly automatable program for processing powder diffraction data into total scattering pair distribution functions. *Journal of Applied Crystallography* **2013,** *46*, 560-566.
24. Yang, X.; Juhas, P.; Farrow, C. L.; Billinge, S. J. L., xPDFsuite: an end-to-end software solution for high throughput pair distribution function transformation, visualization and analysis. *arXiv preprint arXiv:1402.3163* **2015**, doi: 1402.3163.
25. Kodama, K.; Iikubo, S.; Taguchi, T.; Shamoto, S., Finite size effects of nanoparticles on the atomic pair distribution functions. *J Acta Crystallographica Section A: Foundations of Crystallography* **2006,** *62*, 444-453.
26. Farrow, C. L.; Juhas, P.; Liu, J. W.; Bryndin, D.; Božin, E. S.; Bloch, J.; Proffen, T.; Billinge, S. J. L., PDFfit2 and PDFgui: computer programs for studying nanostructure in crystals. *Journal of Physics: Condensed Matter* **2007,** *19*, 335219.
27. Yang, X.; Masadeh, A. S.; McBride, J. R.; Božin, E. S.; Rosenthal, S. J.; Billinge, S. J., Confirmation of disordered structure of ultrasmall CdSe nanoparticles from X-ray atomic pair distribution function analysis. *Physical Chemistry Chemical Physics* **2013,** *15*, 8480-8486.
28. Pyrz, W. D.; Buttrey, D. J., Particle Size Determination Using TEM: A Discussion of Image Acquisition and Analysis for the Novice Microscopist. *Langmuir* **2008,** *24*, 11350-11360.
29. Maes, J.; Castro, N.; De Nolf, K.; Walravens, W.; Abécassis, B.; Hens, Z., Size and Concentration Determination of Colloidal Nanocrystals by Small-Angle X-ray Scattering. *Chemistry of Materials* **2018,** *30*, 3952-3962.
30. Brus, L. E., Electron–electron and electron-hole interactions in small semiconductor crystallites: The size dependence of the lowest excited electronic state. *The Journal of Chemical Physics* **1984,** *80*, 4403-4409.

Appendix I – Electron microscopy histograms.

The following pages show the UV absorption spectra, representative EM image, and sizing histogram for all samples listed in tables S9 – 11.

Sample 1

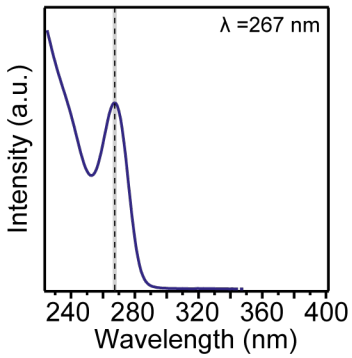

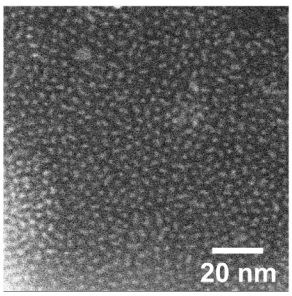

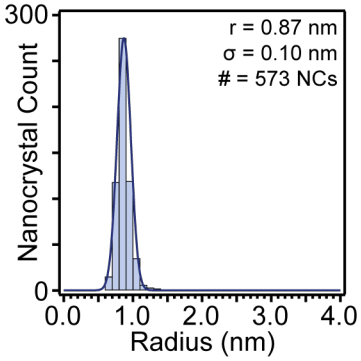

Sample 2

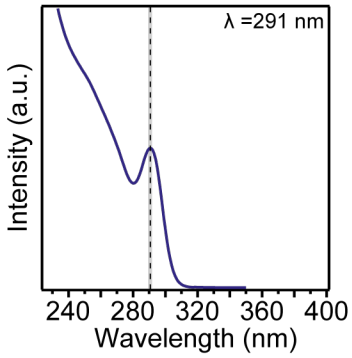

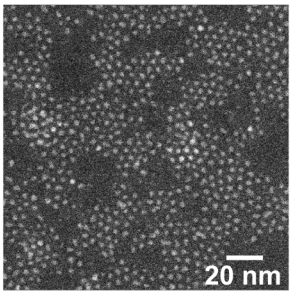

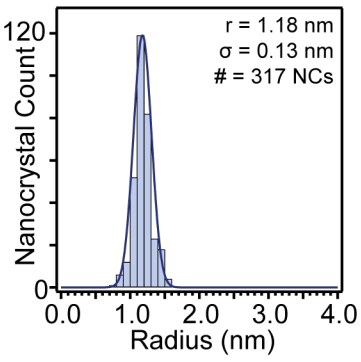

Sample 3

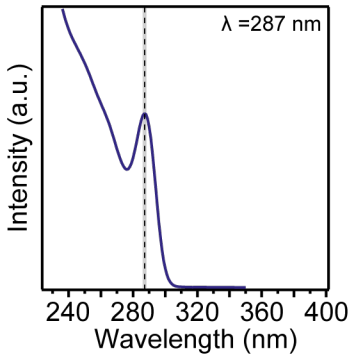

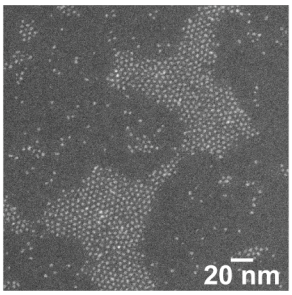

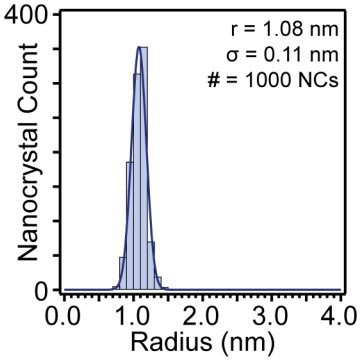

Sample 4

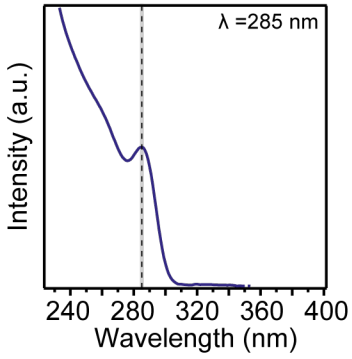

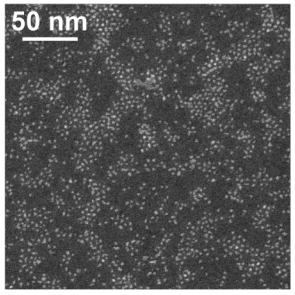

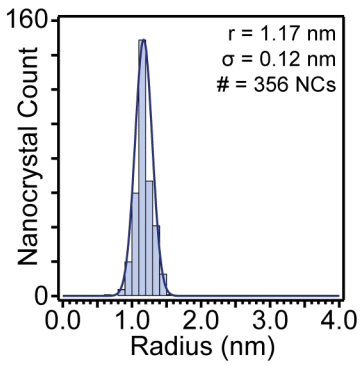

Sample 5

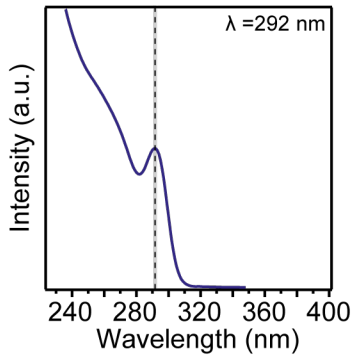

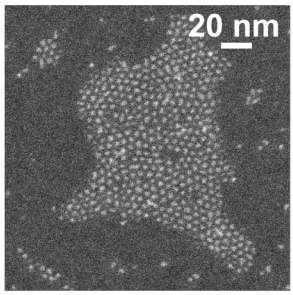

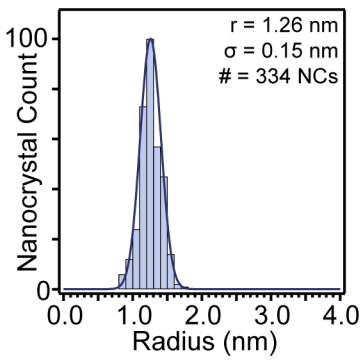

Sample 6

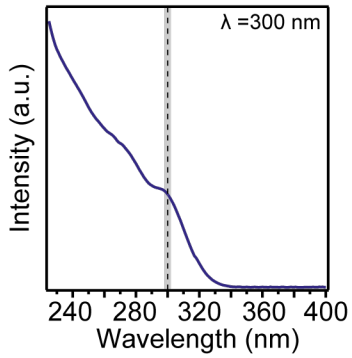

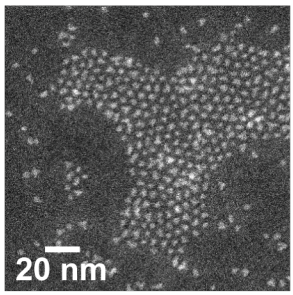

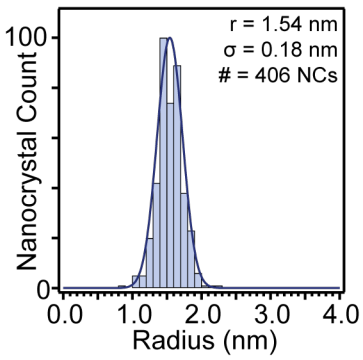

Sample 7

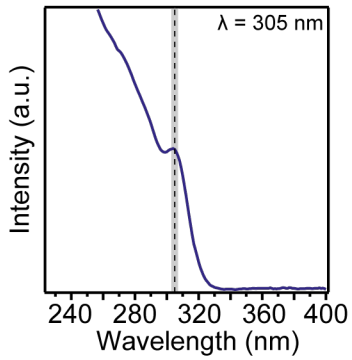

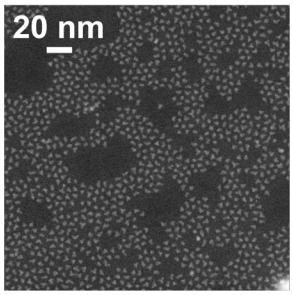

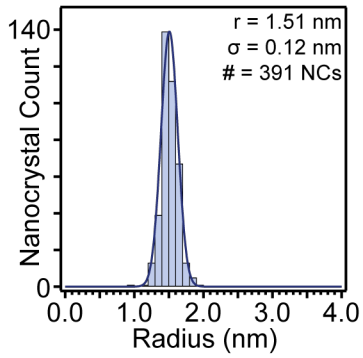

Sample 8

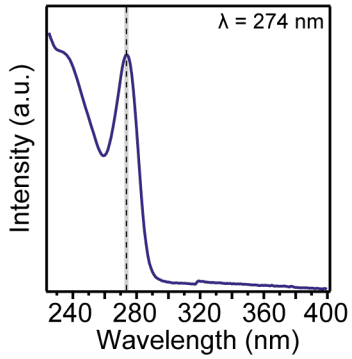

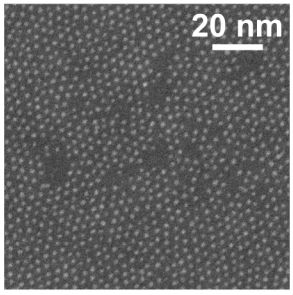

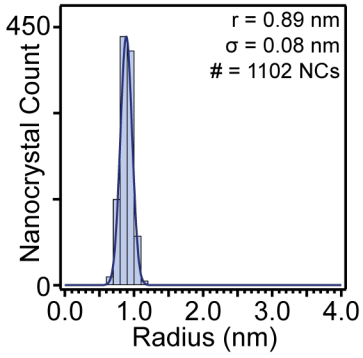

Sample 9

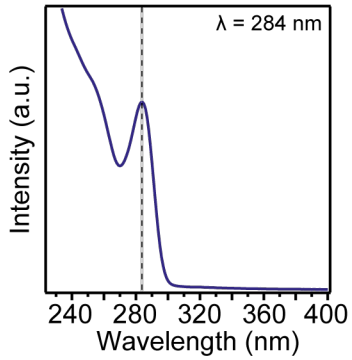

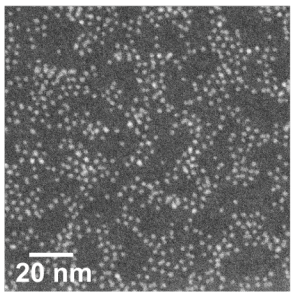

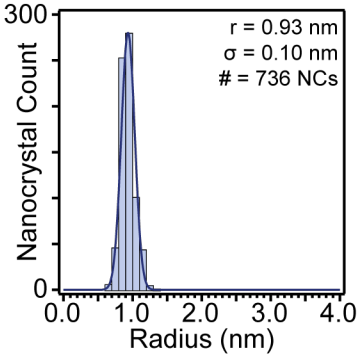

Sample 10

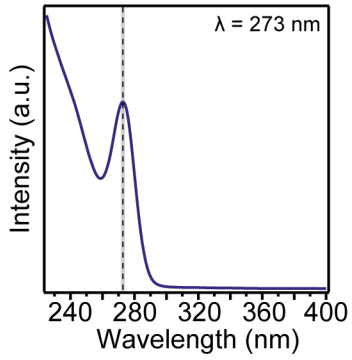

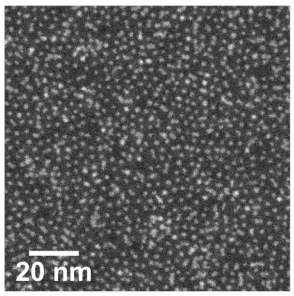

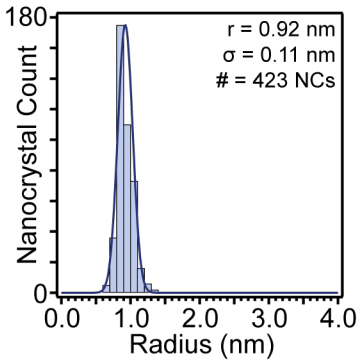

Sample 11

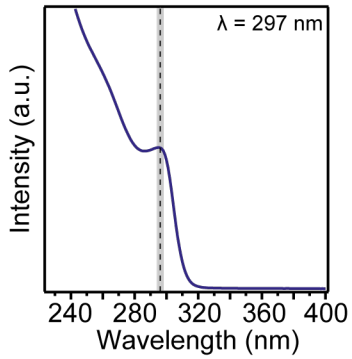

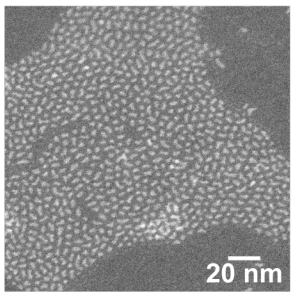

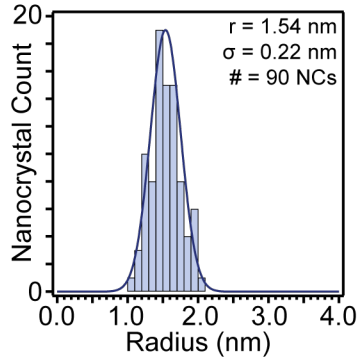

Sample 12

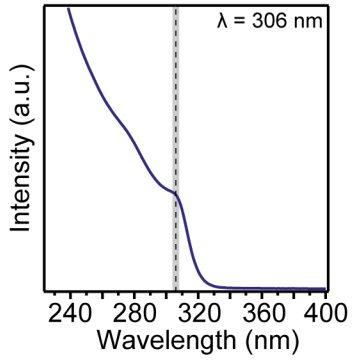

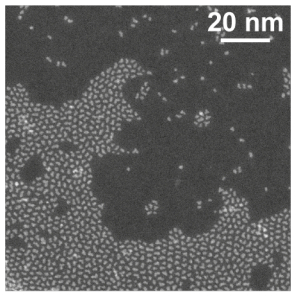

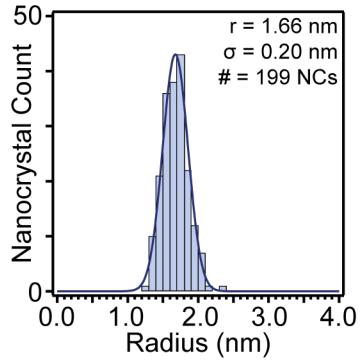

Sample 13

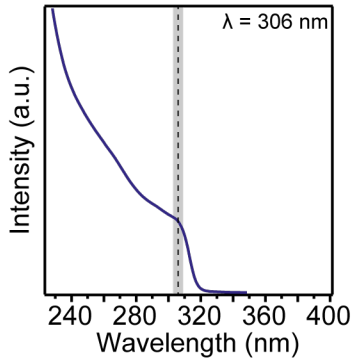

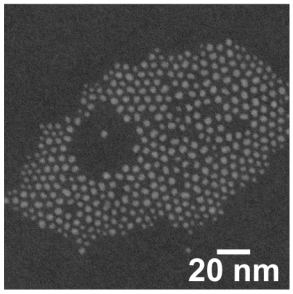

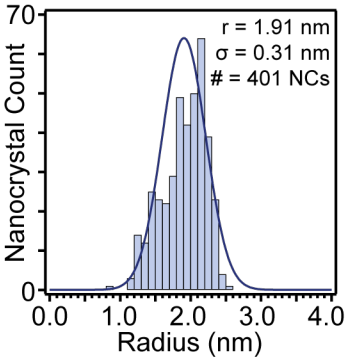

Sample 14

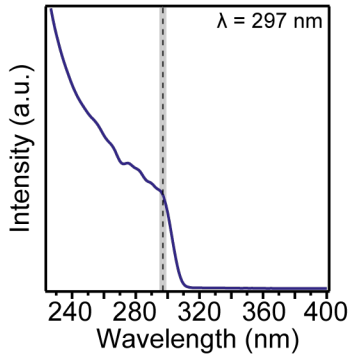

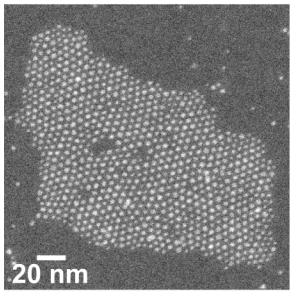

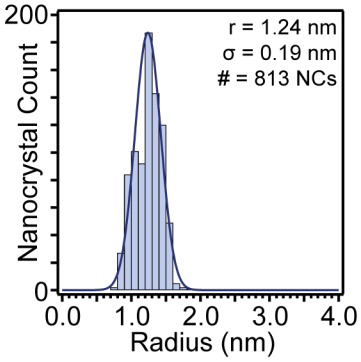

Sample 15

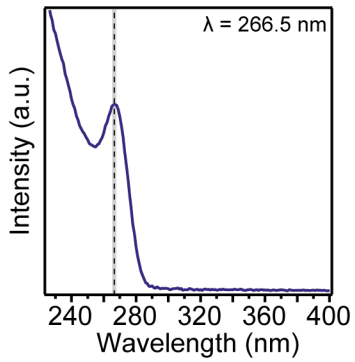

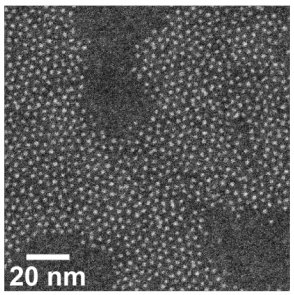

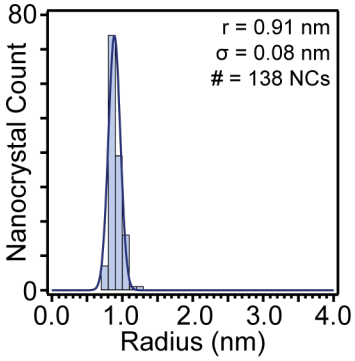

Sample 16

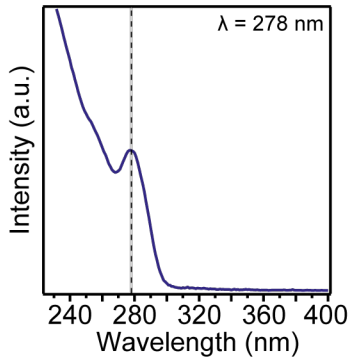

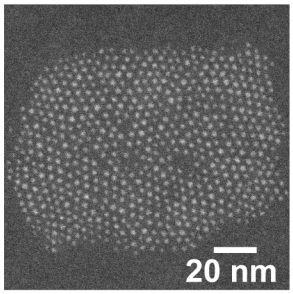

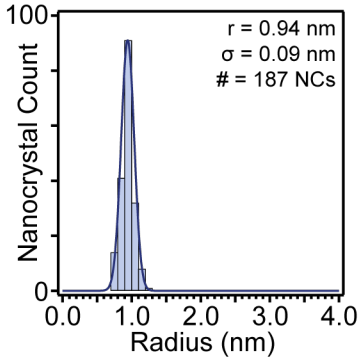

Sample 17

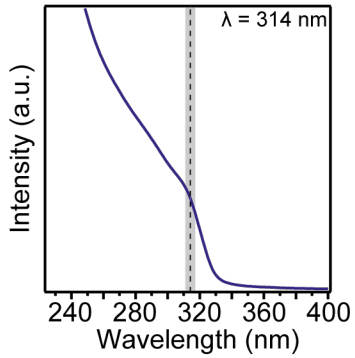

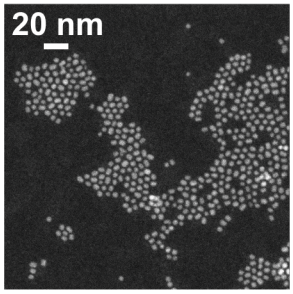

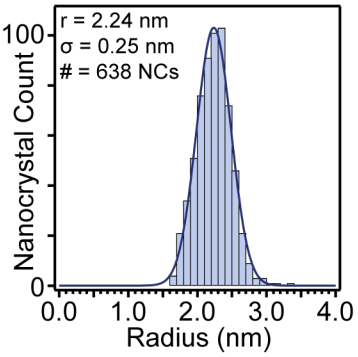

Sample 18

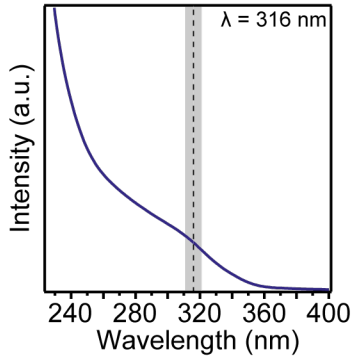

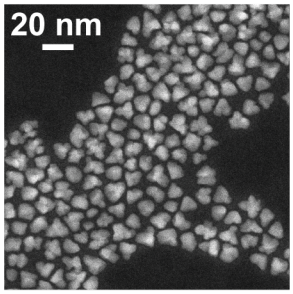

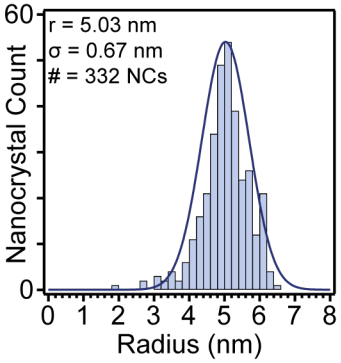

Sample 19

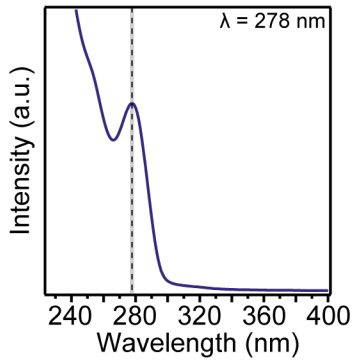

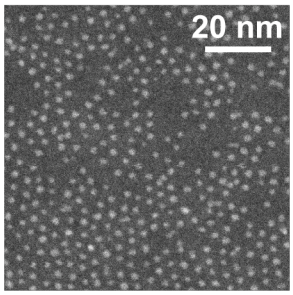

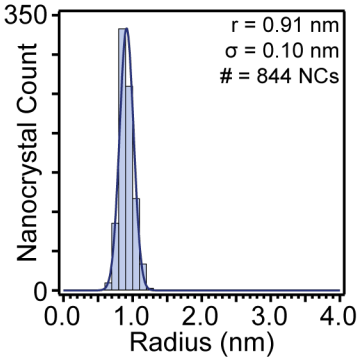

Sample 20

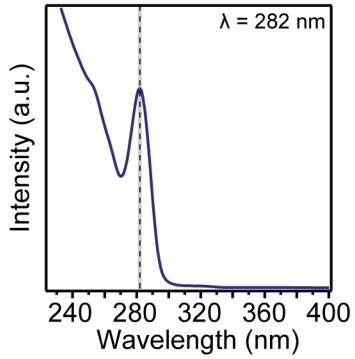

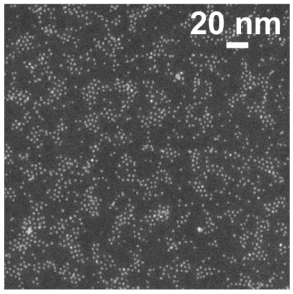

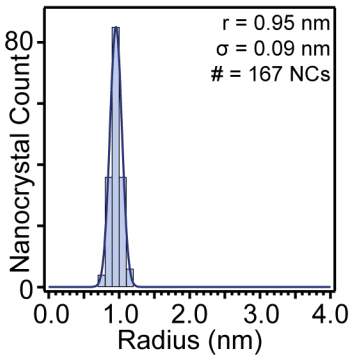

Sample 21

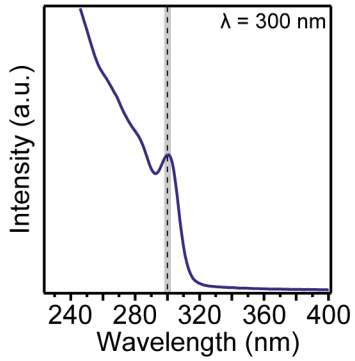

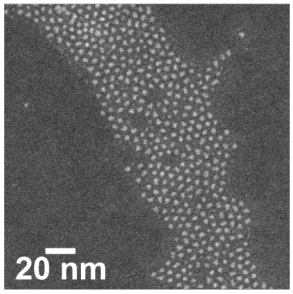

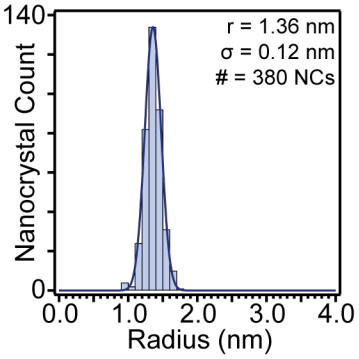

Sample 22

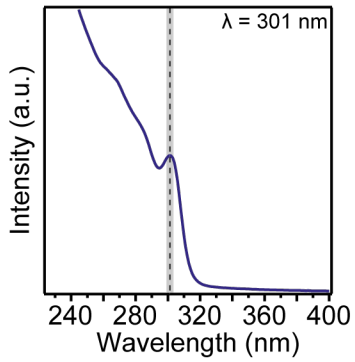

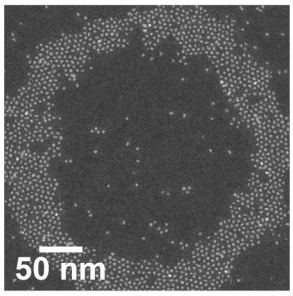

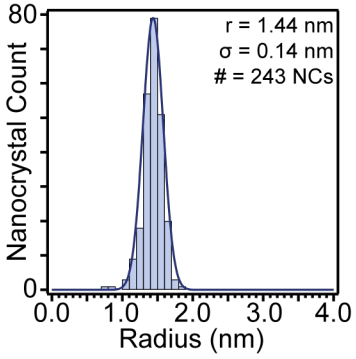

Sample 23

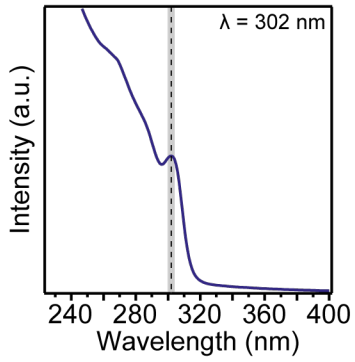

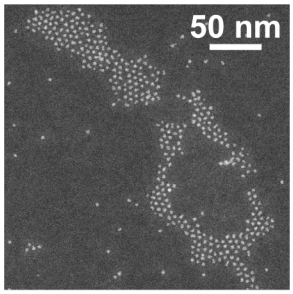

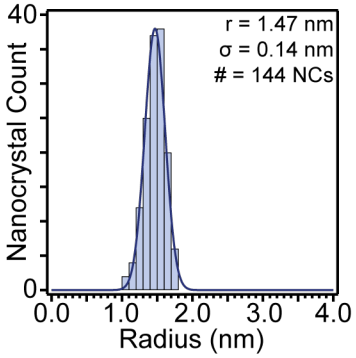

Sample 24

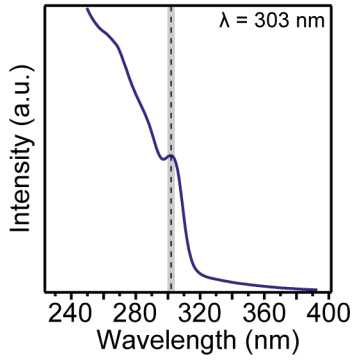

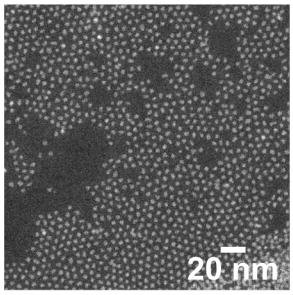

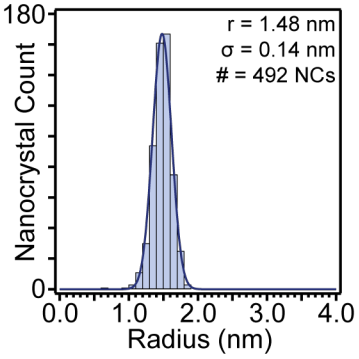

Sample 25

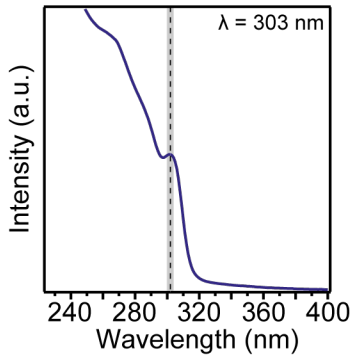

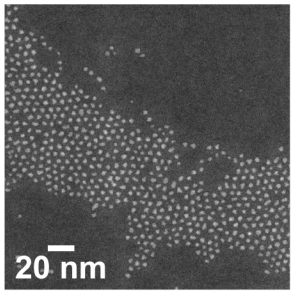

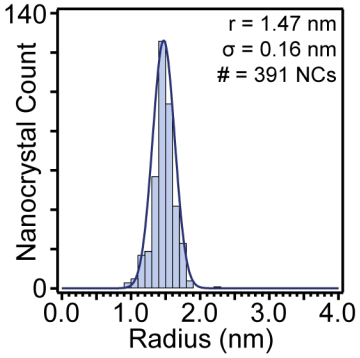

Sample 26

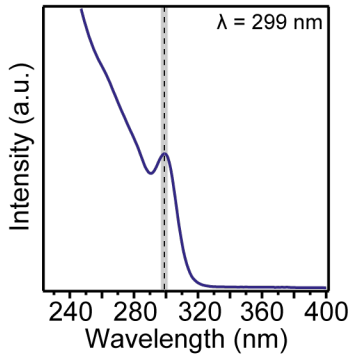

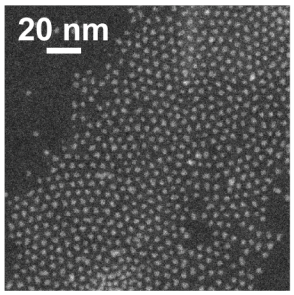

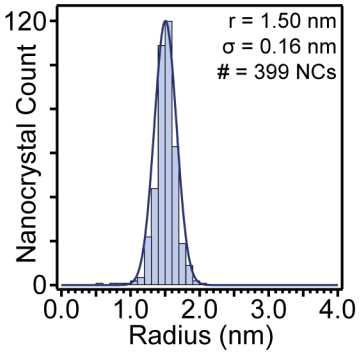

Sample 27

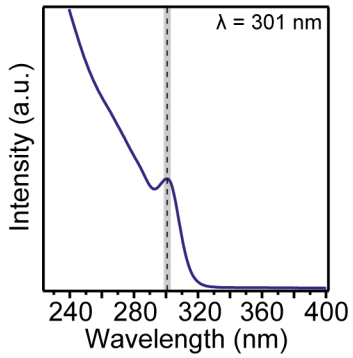

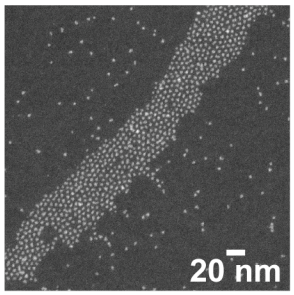

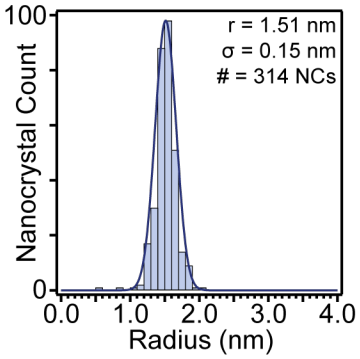

Sample 28

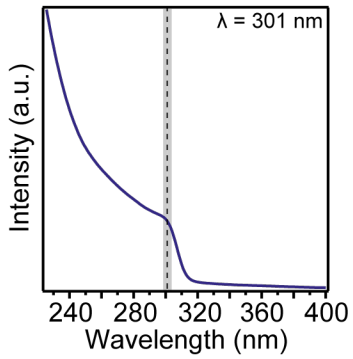

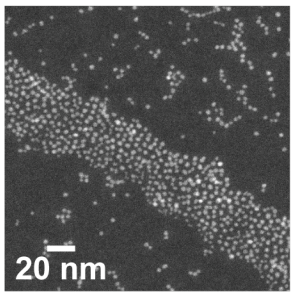

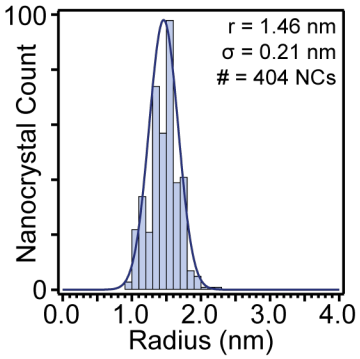

Sample 29

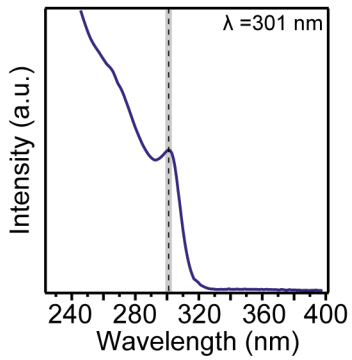

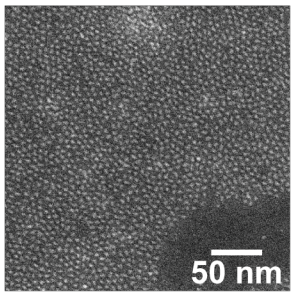

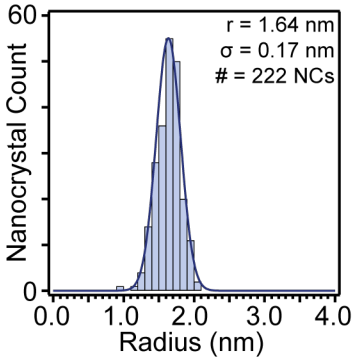

Sample 30

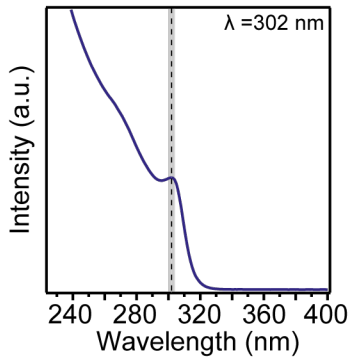

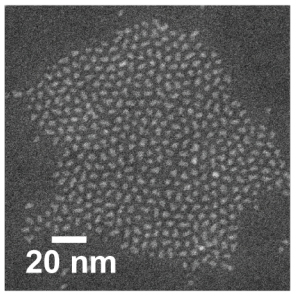

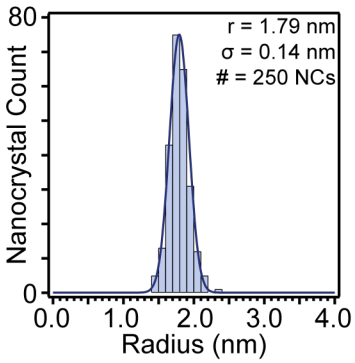

Sample 31

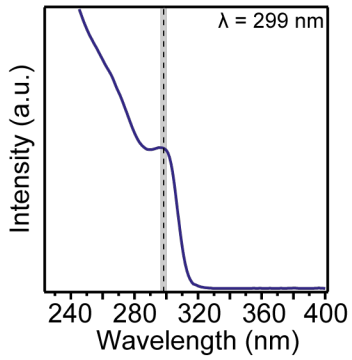

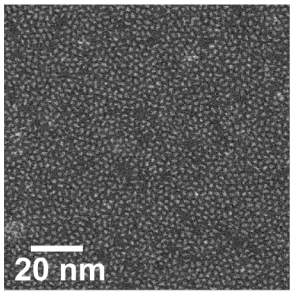

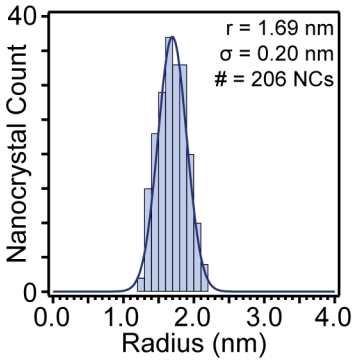

Sample 32

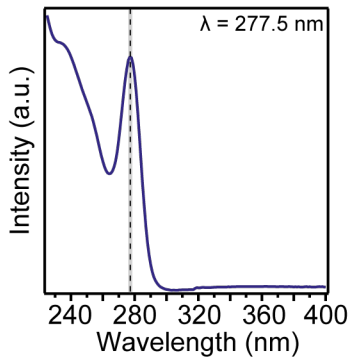

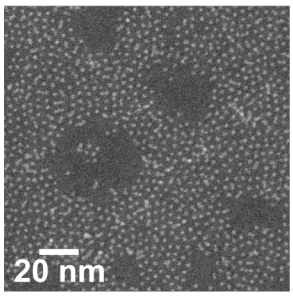

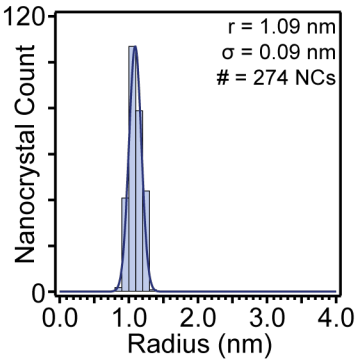

Sample 34

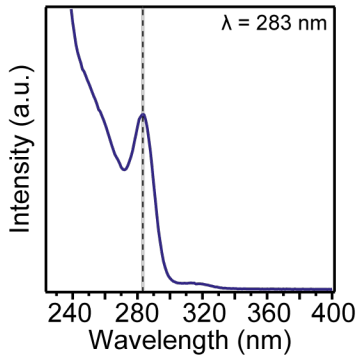

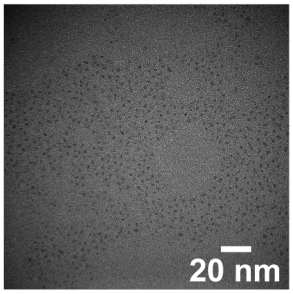

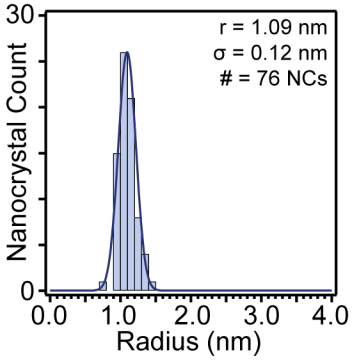

Sample 35

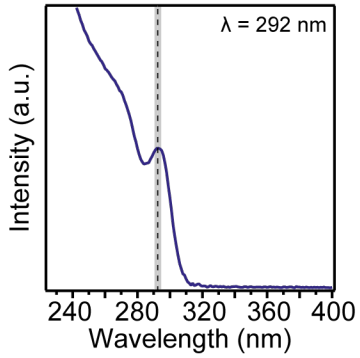

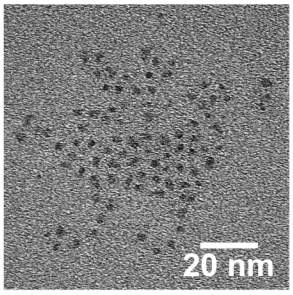

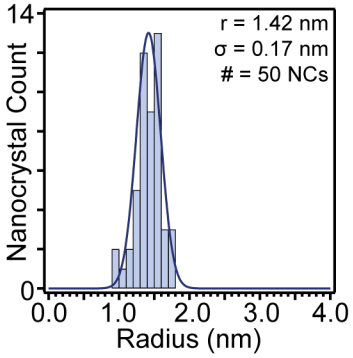

Sample 36

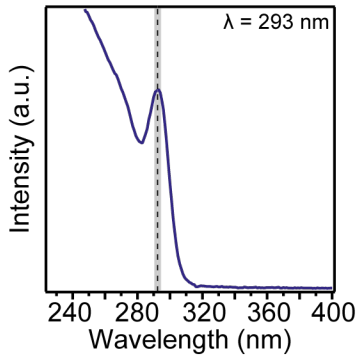

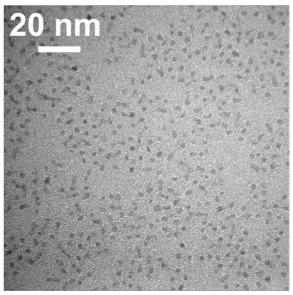

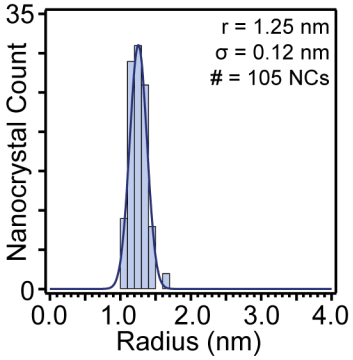

Sample 37

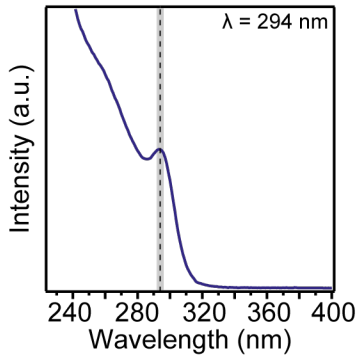

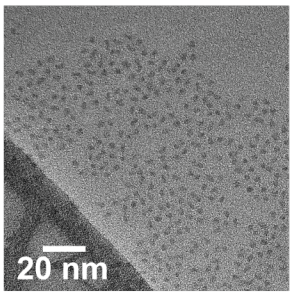

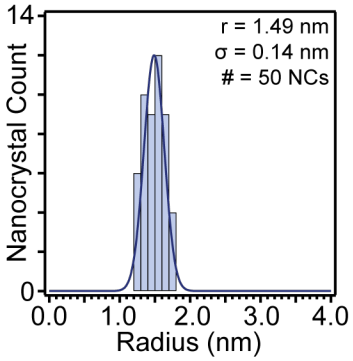

Sample 38

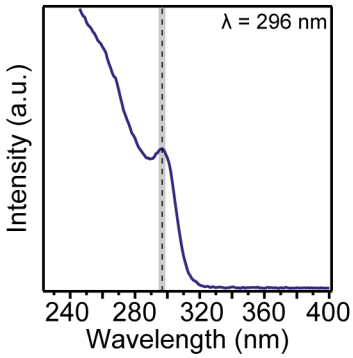

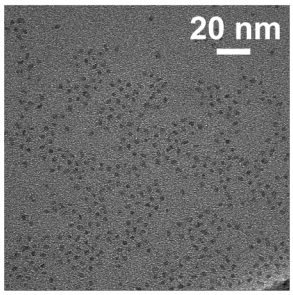

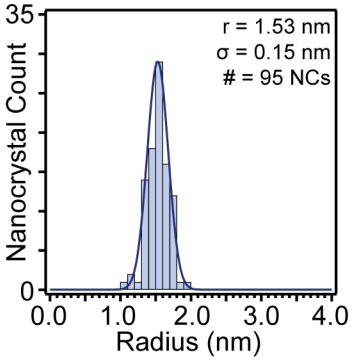

Sample 39

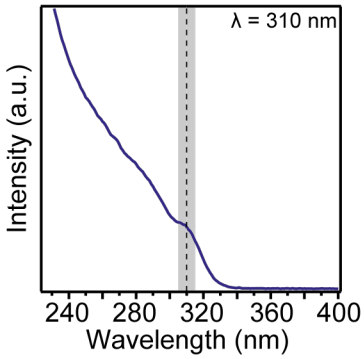

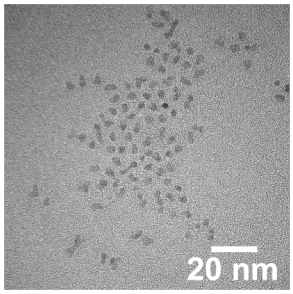

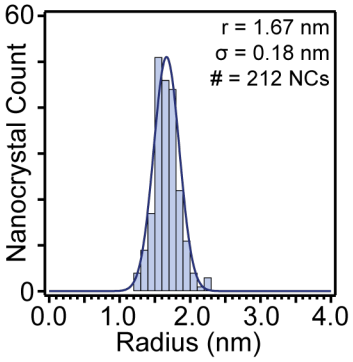

Appendix II – NMR characterization of new precursors

N-4-methoxy-phenyl, *N',N'-n*-dibutyl thiourea

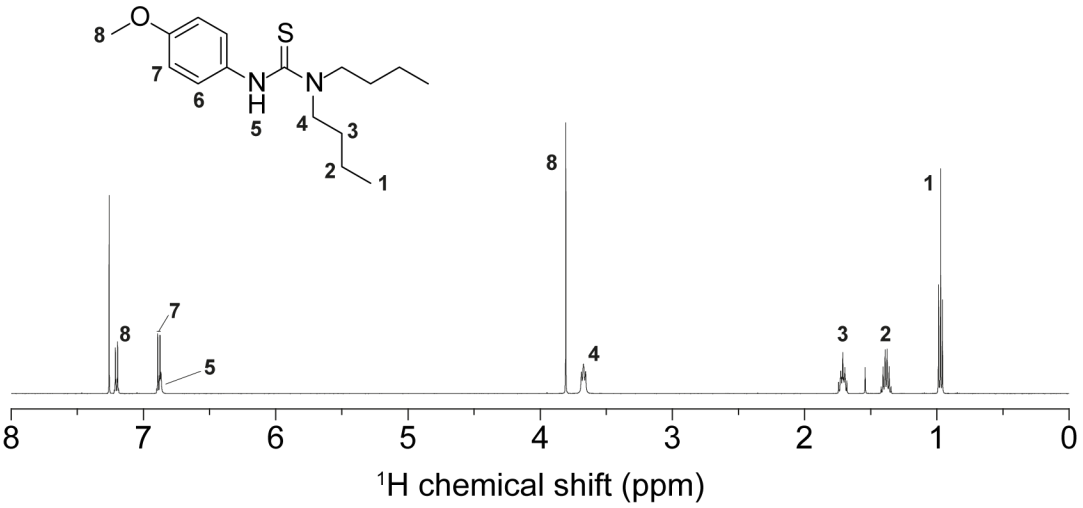

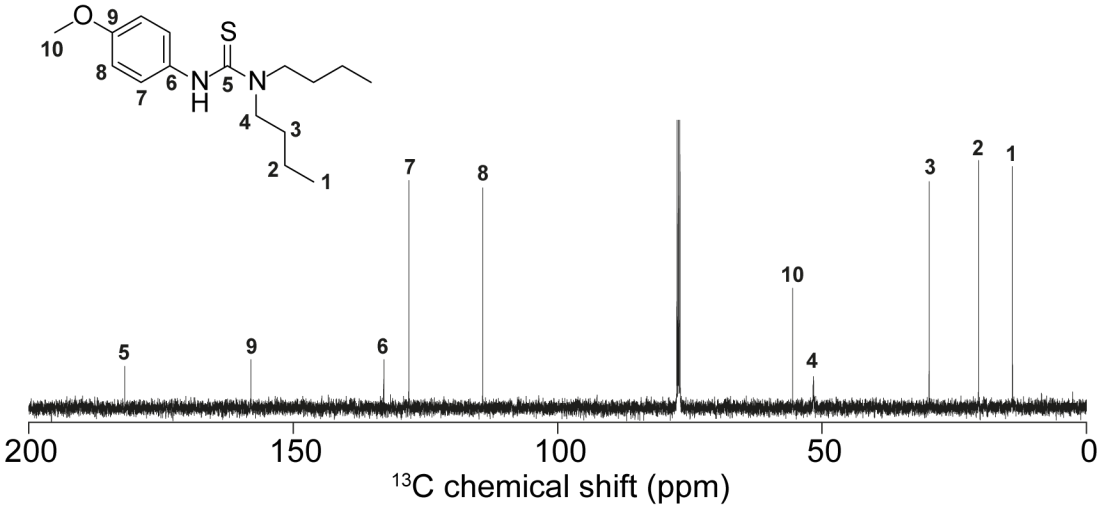

***N*-4-trifluoromethyl-phenyl, *N',N'-n*-dibutyl thiourea**

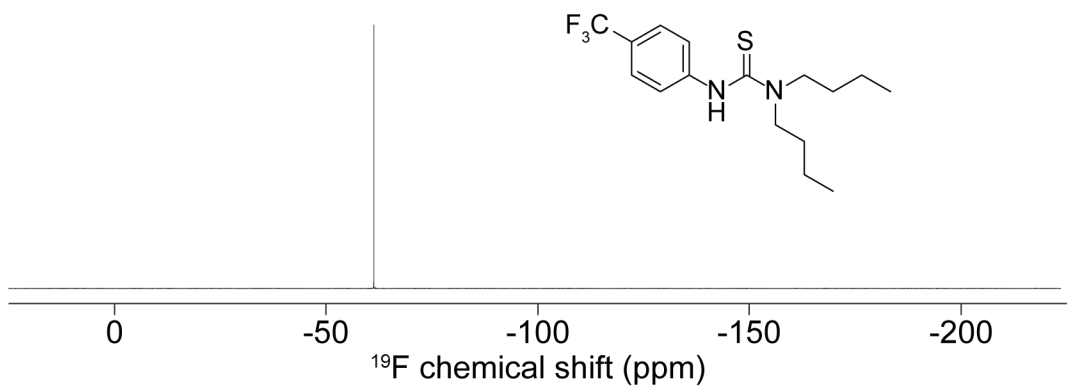

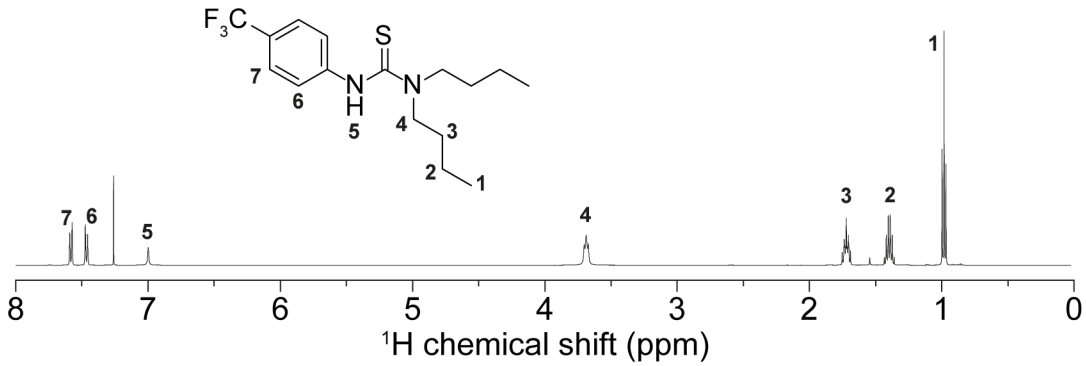

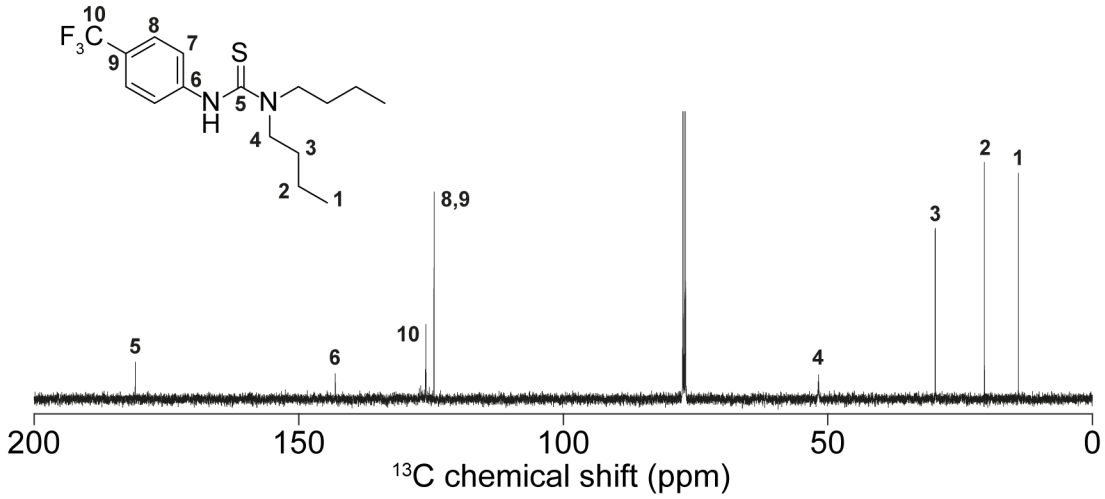

***N*-dodecyl, *N'*-pyrrolidine thiourea**

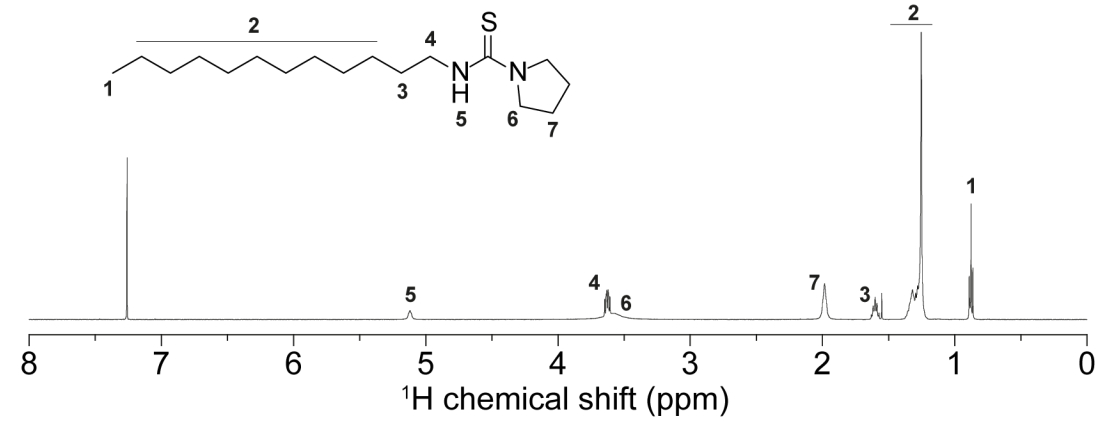

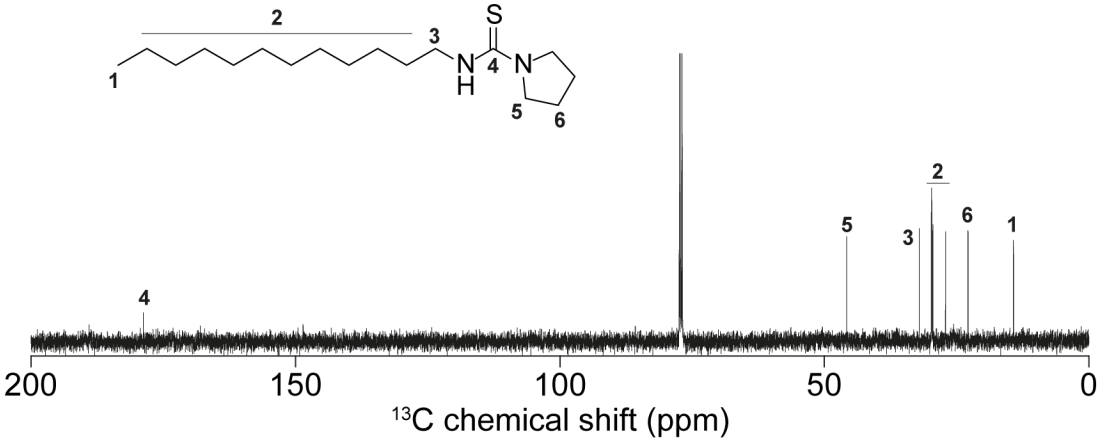

***N*-*n*-butyl, *N'*,*N'*-*n*-dibutyl thiourea**

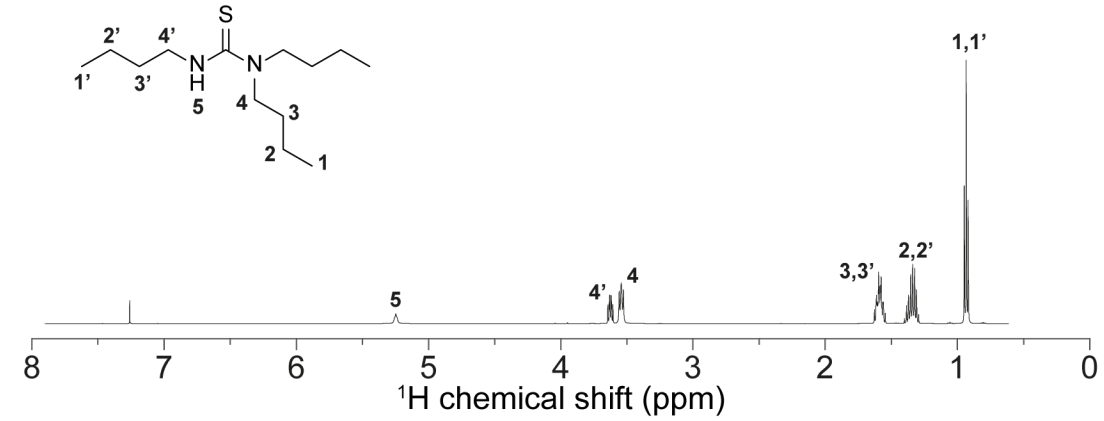

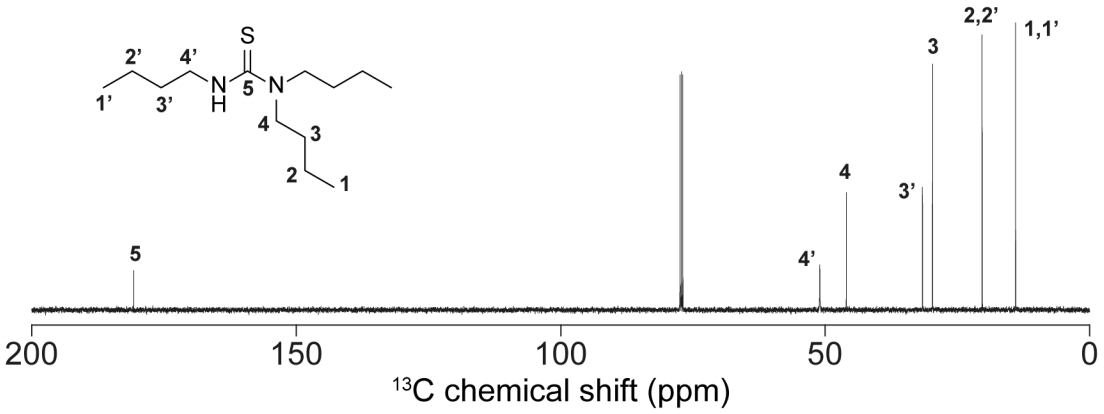

***P,P*-phenyl, *N*-(phenyl)phosphanecarbothioamide**

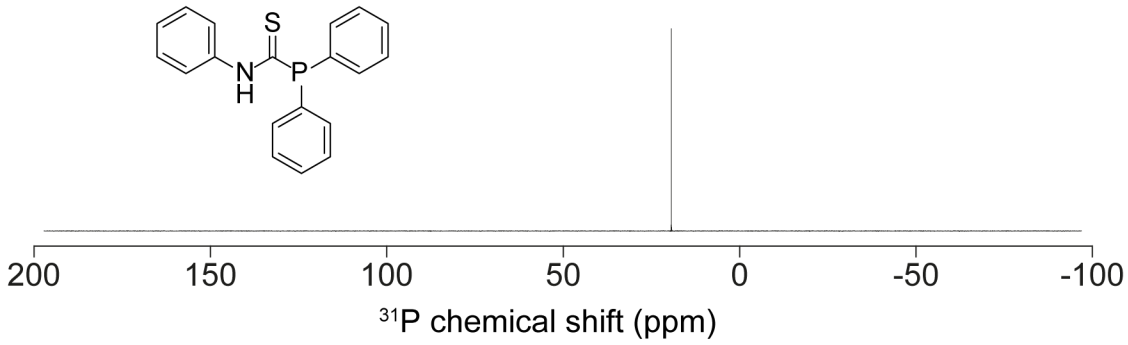

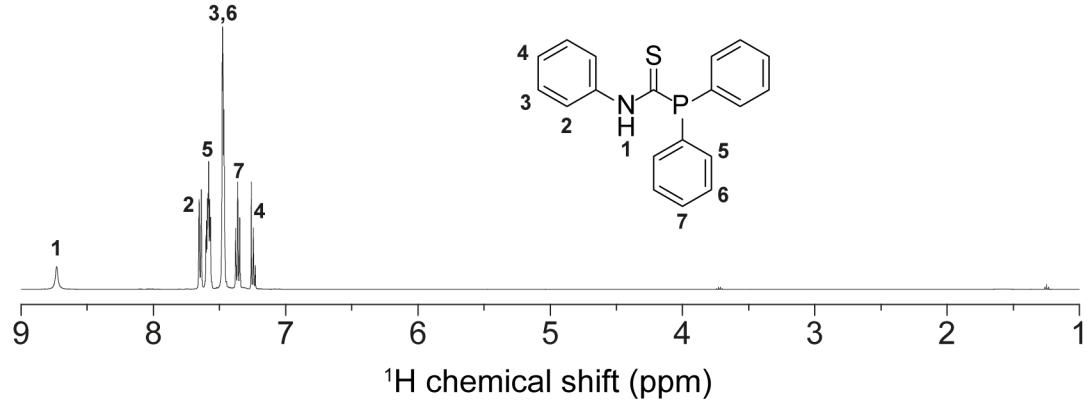

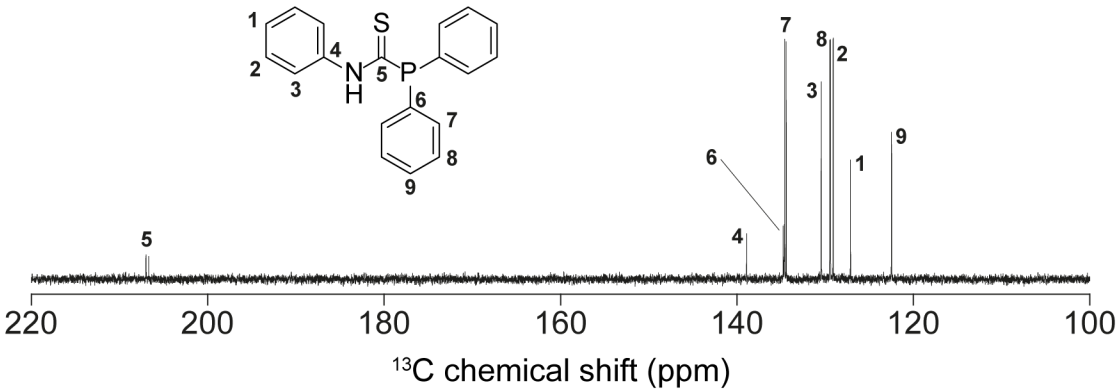

***P,P*-phenyl, *N*-(4-trifluoromethyl-phenyl)phosphanecarbothioamide**

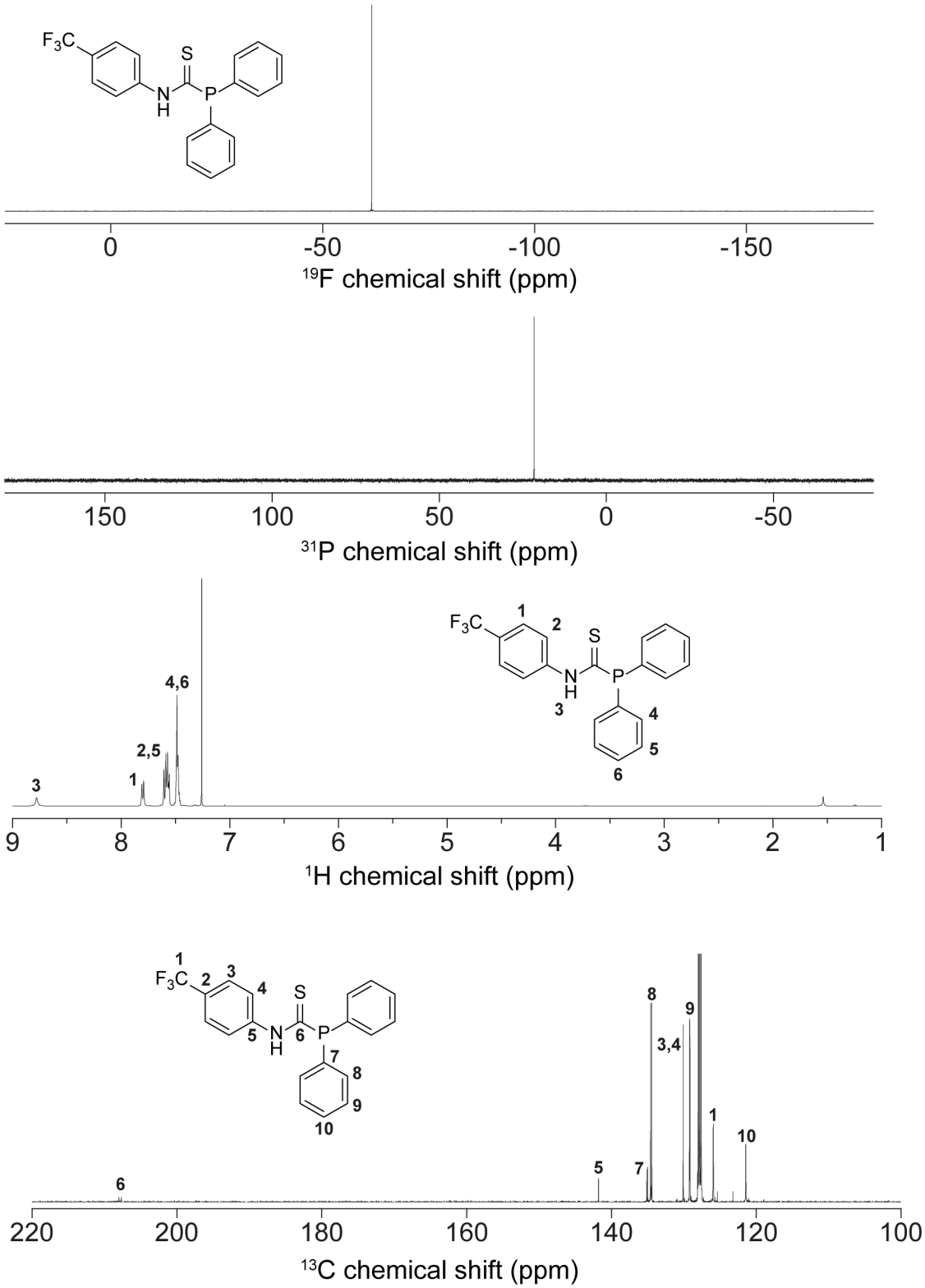

Zinc 2-hexyldecanoate